THE UNIVERSITY OF HULL

High-performance Geometric Vascular Modelling

being a Thesis submitted for the Degree of
Doctor of Philosophy
in the University of Hull

by

Quan QI
B.Sc, M.Sc Computer Science

November 2018

Abstract

Image-based high-performance geometric vascular modelling and reconstruction is an essential component of computer-assisted surgery on the diagnosis, analysis and treatment of cardiovascular diseases. However, it is an extremely challenging task to efficiently reconstruct the accurate geometric structures of blood vessels out of medical images. For one thing, the shape of an individual section of a blood vessel is highly irregular because of the squeeze of other tissues and the deformation caused by vascular diseases. For another, a vascular system is a very complicated network of blood vessels with different types of branching structures. Although some existing vascular modelling techniques can reconstruct the geometric structure of a vascular system, they are either time-consuming or lacking sufficient accuracy. What is more, these techniques rarely consider the interior tissue of the vascular wall, which consists of complicated layered structures. As a result, it is necessary to develop a better vascular geometric modelling technique, which is not only of high performance and high accuracy in the reconstruction of vascular surfaces, but can also be used to model the interior tissue structures of the vascular walls.

This research aims to develop a state-of-the-art patient-specific medical image-based geometric vascular modelling technique to solve the above problems. The main contributions of this research are:

- Developed and proposed the Skeleton Marching technique to reconstruct the geometric structures of blood vessels with high performance and high accuracy. With the proposed technique, the highly complicated vascular reconstruction task is reduced to a set of simple localised geometric reconstruction tasks, which can be carried out in a parallel manner. These locally reconstructed vascular geometric segments are then combined together using shape-preserving blending operations to faithfully represent the geometric shape of the whole vascular system.

- Developed and proposed the Thin Implicit Patch method to realistically model the interior geometric structures of the vascular tissues. This method allows the multi-layer interior tissue structures to be embedded inside the vascular wall to illustrate the geometric details of the blood vessel in real world.

Acknowledgement

Firstly, I would like to express my sincere gratitude to Dr Qingde Li, my supervisor, for providing me the chance of this PhD research project. His patience, motivation and immense knowledge helped me in all the time of this research. Without his consistent support and illuminating instruction, this thesis could not have reached the present form.

My sincere thank also goes to the members of my research committee, Dr Leonardo Bottaci and Mr James Ward, for their insightful comments and advices on each stage of my research.

I am especially thankful to Mr Mike Bielby for the 3D printing of my modelling results and the setting up of my poster. I also want to say thanks to Mrs Lynn Morrell for her kind helps on administrative works during my PhD study.

In particular, I would like to acknowledge the China Scholarship Council (CSC) and the University of Hull for a joint scholarship to support my study and living in the UK.

Additionally, my great gratitude to Dr Jian Wang, Dr Xinhui Ma, Dr Yan Li, Rev Kam Ho and Mrs Mi Ting Ho. They gave me a lot of helps during and after the hard time of the suspension from my PhD study.

Last but not least, I would like to thank my father and sister for supporting me throughout my PhD research. And my eternal memory goes to my beloved mother, who passed away during the third year of my PhD study, to give me a strong faith in doing research for human well-being.

Dedication

Parts of this thesis are published as research papers with Dr. Qingde Li and Dr. Qingqi Hong in the following sources:

- Quan Qi and Qingde Li, “From Visible to Printable: Thin Surface with Implicit Interior Structures”, In *ACM SIGGRAPH 2018 Posters (SIGGRAPH ’18).* ACM, New York, NY, USA, Article 64, 2 pages.
- Quan Qi, Qingde Li and Qingqi Hong, “Skeleton Marching: A High-performance Parallel Vascular Geometry Reconstruction Technique”, Best Student Paper Reward, *The 24th International Conference on Automation and Computing*, Newcastle, 2018
- Quan Qi and Qingde Li, “Thin Implicit Utah Teapot: Design for Additive Manufacturing”, *The 18th International Conference on Computer and Information Technology*, 2018, Halifax, Canada
- Qingde Li, Qingqi Hong, Quan Qi et al, Towards additive manufacturing oriented geometric modeling using implicit functions. *Visual Computing for Industry, Biomedicine, and Art*, 1(1), September 2018
- Quan Qi, Qingde Li and Qingqi Hong, “Implicit Vascular Reconstruction using the Shape-Presenting Blending Operation”, *The 20th International Conference on Automation and Computing*, Cranfield, 2014, pp. 200–205.

Abbreviations

CAD Computer-aided Design. 86

CAGD Computer-aided Geometric Design. 5

CAM Computer-aided Manufacturing. 5, 69

CAS Computer-assisted Surgery. 1, 2, 7

CSG Constructive Solid Geometry. 24, 36, 40

CT Computed Tomography. 4, 5

CVDs Cardiovascular Diseases. 1

DICOM Digital Imaging and Communications in Medicine. 4

DOT Diffuse Optical Tomography. 4

DSA Digital Subtraction Angiography. 5

GPGPU General-purpose Computing on Graphics Processing Units. 28, 58

IIS Implicit Interior Structures. 9, 86, 105

IOS Implicit Offset Surface. 73

LUT Lookup Table. 42

MINC Medical Image NetCDF. 4

MIP Maximum Intensity Projection. 7

MIVS Minimally Invasive Vascular Surgery. 1, 2

MLS Moving Least Squares. 26, 36

MPUI Multi-level Partition of Unity Implicits. 25, 36, 45

MRA Positron Emission Tomography. 5

MRI Magnetic Resonance Imaging. 4, 5

NIfTI Neuroimaging Informatics Technology Initiative. 4

NURBS Non-uniform Rational Basis Spline. 26

PDE Partial Differential Equation. 25

PET Magnetic Resonance Angiogram. 4

PSS Point Set Surface. 26

RBF Radial Basis Function. 30, 36, 50

SDF Signed Distance Function. x, 30, 32, 78, 79

TIP Thin Implicit Patch. 9, 69, 70, 73, 81, 104

VOI Volume of Interest. 41

Contents

Abstract i

Acknowledgement iii

Dedication iv

Abbreviations v

1 Introduction 1
- 1.1 Context 1
- 1.2 Geometric Vascular Modelling 3
  - 1.2.1 Volumetric Vascular Imaging Techniques 3
  - 1.2.2 Geometric Modelling 5
  - 1.2.3 Vascular-specific Geometric Representations 6
- 1.3 Aims and Objectives 8
- 1.4 Outline and Contributions 9

2 Related Work 12
- 2.1 Skeleton and Modelling 12
  - 2.1.1 Skeletonisation 13
  - 2.1.2 Skeleton-based Modelling 14
  - 2.1.3 Sweep Surface 15
  - 2.1.4 Skeleton-free Modelling 17
- 2.2 Templates and Model-based Methods 17
- 2.3 Vascular Segmentation 19
- 2.4 Implicit Modelling Techniques 22
  - 2.4.1 An Overview 22
  - 2.4.2 Implicit Function 28
  - 2.4.3 Special Implicit Functions 30
  - 2.4.4 Implicit Object 34
  - 2.4.5 Blending Operation 36
- 2.5 Visualisation Techniques 41

2.5.1 Volume Rendering 41
2.5.2 Surface Rendering 42
2.6 Summary 43

3 Skeleton Marching-based Vascular Reconstruction 45
3.1 Introduction 45
3.2 Skeleton Marching 46
3.2.1 Subdivision of Skeleton 46
3.2.2 Localised Implicit Reconstruction 49
3.2.3 Localised Implicit Object 54
3.2.4 Parallel Computing 58
3.3 Discussion and Experiments 60
3.3.1 Discussion 60
3.3.2 Experimental Results 61
3.4 Summary 66

4 Vascluar Tissue Modelling with Thin Implicit Patch 68
4.1 Introduction 68
4.2 Thin Implicit Patch 70
4.2.1 Implicit Offset Surface 73
4.2.2 TIP as Dual-layer Reconstruction 74
4.2.3 TIP as Approximate Distance 77
4.2.4 TIP as Morphological Implicits 83
4.3 Implicit Interior Structures 85
4.3.1 Implicit Porous Structures 86
4.3.2 TIP with Inner Structures 87
4.3.3 Multi-layer TIP 91
4.4 Discussion and Experiments 93
4.4.1 Discussion 94
4.4.2 Further Experimental Results 96
4.5 Summary 100

5 Conclusion and Future Work 103

References 107

List of Figures

1.1 Flowchart of this Research 10

2.1 The Scalar Field of a 2D Implicit Function 29
2.2 2D Implicit Objects 35
2.3 3D Implicit Objects 36
2.4 Implicit Intersection Blending 39
2.5 Shape-preserving Blending 40
2.6 A Blending between a Square Column and a Plane 41

3.1 Flowchart of Skeleton Marching 47
3.2 Subdivision of a Skeleton 50
3.3 Subdivided Skeleton Segments 51
3.4 Localised Segmentations of a Curvy Blood Vessel 52
3.5 Localised Reconstruction of a Curvy Blood Vessel 55
3.6 Isocontours of an Implicit Function 56
3.7 Globalised Implicit Object and Localised Implicit Object 57
3.8 CPU Fitting Comparison of Blood Vessel Segments 58
3.9 Fitting Speed Comparison of Blood Vessel Segments 59
3.10 Reconstruction of an Unbranched Blood Vessel 62
3.11 Reconstruction of a Branched Blood Vessel 63
3.12 Reconstruction of Blood Vessel Tree 64
3.13 Flowchart of Skeleton Marching on Parallel Computing 65
3.14 Fitting Speed Comparison of Blood Vessels 66

4.1 Diagram of the Structure of an Artery (Britannica 1911) 69
4.2 Flowchart of Thin Implicit Patch 70
4.3 A Simple Thin Solid 71
4.4 Thin Implicit Solid with Non-uniform Thickness 71
4.5 Thin Implicit Solid of Clebsch Surface with Non-uniform Thickness . 72
4.6 Thin Implicit Solid of Bézier Surface with Non-uniform Thickness . . 72
4.7 A Bézier Patch of Utah Teapot 76
4.8 Parametric Surface to Thin Implicit Patch 78

4.9 Comparison between Implicit Function and SDF 79
4.10 Approximate Distance 81
4.11 Thin Implicit Patch with Approximated Distance 82
4.12 Thin Implicit Spout with Approximated Distance 83
4.13 Implicit Dilation 84
4.14 Implicit Erosion 84
4.15 2D Outward Thin Implicit Patch 85
4.16 2D Inward Thin Implicit Patch 85
4.17 Implicit Porous Structures 88
4.18 Porous Structure on TIP of Clebsch Surface 89
4.19 Interior Structures of Real-world Thin Solids 89
4.20 Inner-structured Thin Implicit Patch 90
4.21 Inner-structured Spout 91
4.22 A Simulated Vascular Wall with Multi-layers 93
4.23 The Spout with Multi-layer Interior Structures 93
4.24 Printable Half Teapot 94
4.25 Inner Connection of Spout and Body of the Utah Teapot 95
4.26 Inner Connection of Handle and Body of the Utah Teapot 95
4.27 Thin Implicit Patch of the Utah Teapot 95
4.28 Thin Implicit Patch of a Face 97
4.29 Thin Implicit Patch of a Tibia 98
4.30 Thin-patched Blood Vessel 99
4.31 Blood Vessel with Interior Structures 99
4.32 Branched Blood Vessel with Interior Structures 100
4.33 A Multi-layer Vascular Wall 101

List of Tables

3.1 Distance Error of the Localised Implicit Reconstruction 54
3.2 CPU Fitting of Blood Vessel Segments (seconds) 57
3.3 Fitting Time of Blood Vessel Segments (seconds) 59
3.4 Fitting Time of Blood Vessels (seconds) 66

Chapter 1

Introduction

1.1 Context

Cardiovascular Diseases (CVDs) are a group of disorders of the heart and the blood vessels (World Health Organization 2017), including heart attack, stroke, hypertension, coronary heart disease, angina and dementia (British Heart Foundation 2018). It has been identified as the number one cause of death globally in the World Health Organisation (WHO) report published in May 2017. The death caused by CVDs is 17.9 million in 2016, representing 31% of all global deaths (World Health Organization 2017, 2018). It is anticipated that this number will increase to over 23.3 million by 2030 (Alwan 2011), which makes CVDs remain leading cause of death for a long time.

Although a large number of CVDs are preventable, they are continually rising mainly because of the inadequate preventive measures (World Health Organization 2010). The high-complexity of vascular structures makes the traditional operations on CVDs unsafe or even infeasible. For one thing, blood vessels in CVDs are of variable sizes and curvatures. Their appearances and geometries can be perturbed by stents, calcifications, aneurysms and stenosis, and they are often embedded inside other complex anatomical tissues and organs (Lesage et al. 2009). For another, CVDs exhibit high patient-specific dependence on different situations, such as gender, age, eating habits and living conditions. As a result, the Computer-assisted Surgery (CAS) techniques, such as Minimally Invasive Vascular Surgery (MIVS) technique, are proposed to assist the surgeons on the cure of CVDs (Lepore et al. 2000). As a necessary part of the CAS techniques, the geometric reconstruction of blood vessels prior to the real surgery plays an important role on the minimally invasive vascular surgeries.

The CAS technique is an interdisciplinary field based on medical imaging, virtual reality, micro-technologies and robotics (Kaladji et al. 2012). It is also frequently referred to as computer-aided surgery, computer-assisted intervention, image-guided surgery and surgical navigation (Papademetris et al. 2009). The CAS has dramatically changed the performance of disease diagnoses and surgeries by improving the diagnostic accuracy and the less invasive surgical interventions (Peters 2001).

One of the most fundamental tasks of MIVS is the geometric reconstruction of blood vessels (Lepore et al. 2000). The images of the vessels are collected with imaging techniques and stored as a dataset. During the collection process, the position and grey value information of the scanned blood vessels are stored in the medical image but these pieces information are usually with a discrete manner and cannot represent the blood vessels as a complete geometry. In order to reconstruct the geometric structures of the blood vessels out of the medical image, a certain geometric vascular modelling technique should be proposed to solve this problem.

Geometric vascular modelling is a very challenging task due to the fact that blood vessels are of high complexity in their structures. The deformations, bifurcations and distortion of blood vessels with varieties of sizes and curvatures make the accurate representation of a single blood vessel very hard. Besides, the complicated joints and connections of different blood vessels significantly increase the difficulties of the modelling task.

Although the shapes and structures of the blood vessels are variable and diverse, there are several common geometric features of the blood vessels. First, the shape of a blood vessel is a cylinder-like structure. This structure can be approximated by a collection of templates or models, such as cylinders or cones (Tyrrell et al. 2007; Wu et al. 2011; Zhang et al. 2007). Secondly, a blood vessel is often topologically regarded as a centreline or a skeleton. This is an important geometric clue for the vascular reconstruction which can be used to assist the image segmentation of blood vessels (Bloomenthal 1995b; Lefdal 2016; Smistad et al. 2012). Thirdly, the cross-section of a normal blood vessel is usually a generalised circle. It is straightforward to reconstruct the shape of a blood vessel step-by-step as a series of cross-sections (Kumar et al. 2015). Furthermore, a vascular tree has a large number of blood vessels. Apart from the areas of joints, each blood vessel can be reconstructed geometrically independent of others. A vascular tree can therefore be reconstructed as a composition of many local blood vessel segments (Bloomenthal et al. 1990b; Middleditch et al. 1985). These geometric features of a vascular system are important information for developing high-performance and robust algorithms for reconstructing the geometric structures of a given blood vessel.

Geometric vascular modelling is also an essential task of many other research fields. For example, hemodynamic analysis studies the physical laws of the blood flow in blood vessels. This study requires the accurate geometric structures of blood vessels to be known. The vascular tissue modelling focuses on the fine modelling of the interior structures inside the vascular wall. This modelling is based on the accurately reconstruction of blood vessels. The virtual surgery with interactive editing on blood vessels allows vascular surgeries being operated on the reconstructed blood vessels without a real surgery. Geometric vascular modelling plays a key role during this operation to faithfully reflect the surgery of the cardiovascular diseases in reality.

1.2 Geometric Vascular Modelling

Geometric vascular modelling aims at extracting geometric information of the blood vessels from a given medical image using a certain vascular medical imaging technique. It is related to the volumetric vascular imaging techniques, geometric modelling techniques and the geometric representation of blood vessels.

1.2.1 Volumetric Vascular Imaging Techniques

The preliminary requirement of geometric vascular modelling is the acquisition of volumetric medical images of different digital imaging modalities (Kishore et al. 2013). A volumetric medical image is a 3D image scanned from a part of the whole human body. By using image visualisation and geometric modelling techniques, a virtual and visual model can be created from a given medical image for geometric and biological analysis and researches. The visualisation and modelling techniques can be used either before the surgery to simulate the whole surgical process and reduce the surgical risk (Oentoro 2009) or during the intra-operative stage to give a visual assistance for the surgeons (Taylor et al. 2002).

A medical image is a representation of the internal structure or function of an anatomic region in the form of an array of picture elements called pixels or voxels (Larobina et al. 2013). A medical image can be captured by different imaging techniques. The X-ray imaging technique is the oldest imaging method invented to detect the hard matters inside the human body (Cox et al. 1896). But it does not produce true 3D medical images. The true 3D imaging modality were absent until modern 3D imaging techniques were developed. These techniques can produce image data as well as their descriptive information, such as Computed Tomography (CT), Magnetic Resonance Imaging (MRI) and Magnetic Resonance Angiogram (PET) scanners. A CT scanner combines an X-ray device with a computer, emits X-rays around the patient to penetrate human body from different directions. These X-rays are fed into computer to bring the information together into a picture of the body. An MRI scanner is a tunnel-shaped piece of equipment, where a patient lies on a table that slides into the scanner with the body being surrounded by a magnetic field. Signals are generated from the magnetic field and fed into a computer to create a picture of the body (Kim et al. 2000). A PET scanner detects parts of gamma rays emitted indirectly by positron emission radionuclide tracer and produces 3D image of functional processes of scanned body. It is a nuclear medicine technique (Das 2014). There are several other kinds of medical imaging techniques, Diffuse Optical Tomography (DOT) (Boas et al. 2001) and ultrasound for instance, to acquire images from part of the human body. No matter what imaging technique being used, the scanning results are stored in medical images and these images require further investigation and analysis to extract geometric and biological information.

A medical image is usually stored in a discrete dataset. It contains the geometric information of the scanning object, descriptive information of patient identification and demographics, as well as the technical information of the examination, series and slices. The commonly used medical image formats are Analyze format, Neuroimaging Informatics Technology Initiative (NIfTI) format, Medical Image NetCDF (MINC) format and Digital Imaging and Communications in Medicine (DICOM) format (Larobina et al. 2013).

A medical image is a structured dataset. This dataset contains topology, geometry and attribute information to represent and implement the objects hidden inside the image. Topology is a set of properties of an object with certain geometric transformations (Weiler 1986), such as triangle, vertex, line and their transformations. Geometry is the instantiation of the topology. It is the specification of a 3D form such as point coordinates of a triangle (Schroeder et al. 2005b). Attributes are supplemental information of the dataset structure, including scalars, vectors, normals, texture coordinates and tensors. Together with the topology and the geometry, this information is to be modelled to represent the objects hidden inside the images.

The image-based modelling applies clinical information and dataset extracted from the medical image to visualise and reconstruct the specific tissues of the image for the purpose of geometric and biomedical analysis and processing.

A medical image is the input of the image-based modelling, which extracts, visualises and reconstructs the region of interest out of the medical image. The image-based modelling aims at the representation of specific tissues in the medial image, such as bones, skins, blood vessels and so forth.

In terms of blood vessels, the vascular images are captured by vascular imaging modalities. In order to visualise the inside of the blood vessels, angiography is normally used in the vascular imaging techniques. There are mainly three types of angiography, X-ray angiography, Positron Emission Tomography (MRA) and CT angiography (Christie et al. 2014; Herrick et al. 2004; Kishore et al. 2013). The X-ray angiography is the traditional way to capture the image of blood vessels. A radio-opaque contrast agent is usually injected into the blood vessel such that the lumen of the blood vessel can be imaged with X-ray based techniques. With the development of digital techniques, Digital Subtraction Angiography (DSA) is introduced on the X-ray angiography to give better visualised blood vessels (Mistretta et al. 1981). However, since the contrast agent is potential for nephrotoxicity and the X-ray is harmful to the human body, the X-ray angiography is much less used than before. The MRA is one of the most used vascular image techniques today. It combines the advantages of DSA and MRI together to gain the fully anatomical 3D image of blood vessels (Hartung et al. 2011). In contrast with the X-ray method, the MR angiography is not invasive because no intra-arterial puncture is required. Besides the vessel lumen, it can examine the vessel wall and surrounding structures. This allows the detection of inflammation and oedema of the vessels wall. The CT angiography is able to capture the 3D images of the blood vessels and the surrounding structures. It gives a huge space on the image processing and analysis techniques on the research of blood vessels. Small and deformed blood vessels and vascular diseases can be visualised with this technique. It is a promising technique on the vascular image modalities.

1.2.2 Geometric Modelling

Geometric modelling is a branch of applied mathematics and computational geometry on the description of geometric shapes. It is usually about the study of techniques and algorithms relating to specifying geometric shapes in the 2D and 3D spaces in terms of points, curves, surfaces, solids, functions and other techniques. It is widely used in a variety of different areas such as Computer-aided Geometric Design (CAGD), reverse engineering, real-world shape reconstruction, Computer-aided Manufacturing (CAM), geometric information processing, image processing, molecular modelling, computational fluid dynamics, computer graphics, computer animation and so forth (Gallier 2018; Mortenson 1997).

Based on the representation form of a geometric model, geometric modelling can be categorised as wireframe modelling, surface modelling, solid modelling (Weiler 1986) and function-based modelling (Pasko et al. 2002a, 1995). Wireframe modelling is one of the earliest geometric modelling techniques, which represents a geometry using points and curves on the objects. Surface modelling is the most used geometric modelling technique. The shape of a geometric object is mathematically described and represented as a set of surfaces. These surfaces are graphically displayed but may not be geometrically connected. Since each surface is independent of the others, the integrity checking features are absent. Solid modelling represents a geometric object in the form of solid (Hoffmann 2004). The solid is a boundary-based volume with a closed surface. Compared with surface modelling, the inside and outside of the solid are divided by this closed surface. Other geometric properties of the solid, such as the centre of gravity, can also be analysed. Function-based modelling represents a shape by using a scalar field function. A level set of the function is regarded as an implicit surface and this surface divides the volume into two implicit solids. The set-theoretic operations are commonly used in function-based modelling to make very complicated geometric shapes.

Geometric modelling techniques can also be classified into two groups: explicit modelling techniques and implicit modelling techniques, according to whether a geometric representation can explicitly provide the points on the geometry. Explicit modelling typically represents a 3D object as point clouds, a wireframe or a triangle mesh. Although it is a preferred approach for the purpose of visualisation, explicit techniques are very inconvenient at combining geometric shapes and handling branched structures (Bloomenthal 1995b). In contrast, implicit modelling represents a geometric object implicitly in the form of field functions, which can be easily blended together to generate more complicated geometries. Since a vascular tree is with complicated shapes, implicit modelling is the favoured method for geometric vascular modelling tasks (Bloomenthal et al. 1997; Li 2007).

1.2.3 Vascular-specific Geometric Representations

Depending on the accuracy required in an application, a blood vessel can be represented geometrically in many ways, such as vascular skeleton, a combination of models and image segmentation results. A vascular skeleton is the supporting structures of blood vessel trees (Preim et al. 2014). With the skeleton, a blood vessel can be represented as a group of blobs (Wyvill et al. 1998; Yureidini et al. 2012) or reconstructed as the approximation of sweep surfaces (Hong et al. 2012; Kretschmer et al. 2013). In some research works, a blood vessel is modelled locally using some simple geometric primitives, such as cylinders, cones and spheres. Together with some vascular geometric information extracted from a given medical image, the combination of these models is an effective way of representing blood vessels (Zhang et al. 2007). The image segmentation of a vascular image aims at identifying the region of blood vessels by separating them from other tissues (Antiga 2002). The grey value and position of the voxels in the region are identified and recorded. Although blood vessels can be represented as the boundaries of the identified region, the segmentation result is far less accurate to present the geometric structures of a blood vessel (Lesage et al. 2009).

The visualisation of volumetric data containing blood vessels plays an important role in the research of geometric vascular modelling. In some cases, when the visualisation of the blood vessels is the main purpose of vascular modelling task, explicit extraction of geometric information is in general not required (Hahn et al. 2001; Preim et al. 2008; Schumann et al. 2007). The most commonly used vascular visualisation techniques are volume rendering, isosurface extraction (Lorensen et al. 1987) and Maximum Intensity Projection (MIP) (Oeltze et al. 2005). Volume rendering gives a good visual result of the volume dataset, but small vascular structures may be distorted or disappeared due to the low resolution of the original dataset (Pommert et al. 1992). Vascular visualisation using the isosurface extraction method can produce iso-value surfaces from the medical image but it usually fails to hold the small vascular structures to be connected as a complete tunnel when the vascular periphery is inhomogeneous and the adjacent organs are with similar imaging properties (Hahn et al. 2001). MIP projects the voxels of medical data in a visualisation plane with maximum intensity such that the medical image is rendered as a 2D image. It is a rather simple way of visualisation but cannot correctly reflect depth relations and small structures may not be rendered (Preim et al. 2014).

Although visualisation technique renders blood vessels in a visualised way and gives an interactive user interface to manipulate the blood vessels hidden inside the medical images (Hansen et al. 2005), it presents no geometric information of the blood vessels and is regarded as a complement of geometric vascular modelling. As a matter of fact, it is insufficient to visualise the blood vessels without the geometric vascular structures in applications concerning Computer-assisted Surgery (CAS). These applications require an accurately reconstructed geometric structure of the blood vessels to assist the surgeries in reality.

1.3 Aims and Objectives

Geometric vascular modelling has been widely investigated by a variety of approaches and researches. Although applications on geometric vascular modelling have achieved great progress in the past two decades, it is still a challenging task to faithfully reconstruct the geometric structures of blood vessels with high accuracy and high performance. For one thing, a vascular tree is with high-complicated reticular formations. Stenosis, aneurysm, thrombosis, atherosclerosis and other deformed irregular pathological parts make them even more complex in their geometric structures. It is extremely challenging to accurately represent the geometric structures of a vascular tree in an effective manner. For another, blood vessels are made of soft tissues with various shapes, complex branches and different sizes. The high-accuracy reconstruction of the complicated vascular tree is inherently difficult and computationally expensive. It is urgently required to optimise this reconstruction to improve the modelling performance. What is more, a blood vessel is a lumen with a thin wall. This wall is a multi-layer thin solid with a thickness which cannot be effectively represented as a geometric surface, since a geometric surface has no thickness. However, the existing geometric vascular modelling techniques reconstruct the blood vessels as surface-based geometric shapes without the faithful representation of the real-world blood vessels. A vascular tissue modelling technique is required to overcome this shortage.

A good geometric vascular modelling technique should be able to provide high accuracy and high performance on the geometric representation of complicated vascular trees and give interior structure descriptions of the vascular wall. This research aims to develop a state-of-the-art patient-specific medical image-based vascular geometric modelling technique to solve these problems. More specifically, this research will focus on the following three areas:

- High-accuracy geometric representation of the complicated vascular system. A blood vessel can be reconstructed in many ways. The model-based method uses templates to simulate the shapes of blood vessels and gives hemodynamic analysis on them. The modelling result is represented with parametric surfaces but the result is too ideal to describe the shapes of blood vessels in reality. Instead of using the templates, the sweep surface method applied the vascular segmentation on the reconstruction of blood vessels and gives a much better result. However, its reconstruction accuracy can only be guaranteed at the data points on the cross-sections of the sweep surface. The reconstructed blood vessel between two neighboured cross-sections of the sweep surface is an approximation and cannot accurately represent the original vascular shape. In this research, the Localised Implicit Object is proposed to replace the sweep surface on the vascular skeleton, which accurately reconstructs the shape of a section of a blood vessel without ignoring the data points on it. The accurately reconstructed vascular sections are then combined together using the shape-preserving blend operations to form a complete vascular tree.

- High-performance computation geometric vascular reconstruction approach. Although the sweep surface method has been used to reconstruct the geometric structures of blood vessels, its computation is very heavy for large modelling task. On the one hand, albeit the sweep surface method has been successfully applied on vascular modelling and achieved satisfactory accuracy on the cross-sections of the sweep surfaces, but extra operations on coordinate transformation and ordering of the data points on cross-sections limit the performance fo the modelling. The accuracy out of the cross-sections is unguaranteed. On the other hand, the sweep surface method is a two-step modelling technique. The data points on a cross-section of the sweep surface have to be approximated to be generalised circles first and many consecutive generalised circles are then being fitted into a generalised cylinder. This research proposed the Skeleton Marching technique to avoid this inefficiency. With the localised implicit object, many sections of blood vessels are directly reconstructed from the data points of blood vessels. Since this direct reconstruction is parallel computing friendly, the performance of the proposed method is significantly improved.

- Tissue modelling of the interior material structures inside the vascular wall. The wall of a blood vessel is very thin but also with interior structures. The surface-based vascular modelling treats the vascular wall as a surface rather than a thin solid, which neither correctly reflects the physical truth nor can be printed out using additive manufacturing techniques for further research. As a solution, this research proposes Thin Implicit Patch (TIP) and Implicit Interior Structures (IIS) to model the geometric structures of tissues inside the vascular wall. Various structures can be embedded inside the vascular wall with simple implementation and cheap computation. It gives a new idea on solid modelling and additive manufacturing applications.

1.4 Outline and Contributions

In this research, the geometric vascular structure is implicitly reconstructed out of volumetric vascular images with parallel computing accelerations. The wall of a blood vessel is implicitly modelled as a thin solid with interior structures to represent the vascular wall in the real world. Figure 1.1 illustrates the process of this research.

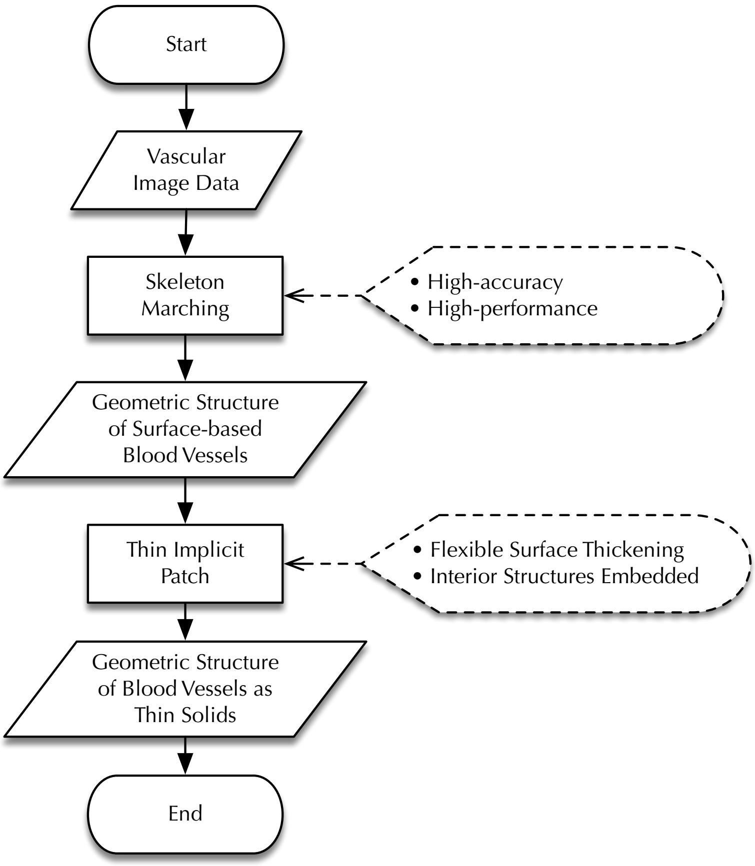

Figure 1.1: Flowchart of this Research

The rest of this thesis is structured as follows:

Chapter 2 discusses the related research background. The vascular modelling techniques are firstly reviewed in several different aspects concerning vascular systems, skeletonisation, segmentations and localisations, and common models and templates used in vascular modelling. Then the key techniques of implicit modelling are discussed, including the conception of the implicit object, the flexibility of the implicit blending operation and the brief discussion of the implicit surface modelling techniques.

Chapter 3 discusses the high-performance computation geometric vascular reconstruction based on implicit modelling techniques. This is the main contribution of this research. A parallel technique called Skeleton Marching is proposed for fast reconstruction of blood vessels. Long and complex blood vessels are divided into short and simple vessel segments guided by the shape of the skeleton, then small point clouds are collected with localised segmentation method, which are then fitted in parallel with a set of implicit surfaces. A complex vascular tree is finally constructed by blending these objects together. This vascular modelling divides large implicit modelling task into small independent sub-tasks and makes them work simultaneously. With the shape-preserving blending operation, this vascular modelling can generate high-accuracy geometric vascular trees.

Chapter 4 investigates the thickening technique of geometric surfaces for modelling a real-world vascular tissue. This is another contribution to this research. The implicit offset surface is proposed to convert a surface to an implicit thin solid. Several construction methods of implicit offset surface are proposed. This offset surface can be applied to both parametric and implicit surfaces to convert them to be thin implicit solids. Inside these thin solids, interior structures can be embedded to simulate the internal composition of real-world 3D objects. In this way, a blood vessel with a thin vascular wall can be printed out such that the reconstruction of the vascular tree is not only visualisable and touchable but also producible and manufacturable.

Chapter 5 gives a conclusion of this research and discusses the future work.

Chapter 2

Related Work

The research of image-based geometric vascular modelling involves many aspects. This chapter discusses the related works including skeletonisation, model-based methods, vascular segmentation and the implicit modelling techniques.

2.1 Skeleton and Modelling

A skeleton is the supporting structure of an organism when talking about geometric medical image modelling (Preim et al. 2014). For vasculatures, a skeleton is usually a centreline which is identified as the locus of the centres of maximal spheres inside the vascular structure (Hong 2013). But a vascular skeleton can be another path inside the blood vessel rather than the centreline, as long as it represents the geometric topology of the vasculatures. Skeletonisation is the process of locating skeleton of vasculatures. With respect to the innate property of natural representation on a solid object, the combination of skeletonisation and implicit techniques is particularly suitable for natural form modelling (Antiga et al. 2003). Most vascular reconstruction techniques are skeleton-based because it is natural and easier to build a tunnel-shaped structure with the guidance of the skeleton. For example, the arterial path line generated with skeleton-based modelling can be used to construct a 3D solid fluid computational model (Hossain et al. 2011). But in some situations, such as small local region or simple geometries, a skeleton may not be necessary and skeleton-free method plays a more important role (Liang et al. 2013).

2.1.1 Skeletonisation

Skeletonisation is a powerful tool for the compact description of shapes and planning of paths. In most cases, it is to find the skeletons out of a medical image.

Zhou presents an efficient skeletonisation algorithm of 3D medical images. The skeletons are interpreted as connected centrelines which consist of medial points of consecutive clusters (Zhou et al. 1999). Telea presents a simple and robust skeletonisation algorithm for arbitrary 3D objects (Telea et al. 2002). This method is based on the Fast Marching Method (FMM) by computing the parameterised boundary location of every pixel. Lower memory costs and shorter running times are required of this method for both 2D and 3D applications. Antiga presents a robust and accurate method to get the centrelines of tubular objects. This method solves the Eikonal equations on the Voronoi diagram to find the centreline. It has been used on the 3D modelling of vascular segments (Antiga et al. 2003). Bühler surveys the geometric methods of visualisation and qualification on centreline computation, boundary dictation projection techniques and geometric model generation out of the vessel data (Bühler et al. 2004). The extraction of retinal centreline is an important application of skeletonisation of medical images. Sofka proposes a new technique for extracting vessels of retinal images (Sofka et al. 2006). The central idea of this method is the combination of matched-filter responses, confidence measures and vessel boundary measures. It is an efficient and effective vessel centerline extraction algorithm. The interactive extraction of the centreline of a tubular object is an effective way of skeletonisation. Zhang describes a user-steered method for interactive centreline tracking. This method has been used on coronary artery tracking (Zhang et al. 2008).

The skeletonisation can be accelerated by GPU computing. Smistad presents an airway segmentation and centreline extraction method implemented with GPU acceleration. This method significantly reduces memory usage and processing time (Smistad et al. 2012). The GPU-accelerated segmentation and centreline extraction of coronary arteries is also discussed in Lefdal's thesis. Different methods and approaches are compared and a suitable method is chosen for the parallel implementation (Lefdal 2016).

A skeletonisation with less manual operations is expected for high-performance computation vascular modelling. Kumar presents a novel semi-automatic method for the segmentation and centreline extraction of blood vessels (Kumar et al. 2015). A user-initiated seed is required at the end of the blood vessel tree and the 3D cross-section analysis is done by single-scale or multi-scale circle enhancement filter to track the trunk and bifurcation of the blood vessel. This method can be combined with an optional active contour post-processing to improved the accuracy of the extraction.

Machine learning can be used on the skeletonisation of vascular structures. Bates proposes a method to extract the centreline of the vessels using Convolutional Neural Networks. The Convolutional Long Short-Term Memory units (ConvLSTM) is used to extend the 2D centrelines to be 3D forms in anisotropic and complex microscopy images. Both 2D and 3D convolutional comparators are effective of this hybrid convolutional-recurrent architecture (Bates et al. 2017). A similar topic on deep feature extraction of vessel segmentation and centreline prediction can be found at (Tetteh et al. 2017). Machine learning for pixel classification tasks is applied in this paper.

2.1.2 Skeleton-based Modelling

One of the earliest work on combining implicit modelling with skeletons can be found at (Bittar et al. 1995). In this paper, the author uses medial axis and implicit surface to reconstruct 3D solid from an unstructured point set. Smooth freeform solids can be generated with this method. Bloomenthal focuses on the skeletal design of natural forms in his dissertation (Bloomenthal 1995b). The geometries from real-world objects can be mimicked by the design of geometric shapes guided with the skeletal design. This paper deeply discusses the techniques of implicit modelling and the design of skeletal objects. No geometric reconstructions are mentioned. Cani-Gascuel applies the idea of skeleton on the implicit surface design and animation (Cani-Gascuel et al. 1997). The articulated skeletons coated with implicit flesh are used to make the animation of simple characters, and the the specific properties of implicit surfaces are used to maintain the constant volume of the animation.

Skeleton-based implicit surfaces allow interactively design and display curved models. Cani focuses on the surfaces with skeletons as graphs of interconnected curves and presents a new solution of interactive implicit modelling called subdivision curve primitives. The surfaces can be efficiently and correctly displayed using local meshes around the curves. This method can be used to represent different levels of details of the model (Cani et al. 2001).

A practical application of the skeletons on vascular modelling are the reconstructions of vasculatures. Selle presents a group of methods for the geometrical analysis of vessel systems based on row medical images (Selle et al. 2002). The skeletons of the vessels are determined after the image segmentation, and the structures of the partial veins and their vascular territories are approximated with different methods. This is a successful application of skeleton-based modelling, but the the modelling results are not precise for further geometric analysis.

Angelidis proposes a skeleton represented as interconnected subdivided curves and surfaces to control the shapes of the model (Angelidis et al. 2002). The level of the subdivision of the skeleton determines the level of the details of the implicit surfaces. A new solution of avoiding the unwanted blendings is also proposed. The skeleton can be used for the interactive modelling of user-defined strokes. Alexe extracts the skeleton of a 2D contour to define an implicit surface that fits the contour. The 3D shape is reconstructed from the implicit surface with a natural aspect. This method is accessible for fast and easy shape prototyping (Alexe et al. 2004). Allegre presents a hybrid modelling frame work called HybridTree for the modelling of complex 3D objects (Allègre et al. 2006). It combines skeletal implicit primitives, triangle meshes and point set models in a coherent fashion. Both the advantages of triangle meshes on local deformation and the flexibility of implicit surfaces on combining shapes are utilised in this method. In order to efficiently reconstruct the surface model of blood vessels, Yureidini proposes a new implicit modelling consists of local implicit surfaces generated by blobby models on skeletons. An energy function is used to replace the original blob for the reconstruction. It is a very efficient reconstruction of blood vessels (Yureidini 2014; Yureidini et al. 2012). Skeleton-based implicit surfaces can be decorated with geometric details. Zanni applies Gabor noises on the skeleton-based implicit surfaces and creates enhanced implicit primitives without blurred details (Zanni et al. 2012).

2.1.3 Sweep Surface

A typical application of skeletonisation is sweep surface, which is a natural idea of building vascular structures. It generates a set of 2D vascular contours and then composes them together using different techniques. This idea can also be applied on a volume rather than a surface. Wang presents a method for modelling the sweep volume from a moving solid. This is one of the earliest research in this field (Wang et al. 1986). Schroeder presents an implicit modelling technique on the generation of sweep surfaces and volumes (Schroeder et al. 1994). This method is applicable for any geometric representation with a distance function. It is used on the maintainability design and robot path planning. Zhang reconstructs the patient-specific vascular geometric models using hexahedral solid NURBS for isogeometric analysis

(Zhang et al. 2007). The skeleton-based sweeping method is used to construct the hexahedral control meshes. This method uses templates to simulate the geometries of blood vessels, therefore the reconstruction cannot achieve high accuracy.

A successful application of skeleton-based vascular modelling with sweep surfaces can be found in the conception of bivariate implicit spline. Based on it, Hong develops a high accurate implicit geometric representation of vascular trees from given volumetric medical dataset to reconstruct high accurate implicit cylinders with arbitrary cross sections (Hong et al. 2012). Hong demonstrates that skeletal curve is the best way to represent topology of vasculatures, because of its complexity and naturally representation of complicated structures such as 3D context. Firstly they make a simple coordinate transformation from Cartesian space to Frenet frame space which consists of binormal, normal, and tangent. Then they represent implicit specification of freeform cross section by using 2D piecewise algebraic splines (Li et al. 2009). Along skeleton with variable cross sections, they construct freeform implicit cylinders in Frenet frame space, but without bifurcations permission. A blending function is introduced to reconstruct the branched blood vessels with flexible blending range control. This blending function is a piecewise polynomial shape operator which has smooth distributions on any required degree. Their work starts with a pre-segmented data so that the reconstruction result heavily relies on the accuracy of segmentation.

Kretschmer gives a similar solution of the skeleton-based vascular modelling (Kretschmer et al. 2013). This paper presents a solution of interactive implicit vascular modelling techniques, including how to convert vascular contours to 2D implicit sweep template for sweep surface generation, how to eliminate undesirable bulges in blending but preserve the original shapes meanwhile, and how to locally update the model interactively. This paper develops vascular modelling in three steps. (1) Implicit description of polygons by using precomputed implicit representations to abridge computation complexity, and construction of sweep template by Catmull-Rom spline (Twigg 2003). (2) Defining the implicit sweep using Frenet frameworks to convert the world coordinate to tangent coordinate, and doing interpolation because the sweep templates are sparse. (3) Using gradient-base blending operations to smooth and eliminate bulges (Gourmel et al. 2013).

Sweep surface has several limitations. Firstly, there are two extra operations of sweep surface method: indispensable coordinate transformation for orthogonality between the blood vessel and the sweep surface, and unavoidable points sorting up on the cross-sections for spline approximation. These operations reduced the performance of the modelling. Secondly, the density of cross-sections influences the reconstruction. Data points between two consecutive cross-sections are ignored. The larger the density of the cross-sections, the better the modelling quality. Lastly, vascular modelling based on sweep surface uses two-step approximation. Cross-sections are firstly approximated as a series of closed splines, then these splines are approximated as a generalised cylinder. Modelling performance will decrease with this two-step operation.

2.1.4 Skeleton-free Modelling

The skeleton is not indispensable for surface modelling when the modelling is regarded as a general object. Liang reconstructs the implicit surfaces from point clouds of tubular objects (Liang et al. 2013). The modelling space is divided into the interior region and the exterior region by a boundary surface fitted from the data points. The anisotropic Gaussian function with signed distance functions is used to smooth noises and solve the non-uniform open boundaries. The tubular experiments in this paper do not require skeletons, but this method is hard to apply on complicated vasculatures, especially the tiny and complicated parts such as capillaries.

The famous marching cube method can also be regarded as a skeleton-free modelling (Lorensen et al. 1987; Newman et al. 2006). This algorithm creates triangles of constant density surfaces from medical images. A case table is made by the divide-and-conquer approach to generate inter-slice connectivity. By maintaining the inter-slice connectivity, the surface of the 3D object hidden inside the medical image is constructed. This method has been a standard of the surface visualisation of medical images. However, it is more a visualisation method rather than a reconstruction method. The surfaces generated by this algorithm is far accurate from the requirement of geometric analysis.

2.2 Templates and Model-based Methods

Blood vessels are geometric objects with long thin shapes. A single blood vessel can be regarded as a generalised cylinder, and the junction of different blood vessels also has specific shapes. A model-based vascular modelling uses geometric models and templates to simulate the different shapes of blood vessels (Schumann et al. 2007). In contrast, a model-free vascular modelling has no template assumptions but uses other techniques, such as vascular segmentation, to reconstruct the blood vessels (Preim et al. 2008).

The model-based vascular modellings are usually used for vascular decomposition and classification or the analysis of blood current. Agin studies the representation and description of curved objects with simple geometric primitives. The joints of these primitives are also discussed. This is one of the earliest work on the modelling of generalised cylinders (Agin 1972). Hahn describes a pipeline of image procession for the symbolic models of vascular reconstruction (Hahn et al. 2001). A blood vessels is regarded as a truncated cone and different cones are smoothly blended at the branching joints. This pipeline is proposed for the visualisation of the vasculatures and aims at medical education and therapy planning. Frangi reviews the 3D modelling for functional analysis of cardiac images. This review surveys the research of cardiac modelling for two decades and conclude that the 3D model-based modelling can improve the diagnostic value of cardiac images (Frangi et al. 2001).

A template sweeping along the skeleton of a blood vessel can be treated as a model-based vascular reconstruction. In the paper of (Antiga et al. 2003), the author mainly discusses how to compute the centrelines of blood vessels but also mentions the blood vessel model generated from a sweeping maximal inscribed ball along the vascular centreline .

Zhang proposes a model-based vascular reconstruction for isometric analysis (Zhang et al. 2007). Image processing techniques are firstly use to improve the quality of input image data, then templates are designed to match different shapes of blood vessels along the vascular skeletons. NURBS meshes are used to generate the surface of the blood vessels based on a variety of templates. This is a typical model-based vascular modelling method.

Wang presents an extension algorithm to repair the segmentation flaws of cerebrovascular structure with G^2 continuous Ball B-spline curve (Wang et al. 2016). The Ball B-spline is good at representing tubular structures and gives out model-based vascular tree with smooth joints. This method can be regarded as a vascular modelling technique.

Priem overviews the visualisation techniques on vascular structures, including volume rendering and surface rendering (Preim et al. 2008). Particularly, this paper distinguishes model-based approaches and model-free approaches. The model-based methods create ideal easy-to-interpret visualisation with model assumptions, while the model-free methods represent the data with a more faithful way. Interaction techniques and virtual angioscopy are also discussed. Another review of model-based vascular modelling can be found at Urick's work (Urick et al. 2017). This paper reviews the literature on patient-specific arterial network modelling. One of the main steps of the modelling mentioned in this paper is the analysis of suitable model generation. NURBS is used for the isogeometric finite element analysis in the examples of the paper.

2.3 Vascular Segmentation

A model-free vascular modelling usually uses image segmentation to assist the geometric reconstruction of blood vessels. Image segmentation is one of the most important techniques of image information extraction. It partitions an image into distinct constituent subregions, which are homogeneous with some defined characteristics (Drever et al. 2007). Conventionally, segmentation is the prerequisite of reconstruction (Hong 2012; Yureidini 2014; Zhang et al. 2007), but there are also some segmentation-free approaches for the task of vascular modelling (Kretschmer et al. 2013). This means blood vessels may be reconstructed in a more natural way than the segmentation-based method.

Region growing segmentation is a robust image segmentation algorithm for freeform regions (Adams et al. 1994). Based on the region growing technique, Masutani develops an algorithm to acquire the topological information of tree-like objects such as vascular shapes (Masutani et al. 1996). This algorithm extended the theory of mathematical morphology for closed space inside binary shapes. The superior features such as parametric controllability can be shown. Similar with the region growing method, Xu develops the gradient vector flow (GVF) for active contours (Xu et al. 1997). The GVF computes the gradient vectors of a gray-level map from the image as the external force. This new external force does not require initialisation but can get fine convergence to concave boundaries.

Antiga discusses the patient-specific modelling of large arteries in his dissertation (Antiga 2002). Various 3D modelling of vascular structures are addressed in this thesis, such as snakes and level set. Computational geometry techniques are developed to solve segmentation, reconstruction and other specific problems of 3D modelling of vasculatures. Fluid-dynamics analyses are discussed in the paper.

Selle's method for geometrical and structural analysis of vessel systems is a skeleton-based and segmentation-based reconstruction for lier surgical planning (Selle et al. 2002). After the segmentation of the vessels, the geometrical and structural shapes of the vessels are analysed with the assistance of the vascular skeletons. The vascular territories are approximated with different methods and visualised with graphics primitive fitted to the skeleton.

The application of convolution surfaces on the modelling of vasculatures produces excellent visualised results. Based on this application, Oeltze presents a visualisation method for the vasculatures inside medical images (Oeltze et al. 2005). Using the skeleton and the diameter information as in put, this method produces smooth transitions at branchings and closed rounded ends with convolution surfaces. Although very smooth blood vessels can be visualised, this method lacks of accurate geometric information of the vessels.

Vessel segmentation algorithms are surveyed in detail in Kirbas' review (Kirbas et al. 2004). This review surveys vessel segmentation algorithms into several categories: pattern recognition techniques, model-based approaches, tracking-based approaches, artificial intelligence-based approaches, neural network-based approaches, and miscellaneous tube-like object detection approaches. This is one of the most detailed reviews on the problem of vessel segmentation.

Boskamp reviews how to analyse and visualise blood vessels of medical images (Boskamp et al. 2005). The key techniques of vascular modelling, including segmentation, skeletonisation, topological and morphometrical analysis methods are all discussed. A number of clinical and medical applications are described in this paper.

One of the most general reviews of vascular segmentation can be found at (Lesage et al. 2009). In this paper, the authors review the literatures of vascular segmentation from the views of models, features and extraction schemes. The model assumptions of the vessel appearance and geometry can be embedded in the segmentation approaches, the image features are used to evaluate the models, and the extraction schemes combining the model and the feature is discussed to perform the segmentation task.

Schumann presents an accurate and high-quality model-free reconstruction of vascular structures (Schumann et al. 2008). A point cloud is firstly extracted as the result of a segmentation. The signed distance field is generated by using Multi-level Partition of Unity Implicits (MPUI) and then polygonised with a surface tracking approach. This method makes a good tradeoff between the accuracy and smoothness.

Antiga presents a vascular modelling framework for computational hemodynamics (Antiga et al. 2008). The techniques of image processing, geometric analysis and mesh generation are used in this framework. This paper proposes implicit deformable models for the image segmentation task. This is a novel approach for segmentation on vascular images. Selective initialised points of blood vessels are used as a strategy for this segmentation. This framework is a part of the open source software Vascular Modeling Toolkit.

Taylor describes the patient-specific modelling of cardiovascular mechanics (Taylor et al. 2009). After the acquisition of patient-specific anatomic and physiologic data, image segmentation and image-based geometric modelling are used to reconstruct the geometry of the vascular tree. The reconstruction is represented as an automatic mesh generation. This is a new application of cardiovascular mechanics.

Wu proposes a technique to accurately obtain the vascular structure of patient-specific vasculatures (Wu et al. 2011). An accurate and smooth centreline step is firstly applied to fit the cross-sections of blood vessels. A level set method is then used to segment the vessels out of the medical image. The segmentation results are used to reconstruct the surface of the blood vessel by generating a set of topologically preserved quadrilateral patches. This method receives a good balance on smoothness, number of triangles and distance error.

Shang presents a novel active contour model for the segmentation of vessel tree (Shang et al. 2011). A region competition-based active contour model is firstly introduced to segment the thick vessels. Then a vascular vector field is defined to evolve the active contour along the centreline for the thin and weak vessels. A dual curvature strategy is finally used to smoothen the surface of blood vessels without changing the shapes. This method is accurate and robust for the automatic extraction of blood vessel trees.

Hong's vascular modelling technique gives high-accuracy high-smoothness vascular geometries (Hong 2012, 2013; Hong et al. 2012, 2015). This method is a skeleton-based, segmentation-based and model-free implicit vascular modelling technique.

One of the latest work of vascular modelling with image segmentation and implicit modelling can be found at (Kerrien et al. 2017). Both the segmentation and reconstruction of the vasculature are addressed in this paper. The segmentation is based on an original tracking algorithm which filters the points extracted from the vessel surface surrounded the centreline. Blobby models are used to automatically reconstruct each local unstructured point set along the centreline. The vascular tree is a new model of the local implicit models.

Several other model-free vascular modelling techniques mentioned in previous sections also use segmentation results to achieve the reconstruction of blood vessel (Kretschmer et al. 2013; Kumar et al. 2015; Yureidini 2014; Yureidini et al. 2012). In contract with the model-based methods, the model-free methods generate more faithful blood vessels rather than idea geometric shapes. However, the quality of segmentation results directly determines the precision of the reconstruction results.

2.4 Implicit Modelling Techniques

In order to accurately reconstruct the structure of a complicated vascular tree, a correct geometric representation of the structure plays an essential role. Considering the various shape of a single blood vessel and the complex joints of the branched vascular tree, the implicit modelling is the favoured modelling technique. On the one hand, implicit modelling is good at representing freeform objects. An implicit function can be either with concise expression to give simple shapes or with a careful configuration to give complex implicit objects. Each part of the blood vessel, no matter whether it is straight or curvy, thick or thin, long or short, can all be effectively represented. On the other hand, an implicit object with complex shape can be efficiently represented by combining implicit objects with simple shapes. By using the shape-preserving blending operations, the shapes of the vascular joints can be preserved as much as possible to the original data points. As a result, the accuracy of the implicit modelling can be guaranteed. The rest of this chapter discusses implicit modelling and related techniques.

2.4.1 An Overview

A geometric object can be represented in the form of implicit functions, relevant geometric modelling techniques developed based on this idea is called implicit modelling (Gomes et al. 2009). In general, a scalar function can be used to represent any attribute associated with a geometric object across a 3D volume, not just about its geometric shape. Implicit modelling technique is also referred to as solid modelling (Hoffmann 2004; Hoffmann et al. 1991; Lim et al. 1995; Shapiro et al. 1999), volume modelling (Kaufman et al. 2005), level set methods (Museth et al. 2002; Osher et al. 2006; Shang et al. 2011; Zhao et al. 2001) or F-reps (Function Representation) (Bernhardt et al. 2010; Menon et al. 1996; Pasko et al. 1995), depending on the context in which the technique is applied.

Implicit modelling was given less attention by the researchers of computer graphics before the 1980s (Foley et al. 1982). Sabin proposes the use of potential surfaces for the description of arbitrary surfaces. This is one of the pioneer works on implicit modelling, where the zero-value of the scalar function is regarded as the implicit surface of a potential field. In addition, some Implicit blending operations are discussed in this paper (Sabin 1968).

Ricci introduces the concepts of the intersection and union operations for the smoothly joining of implicit objects (Ricci 1974). Middleditch is another pioneer on the study of implicit blending operations. In the paper of (Middleditch et al. 1985), he presents a technique for blending definition and profile control. Several implementations on 3D objects are visualised. Warren introduces a new definition of geometric continuity for implicit blending operations (Warren 1989). The blending of two or more polynomials always gives simple expression.

Hoffmann investigates and extends the potential method for implicit blending operations (Hoffmann 1993; Hoffmann et al. 1985). In order to avoid the pseudo-Euclidean distance of blending functions, Rockwood proposes the displacement blending which embeds the zero surface of the blending functions with a C^1 continuous algebraic distance.

Blinn uses implicit functions to draw algebraic surfaces and develops an algorithm that can be used for modelling electro density maps of molecular structures (Blinn 1982). The conception of blobby molecules (blobs) is proposed, where the implicit functions are the sum of radially symmetric functions with a Gaussian profile. Typically, a blob is an exponential function but can be replaced with piecewise polynomials to reduce the computational complexity (Blanc et al. 1995; Wyvill et al. 1986). Bloomenthal extends this idea and introduces convolution surfaces which gives fluid topological changes and smooth joints (Bloomenthal et al. 1991). The blob is also known as metaball (Nishimura 1985) or soft object (Wyvill et al. 1990).

Sederberg uses piecewise algebraic surfaces for geometric modelling. This method can blend algebraic surfaces together with any degree of smoothness. It can also be used for solid modelling (Sederberg 1985, 1987).

The implicit surfaces and their applications receive more attentions after 1990s. Muraki uses blobs for implicit modelling (Muraki 1991). A Blobby model is expressed as an isosurface of a scalar filed and different blobs can be blended together to form a very complicated shape.

Bloomenthal explains interactive techniques for implicit modelling (Bloomenthal et al. 1990a). In other papers, he discusses how to eliminate the bulges and creases when implicit surface blends together (Bloomenthal 1995a, 1997). Kacic-Alesic presents several techniques on the controlling of blended surfaces (Alesic et al. 1991). Pasko describes an implicit blending operation based on the modified R-function. The method supports both intuitive shape control and aesthetic blending by hand drawn strokes (Pasko et al. 1994; Pasko et al. 1995; Pasko et al. 2002b).

Desbrun presents a hybrid model for the animation of soft inelastic substance (Desbrun et al. 1995). Opalach overviews the modelling, rendering and animation of implicit surfaces in (Opalach et al. 1995) and presents the use of implicit surfaces for computer generated character animation in his dissertation (Opalach 1996).

In the course note of SIGGRAPH 1996, implicit surfaces are surveyed and compared with other modelling techniques (Menon et al. 1996). In the book of (Bloomenthal et al. 1997), Bloomenthal examines the definition, representation, and geometric properties of the implicit surface and its practical methods.

Implicit surfaces are used to design and animate complex deformable models by Cani-Gascuel (Cani-Gascuel et al. 1997). Implicit surfaces are introduced as extra layers coating any kind of structure that moves and deforms over time.

The implicit representation of a geometry is multi-isocontour with possible self-intersection and undesirable singularities. In order to overcome these problems, Bajaj presents the details of the implicit surface patches as several implicit algebraic surface splines (Bajaj 1997). Their use in C^1 and C^2 interpolation and interactive freeform modelling are also discussed.

Barthe combines implicit surfaces with soft blending operations in a Constructive Solid Geometry (CSG) tree to develop new shapes with limited number of parameters (Barthe et al. 1998).

Wyvill proposes the Blob Tree for arbitrary compositions of implicit surfaces. The rendering algorithms of implicit surfaces is also discussed (Wyvill et al. 1998). The Blob Tree is extended to be locally restricted in a later work (Groot et al. 2009).

Variational implicit surfaces are proposed for arbitrary manifold topology by Turk. A key strength of the variational implicit surfaces is both the location of points on the surface and surface normals can be directly specified (Turk et al. 1999, 2002).

Implicit surfaces and implicit blending operations are widely used on geometric modelling fields in the 21st century. Barthe presents a new implicit blending operator defined by an extruded implicit curve in an implicit extrusion field. This extrusion field is a 2D space that each blending coordinate is a potential field (Barthe et al. 2001). Museth presents a level set framework for the blending of implicit surfaces (Museth et al. 2002). Speed functions are defined as surface editing operators, which encapsulates all the information required to deform a surface. The proposed operators are regionally and globally supported for surface editing with quick computation. Barthe uses a freeform curve to define the blending regions of two implicit primitives (Barthe et al. 2004, 2003). The new blending operator unifies the sharp transitions and smooth transitions in a single formula such that general blending ideas are supported for freeform implicit modelling.

In (Zhao et al. 2001), the fast reconstruction of implicit surfaces based on variational and Partial Differential Equation (PDE) methods are used to reconstruct surface from scattered dataset. This is a pioneer work of level set surface reconstruction based on the proposal of level set methods and dynamic implicit surfaces (Osher et al. 2006).

SIGGRAPH 2003 presents the advances in implicit techniques in its course note. Variational implicit surfaces, radial basis functions and level set approaches are surveyed. The tools related to implicit modelling techniques and the fundamentals of implicit surfaces that make these tools work best are described (Yoo et al. 2003).

Multi-level Partition of Unity Implicits (MPUI) is a shape representation allows to construct surface models from very large point set (Ohtake et al. 2003b). This approach is flexible on local shape functions and can accurately represent sharp features with appropriate shape functions. The seperation of local approximation and local blending makes the representation can be rapidly evaluated.

Li proposes smooth unit step functions to define novel implicit blending operators (Li 2004, 2007; Li et al. 2008). The proposed operators can achieve any level of smoothness and the blending range is controllable. The shape of the blending result can be preserved to the original shapes as much as possible. Similarly, Hsu proposes two frameworks to transform exiting union and intersection blending operations to a new family that the blending range can be controlled (Hsu 2013); Zanni introduces an improved blending operator to give control over the topology changes (Zanni et al. 2015).

In order to describe sharp features of an implicitly defined surface, Song augments an implicit surface by adding edge descriptors and vertex descriptors which are defined by the distance field of edge curves such that the augmented function contains the sharp features (Song et al. 2009). This method has been used on the reconstruction of a point cloud with a sharp feature.

Bernhardt presents a new implicit blending solution that happens only at the overlapped region of two implicit objects but leaves a clean status for other parts of the objects (Bernhardt et al. 2010). Gourmel extends this idea to the gradient-based implicit blend, which uses not only the values of blended field functions but also their gradients (Gourmel et al. 2013). This method suppresses the bulge problems of constructive implicit modelling.

Effectively rendering of implicit surfaces is one of the difficulties of implicit modelling. This problem is detailedly discussed in Sigg's dissertation (Sigg 2006). This thesis proposes different ways of representing implicit functions with real-time performances. Level set method, signed distance function and quadratic surfaces are discussed in this thesis. A progressive rendering technique is proposed by Gamito which gives coarse-to-fine visualisation of implicit surface to overcome the slow procedure of ray casting method (Gamito et al. 2007).

Point Set Surface (PSS) is an important meshless surface representation. Guennebaud proposes a new PSS based on the Moving Least Squares (MLS) fitting of algebraic sphere (Guennebaud et al. 2007). This surface can be expressed by either a projection procedure or an implicit form. It is a very efficient computational representation of implicit surfaces. Poisson surface reconstruction creates watertight surfaces from oriented point sets. This method is robust for noisy point set scanned from real-world and gives fine details of the reconstruction implicit surfaces (Kazhdan et al. 2006). An extended work explicitly incorporates the points as interpolation constraints can be found at (Kazhdan et al. 2013).

The developing of implicit modelling requires more mathematical algorithms for better control of geometric shapes. Li proposes a new type of bivariate spline which can be created from any given set of 2D polygons with any required degree of smoothness. The basis function of this spline are piecewise polynomials such that the evaluation is fast and accurate (Li et al. 2009). When it is used as a parametric spline technique, this bivariate spline is partial shape-preserving implicit splines which can achieve the same effects of the classical Non-uniform Rational Basis Spline (NURBS) but with relatively smaller set of control points (Li et al. 2011). These new splines are powerful tools on implicit modelling of objects with complicated shapes. Based on the bivariate implicit splines, Hong develops a vascular reconstruction technique for the accurate construction of blood vessels. The qualitative and the quantitative validations show that this method is of high accuracy and smoothness (Hong et al. 2012).

Inspired by the dynamic implicit surfaces, Stam derives a time-evolving implicit surface based on velocity. This formulas have been applied on surface tracking and the motion blurred blobby surfaces. The normal component of the velocity is unknown in this method (Stam et al. 2011).

A short paper about tessellation of implicit surface with Cabor noise is presented by Zanni. This method blends implicit primitives without blurring the details (Zanni et al. 2012). Berger surveys a benchmark to evaluate and compare implicit surface modelling from point clouds. The pipeline of measuring a surface reconstruction algorithm is categorised into three phases: surface modelling, sampling and evaluation. The experiments in this paper demonstrate the state of surface reconstruction algorithms (Berger et al. 2013).

Rouhani presents a fast and flexible surface reconstruction techniques based on implicit B-spline with local support (Rouhani et al. 2015). This technique reconstruct a surface by solving a sparse system of equations. A novel weighting technique is introduced to smoothly blend implicit patches together. This method is efficient for handling large dataset with low computations.

Implicit modelling can also be used for stream modelling. In (Tao et al. 2016), Tao presents an interactive approach for the stream surface generation. A sketch-based interface is firstly designed to given topological clue of the streaming, and a 3D seeding curve is identified to generate a stream surface that captures the flow pattern. In the last, the streamlines are removed to give the final stream surface. This method gives an intuitive painting metaphor for many users.

One of the latest implicit geometric reconstruction techniques is proposed by Liu (Liu et al. 2017). This paper presents a surface reconstruction that involves the total variation of the implicit representation to minimize the occurrence of spurious sheets. This method can achieve high quality reconstruction results but reduce the use of extra sheets of the implicit modelling.

Implicit modelling has become a powerful tool on the surface and solid modelling of complicated geometries. There are three main advantages of implicit modelling (Bloomenthal 1990). Firstly, implicit model can be represented as either surface or solid by the same implicit function. Secondly, the inside and outside of the surface of an implicit model are directly determined by the implicit function. The most important property owned by implicit modelling is that implicit models can be easily combined together using certain blending (or composition) operations to form much more complicated object.

The slow development of implicit modelling before 1990s comes from the difficulty of effective representation of implicit geometric objects. The evaluation of an implicit function is much heavier than a parametric function (Bloomenthal 1990; Bloomenthal et al. 1990b). The problem has been progressively solved by fast development of powerful modern General-purpose Computing on Graphics Processing Units (GPGPU) with parallel computing (Araújo et al. 2015; Chen et al. 2014; Li et al. 2009; Owens et al. 2007). The main difficulty now is how to precisely design or reconstruct required shapes using implicit functions (Zanni et al. 2012).

2.4.2 Implicit Function

Implicit modelling technique uses implicit functions to express geometric shapes for surface modelling and solid modelling. An implicit function is in general a mapping $f : \mathbb{R}^m \to \mathbb{R}^n$. In terms of implicit modelling, the scale function $f : \mathbb{R}^3 \to \mathbb{R}$ is used to represent a 3D object. For example, a surface in the 3D space can be represented as the α-isosurface of an implicit function f:

$$\{\mathbf{X} \in \mathbb{R}^3 : f(\mathbf{X}) = \alpha\} \tag{2.1}$$

In contrast, an explicit function is a function in which the dependent variable can be written explicitly in terms of the independent variable. It is defined in the form of:

$$y = f(x_1, x_2, \ldots, x_n) \tag{2.2}$$

When the independent variables $(x_1, x_2, \ldots, x_n)$ are expressed with other parameters, u and v for example, this function is a parametric function.

The implicit function has several distinctive advantages over the explicit function. Firstly, an implicit function gives the position relation between a given point and an implicit object. For example, the sign of implicit function $f(\mathbf{X})$ at a given point $\mathbf{X}_0$ directly indicates whether this point is inside or outside, or on the implicit surface $f(\mathbf{X}) = 0$. Collision detection is therefore easier on implicitly represented objects.

Secondly, the function value at a given point directly provides the distance information from this point to the zero level set of the implicit function. In this way, two implicit function can be easily blended together to form a new implicit function. This is very important for modelling branching structures. For example, Figure 2.1 shows the scaler field of the min operation between implicit function $f(x,y) = 4x^2 + \frac{y^2}{4} - 1$ and $f(x,y) = \frac{x^2}{4} + 4y^2 - 1$. The 0-isocontour of the new implicit function is also shown.

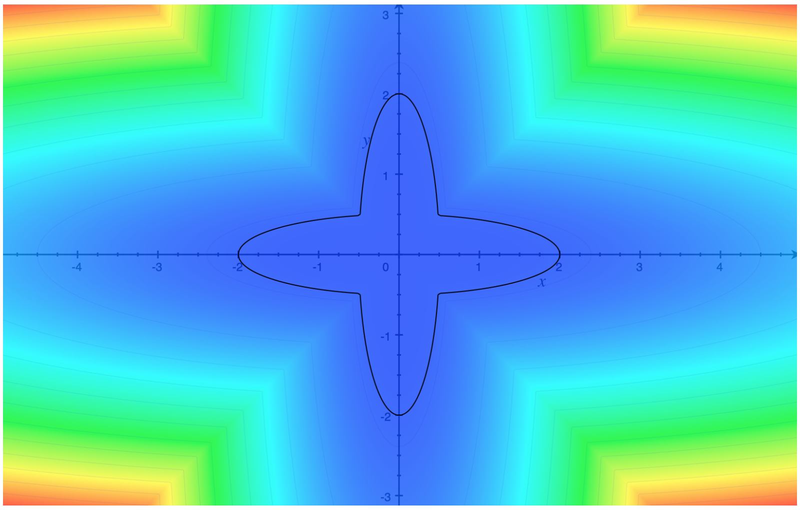

Figure 2.1: The Scalar Field of a 2D Implicit Function

Thirdly, implicit function has simple forms for spheres, cylinders, ellipsoids, cubes and many other common used geometries. For example, a unit sphere in 3D space can be implicitly represented as:

$$f(\mathbf{X}) = \|\mathbf{X}\| - 1 = 0, \mathbf{X} \in \mathbb{R}^3 \tag{2.3}$$

This representation is much simpler than the explicit and parametric counterparts of a unit sphere. Equation 2.4 gives an explicit unit sphere and Equation 2.5 shows a parametric representation.

$$z = \pm\sqrt{1 - x^2 - y^2} \tag{2.4}$$

$$\left\{\begin{array}{lcl} x & = & \sin\theta\cos\phi \\ y & = & \sin\theta\sin\phi \\ z & = & \cos\theta \end{array}\right. \tag{2.5}$$

The implicit function is a flexible mathematical tool for solid modelling. It has concise expression and is versatile on modelling freeform shapes. A complex implicit object can be assembled by simple implicit objects. This is an essential requirement for vascular modelling.

2.4.3 Special Implicit Functions

The Radial Basis Function (RBF) and the Signed Distance Function (SDF) are two special implicit functions. They are especially important for implicit modelling.

Radial Basis Function

The RBF is one of the simplest implicit functions. It is a real-valued function whose values depend only on the distance from the original point. The combination of RBFs is widely used on approximately given functions. In terms of geometric modelling, the RBF technique is an effective way to approximate the surfaces from unorganised points.

Buhmann surveys the development of RBF method and explains its usefulness (Buhmann 2000). The approximation of spheres and the computation of interpolants for large dataset are discussed. Carr uses the RBF method to reconstruct smooth and manifold surfaces from unorganised point data (Carr et al. 2001). The surfaces are implicitly defined as the zero level set of a RBF fitted to the given dataset. Very large datasets can be evaluated by a greedy algorithm which significantly compresses the number of RBF centres. Holes can be smoothly filled by this method.

Ohtake applies the coarse-to-fine hierarchy to the RBF method to reduce its sensitivity of points density (Ohtake et al. 2003a, 2004; Ohtake et al. 2005). A downsampling is firstly used to construct the hierarchy of the dataset, then the approximation is starting from the coarsest level with local supported basis function and progressively gains fine results. This method is faster than the globally supported RBF methods. An extension work based on the coarse-to-fine hierarchy is the sparse surface reconstruction with adaptive partition of unity and RBF (Ohtake et al. 2006). Ohtake combines the adaptive partition of unity approximation with the compactly supported RBF fitting and generates high-quality surface reconstruction.

Similarly, Tobor presents a multi-scale scheme for the reconstruction of implicit surfaces from discrete points (Tobor et al. 2006). Attributes are allocated in this scheme to give a better reconstruction results. The RBF techniques are used to reconstruct surface parts and these parts are hierarchically blended together with partition of unity functions.

Pan also presents a coarse-to-fine approach for the implicit surface reconstruction from scattered points (Pan et al. 2010). This method uses a two-level method on the reconstruction. The coarse level uses local quadratic approximation to compute the signed distances from the point set to the underlying surface, while the fine level performs a fitting to the residual errors on the surface points and additional off-surface points. The final result with a good approximation is the sum of these two intermediate functions.

The Dual-RBF is a novel implicit surface reconstruction approach. In the paper (Lin et al. 2009), Lin simulates the polar field model to initialise the Dual-RBF model and applies multi-level strategy to adjust the accuracy of the reconstruction. The Dual-RBF model becomes robust and shows faster modelling on surface reconstructions. The GPU acceleration is used on the visualisation of the surface.

A radial basis function consists of a linear combination of translated basis functions and the RBF approximation is essentially a problem of solving a linear system. In order to avoid the trivial solutions, extra layers of data points are constructed at the inside and outside of the original data points (Carr et al. 2001). A substitutional way is using direct RBF fitting. By using the ellipsoid constraints, Li proposes a direct RBF fitting method that approximates the data point with a one-step fitting. This method is especially suitable for small and sparse dataset (Li et al. 2004b).

As another solution of avoiding the use of extra offset points, Macedo presents the Hermite RBF implicits for the approximation of unstructured points with normals (Macêdo et al. 2009, 2010). By using Hermite data, which consists of the points and their normals, this method gives details of the reconstructed implicit surfaces and shows computing effectiveness when compared with other approaches.

The difficulty of solving a RBF interpolation grows rapidly with the increase of data size. In order to overcome this problem, Torres proposes a fast algorithm for RBF interpolation with Gaussians by means of localisation and iteration (Torres et al. 2009). This method uses Gaussians in small spreads to achieve localised solution of the global problem. This localisation happens during the solution procedure of the global basis functions. The global effect is then added back via interactions. The convergence can be obtained and the efficiency of the algorithm is excellent.

Another performance improving solution is using parallel computing. Yokata develops a parallel algorithm for RBF interpolation with $O(N)$ complexity and $O(N)$ storage. Gaussians with small variances are used in this method as the basis function instead of the use of maltiquadratic and polyharmonic basis functions. The accuracy of the this algorithm can achieve the matching precision (Yokota et al. 2010).

Ijiri proposes a contour-based volume image segmentation with the idea of implicit surface reconstruction (Ijiri et al. 2013). Hermite RBF interpolation is used to obtain the scalar filed of a joint spatial-range domain. This method produces segmentation boundary that passes through all contours, including both high-contrast image and blurred image. In another paper, Ijiri presents a novel 3D modelling technique for the real-world flowers extracted from CT images (Ijiri et al. 2014). A new active contour model is designed for the flower CT to fit and reconstruct the shaft and sheet of a flower respectively. This is a semi-automatic modelling technique.

Liu proposes a closed-form formulation of surface reconstruction based on the Hermite RBF (Liu et al. 2016). The quasi-solution is used to approximate the surface such that no global operations are required on the generation of the implicit functions. This method is robust and efficient for the reconstruction of real-world objects.

The surface reconstruction using RBF is still a popular research topic at present. For example, Cuomo (Cuomo et al. 2017) focuses on the theoretical and practical issues of using RBF for the surface reconstruction from unorganised points, Crivellaro proposes an algorithm for adaptive multilevel interpolation based on the RBF for surface reconstruction (Crivellaro et al. 2017), and DeRossi discusses the construction of RBF-based Partition of Unity interpolants (De Rossi et al. 2017).

More details of the radial basis function will be discussed in Chapter 3.

Signed Distance Function

In 3D spaces, an isocontour of an implicit function represents a surface. The distance between two isocontours is usually unknown since the gradient value of the implicit function may not be a constant. In contrast, the Signed Distance Function (SDF) can hold this distance such that the shape of the geometry represented as a SDF is easier to control. However, finding the distance from a point to a curve or surface is in general computationally impractical, the SDF should be approximated in other ways.

Taubin is one of the pioneers on the approximation of distance functions. He proposes the simple approximate distance with first order to efficiently carry out the estimation of the distance from a point set without using the nonlinear optimisation techniques (Taubin 1988). In another paper, Taubin demonstrates that the minimisation process can be reduced to a problem of generalised eigenvector fiting in certain cases and can be computed in real time (Taubin 1991). However, the approximate distance shows limitation on certain families of implicit curves and surfaces such as circles, planes, spheres and cylinders. Taubin introduces an improved approximation distance to evaluate the distance from a point to a curve or surface. The iterative procedures are not required either but the results are with the same quality as those based on the exact distance (Taubin 1993).

The calculation of the distance between a point to a geometric object attracts the attentions of other researchers. Barbier presents the algorithms for the distance between a point to specific geometries, including cylinder, cone, line-swept sphere and cone-sphere. Some acceleration algorithms relating to distance estimation are also developed (Barbier et al. 2004). Tankelevich presents a new geometric modelling technique based on level sets and distance fields, which has the advantage of smooth converging to threshold surfaces (Tankelevich et al. 2004).

Zeng presents a PDE-driven method to reconstruct the 3D objects from point cloud. A shape is represented as an SDF and a PDE is directly applied onto the point cloud with the SDF as the constraint. With this method, a deformable surface can shrink to the surface of the object (Zeng et al. 2005).

In order to model and analyse physical fields within a geometric object, Freytag uses approximate distance fields on geometric data (Freytag et al. 2006). The use of approximate distance avoids the difficulties on mesh-based reconstructions. The distances are used to model fields satisfying boundary conditions with arbitrary precision. The heat transfer applications are used to demonstrate the modelling capability of this method.

Rouhani presents a distance estimation for the fitting of implicit polynomials (Rouhani et al. 2012). The height of a simplex is used to estimate the real orthogonal distance and the proposed distance can be treated as a coefficient of the implicit polynomial. The distance is differentiable such that any gradient-based optimisation can use this distance.

In order to better represented the blended soft objects more diverse, Hsu proposes the morphological operations of distance function to deform a primitive soft object (Hsu et al. 2015). More than two morphological operations can be applied onto a soft object to deform it with more flexibility.

More details of the signed distance function will be discussed in Chapter 4.

2.4.4 Implicit Object

The geometry represented by implicit functions is an implicit object. Mathematically, a 3D implicit object is represented as a scalar field function $f : \mathbb{R}^3 \to \mathbb{R}$ (Velho et al. 2007). An implicit object can be either a solid or a surface.

Definition 2.1 (Implicit Object)**.** Let $\mathbb{U} \subset \mathbb{R}^3, \mathbb{V} \subset \mathbb{R}$, and let $f : \mathbb{U} \to \mathbb{R}$ be an implicit function. An *Implicit Object* $\mathcal{O}$ is a subset of $\mathbb{U}$, such that $\mathcal{O} = \{\mathbf{X} \in \mathbb{U} : f(\mathbf{X}) \in \mathbb{V}\}$.

The level set $\partial\Omega_\alpha = \{\mathbf{X} \in \mathbb{U} : f_\alpha(\mathbf{X}) = \alpha\}$ is a surface dividing space $\mathbb{U}$ into two parts: the interior region $\Omega_\alpha^- = \{\mathbf{X} \in \mathbb{U} : f_\alpha(\mathbf{X}) < \alpha\}$ and the exterior region $\Omega_\alpha^+ = \{\mathbf{X} \in \mathbb{U} : f_\alpha(\mathbf{X}) > \alpha\}$.

Particularly, the 0 level set $Z(f) = \partial\Omega_0$ is the *implicit surface* of $\mathcal{O}$, $\partial\Omega_0 \cup \Omega_0^- = \{\mathbf{X} \in \mathbb{U} : f(\mathbf{X}) \leqslant 0\}$ is the *interior implicit solid* of $\mathcal{O}$, and $\partial\Omega_0 \cup \Omega_0^+ = \{\mathbf{X} \in \mathbb{U} : f(\mathbf{X}) \geqslant 0\}$ is the *exterior implicit solid* of $\mathcal{O}$.

Figure 2.6 demonstrates the interior implicit solid (Figure 2.2(a)), exterior implicit solid (Figure 2.2(b)) and implicit surface (Figure 2.2(c)) in a 2D condition. The implicit function $f(x, y) = \min(4x^2 + \frac{y^2}{4} - 1, \frac{x^2}{4} + 4y^2 - 1)$ is represented as three implicit objects by $f(x, y) < 0$, $f(x, y) > 0$ and $f(x, y) = 0$ respectively. The objects are rendered with blue colour.

A 3D implicit object is usually represented as a surface-based object. For one thing, the solid modelling normally focuses on the geometric shape of a 3D object without the attention on its interior structures. The internal part of the object is usually regarded as a solid with evenly distributed materials. For another, a 3D implicit modelling task usually expresses a modelling result as a closed geometric shape. The modelling result can be regarded as an interior implicit solid $\partial\Omega_0 \cup \Omega_0^-$ enclosed by the implicit surface $\partial\Omega_0$. In many applications, it is more convenient to consider it as a surface object for the purpose of geometric analysis. What is more, geometric modelling on real-world 3D object uses the data points collected from the surface of the object and reconstructs these points to be a geometric surface. It is reasonable to use a surface-based object as the representation of the real-world object.

Two examples of the surface-based object are shown in Figure 2.3. The object in Figure 2.3(a) is the surface of the implicit solid $f(x, y, z) = \max(\min(\frac{1}{4}x^2 + 4y^2 + z^2 - 1, 4x^2 + \frac{1}{4}y^2 + z^2 - 1), z) \leqslant 0$. The object in Figure 2.3(b) is the Clebsch Cubic Surface. It is the 0 level set of Equation 2.6.

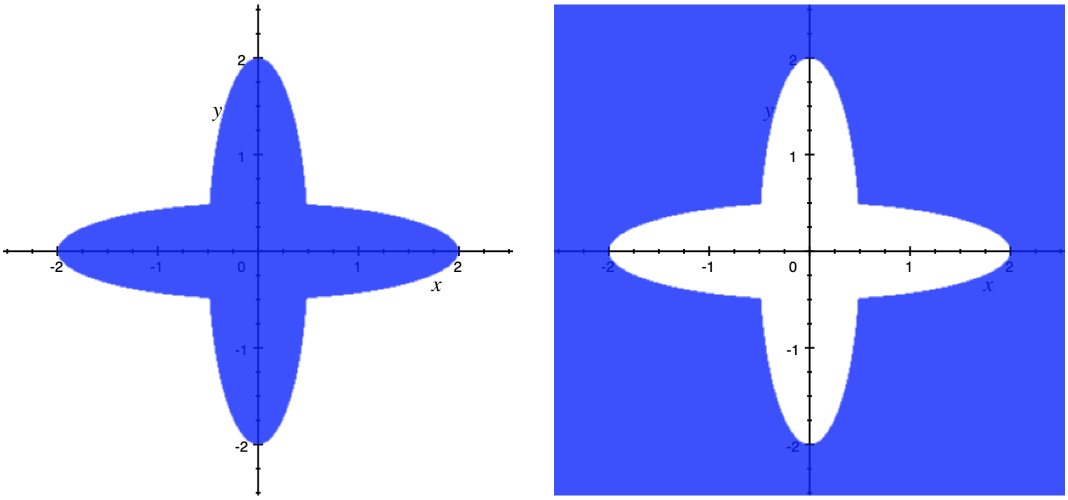

(a) $\Omega_0^- = \{\mathbf{X} : f(\mathbf{X}) < 0\}$ (b) $\Omega_0^+ = \{\mathbf{X} : f(\mathbf{X}) > 0\}$

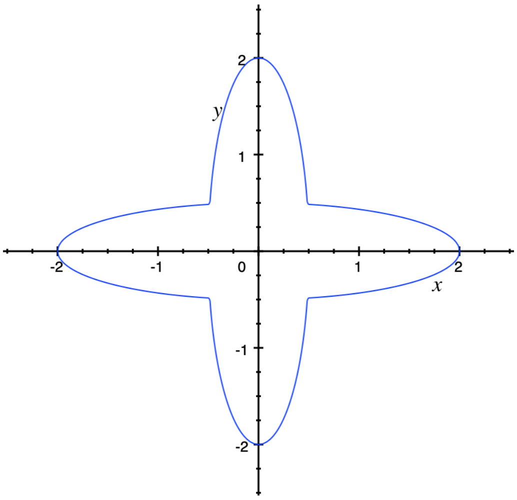

(c) $\partial\Omega_0 = \{\mathbf{X} : f(\mathbf{X}) = 0\}$

Figure 2.2: 2D Implicit Objects

$$\begin{aligned} f(x,y,z) \quad = \quad & 81(x^3+y^3+z^3) \\ & -189(x^2y+x^2z+y^2x+y^2z+z^2x+z^2y) \\ & +54xyz+126(xy+xz+yz) \\ & -9(x^2+y^2+z^2)-9(x+y+z)+1 \end{aligned} \tag{2.6}$$

The geometry of a surface-based object can either be designed by mathematical approaches or reconstructed from real-world object. For the latter one, unorganised points are usually sampled from the surface of the real-world object and these points will be approximated into a geometric surface (Berger et al. 2016; Berger et al. 2014; Hoppe 1994). In terms of implicit modelling, this approximation is called implicit surface reconstruction.

Definition 2.2 (Implicit Surface Reconstruction). *Implicit Surface Modelling* is to find an implicit function $f : \mathbb{R}^3 \rightarrow \mathbb{R}$ such that $\sum_{i=1}^{n} d(\mathbf{P}_i, Z(f)) = 0$, where

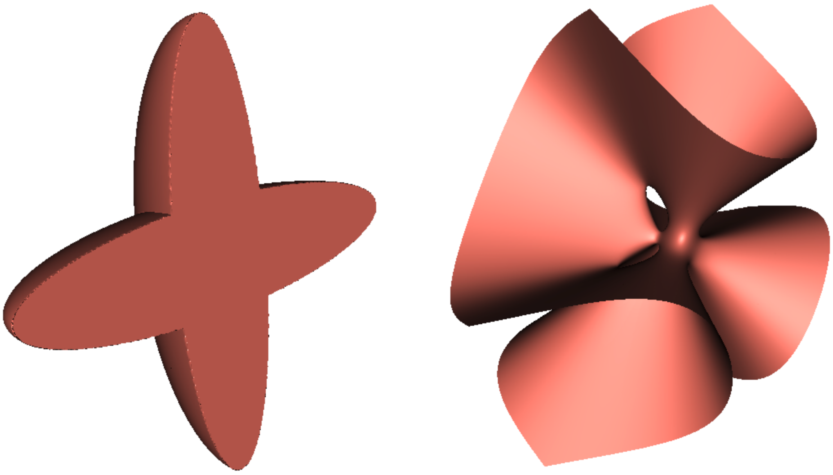
(a) A 3D Implicit Solid (b) Clebsch Cubic Surface

Figure 2.3: 3D Implicit Objects

$\{\mathbf{P}_1, \mathbf{P}_2, \ldots, \mathbf{P}_n\}$ are n distinct points sampled from a given surface $\mathcal{S} \subset \mathbb{R}^3$, $Z(f) = \{\mathbf{X} \in \mathbb{R}^3 : f(\mathbf{X}) = 0\}$ is the 0 level set of f, $d(\mathbf{P}_i, Z(f)) = \min_{\mathbf{P} \in Z(f)}(\|\mathbf{P}_i - \mathbf{P}\|)$ is the Euclidean distance from point $\mathbf{P}_i$ to the surface $Z(f)$.

Implicit surface reconstruction has been widely used on the reconstruction of complicated objects, especially soft tissues hidden inside medical images. Representative implicit surface modelling methods are level set method (Zhao et al. 2001), Moving Least Squares (MLS) method (Guennebaud et al. 2007; Klein et al. 2004), variational implicit surface method (Turk et al. 1999), adaptively sampled distance field method, Multi-level Partition of Unity Implicits (MPUI) method (Frisken et al. 2000), Radial Basis Function (RBF) method (Li et al. 2004b; Macêdo et al. 2010; Wu 1992) and other methods (Pan et al. 2016, 2017; Wu et al. 2015).

2.4.5 Blending Operation

A distinctive geometric property of implicit objects is they can be combined to form new shapes using binary blending operator (composition operator).

Definition 2.3 (Implicit Blending Operator)**.** Let $f_0 : \mathbb{R}^n \to \mathbb{R}$ and $f_1 : \mathbb{R}^n \to \mathbb{R}$ be two implicit functions, $n = \{2, 3\}$. An *Implicit Blending Operator* is a mapping $g : \mathbb{R}^2 \to \mathbb{R}$ such that $g = g(f_0, f_1)$ is a composite function.

An effective method to build blending operators is using Constructive Solid Geometry (CSG) operations. Let $\mathcal{O}_0 = \{\mathbf{X} \in \mathbb{R}^3 : f_0(\mathbf{X}) \leqslant 0\}$ and $\mathcal{O}_1 = \{\mathbf{X} \in \mathbb{R}^3 : f_1(\mathbf{X}) \leqslant 0\}$ be two implicit objects represented by field functions $f_0 : \mathbb{R}^3 \to \mathbb{R}$ and

$f_1 : \mathbb{R}^3 \rightarrow \mathbb{R}$. The implicit objects corresponding to the intersection $\mathcal{O}_0 \cap \mathcal{O}_1$, union $\mathcal{O}_0 \cup \mathcal{O}_1$ and subtraction $\mathcal{O}_0 \backslash \mathcal{O}_1$ of $\mathcal{O}_0$ and $\mathcal{O}_1$ can be defined using the maximum function $g = \max(f_0, f_1)$, a special and the simplest intersection blending operator, in the following way:

$$\left\{\begin{array}{rcc} \mathcal{O}_0 \cap \mathcal{O}_1 & = & \{\mathbf{X} \in \mathbb{R}^3 : g(f_0(\mathbf{X}), f_1(\mathbf{X})) \leqslant 0\} \\ \mathcal{O}_0 \cup \mathcal{O}_1 & = & \{\mathbf{X} \in \mathbb{R}^3 : -g(-f_0(\mathbf{X}), -f_1(\mathbf{X})) \leqslant 0\} \\ \mathcal{O}_0 \backslash \mathcal{O}_1 & = & \{\mathbf{X} \in \mathbb{R}^3 : g(f_0(\mathbf{X}), -f_1(\mathbf{X})) \leqslant 0\} \end{array}\right. \tag{2.7}$$

For a general blending operation $g(x, y)$, the blending operators $g_\cap, g_\cup$ and $g_\backslash$ corresponding to the intersection, union and subtraction of two implicitly represented geometric shapes with function f_0 and f_1 are defined in the following way:

$$\left\{\begin{array}{rrcl} \text{intersection:} & g_\cap(f_0, f_1) & = & g(f_0, f_1) \\ \text{union:} & g_\cup(f_0, f_1) & = & -g(-f_0, -f_1) \\ \text{subtraction:} & g_\backslash(f_0, f_1) & = & g(f_0, -f_1) \end{array}\right. \tag{2.8}$$

In solid modelling, $g_\cap(f_0, f_1)$ and $g_\cup(f_0, f_1)$ are often defined as $g_\cap(f_0, f_1) = \max(f_0, f_1)$ and $g_\cup(f_0, f_1) = \min(f_0, f_1)$ (Ricci 1974). The min blending has been demonstrated in Figure 2.2. Although these two blending operators are simple, max and min are not generally differentiable and not suitable for modelling smooth solid geometric objects.

Various soft max and min functions are proposed to blend implicit objects smoothly. For instance, a soft max function can be defined as $g(f_0, f_1) = \frac{1}{k}\ln(e^{kf_0} + e^{kf_1})$ using a hardness control factor $k > 0$. Let $g_\cap = g$, then $g_\cup$ and $g_\backslash$ can be given with Equation 2.8. Although the soft blending functions defined in this way have a high degree of continuity, they lack blending span controllability. When an implicit object is blended with other objects using these blending operations, its entire shape will be distorted with no part of its original shape being kept unchanged.

Another soft blending operator is the R-function, whose sign is completely determined by the sign of its arguments (Rvachev 1963; Shapiro 1991, 1994). The most popular R-function is $R_\alpha = \frac{1}{1+\alpha}(f_0 + f_1 + \sqrt{f_0^2 + f_1^2 - 2\alpha f_0 f_1})$, where $\alpha = \alpha(f_0, f_1)$ is a symmetric function and $\alpha \in (-1, 1]$. Let $g_\cap = R_\alpha$, $g_\cap$ and $g_\backslash$ can then be constructed with Equation 2.8.

When $\alpha = 0$, intersection function $g_\cap$ is reduced to simplified R-function $g_\cap(f_0, f_1) = f_0 + f_1 + \sqrt{f_0^2 + f_1^2}$ (Pasko et al. 1995). When $\alpha = 1$, it is reduced to a max function $g_\cap(f_0, f_1) = \frac{1}{2}(f_0 + f_1 + |f_0 - f_1|) = \max(f_0, f_1)$ (Ricci 1974). Simplified R-function is C^1 continuous piecewise bivariate polynomial and can be extended to C^m continuous in the form of $g_\cap(f_0, f_1) = (f_0 + f_1 + \sqrt{f_0^2 + f_1^2})(f_0^2 + f_1^2)^{\frac{m}{2}}$ (Pasko et al. 1995). Function max is C^0 continuous and can be extended to a C^n-smooth piecewise polynomial $\max_{n,\delta}$ function (Li 2007).

Smooth piecewise polynomial $\max_{n,\delta}$ function is a C^n-smooth max function ($n > 0$) with a smoothness span controller $\delta > 0$ developed in (ibid.):

$$\max_{n,\delta}(x, y) \;=\; \tfrac{1}{2}(x + y + |x - y|_{n,\delta}) \tag{2.9}$$

where

$$|x|_{n,\delta} = \begin{cases} |x| & \text{for} \quad n = 0 \\ \frac{\delta}{n}\left|\frac{nx}{\delta}\right|_n & \text{for} \quad n = 1, 2, 3, \ldots \end{cases} \tag{2.10}$$

and

$$|x|_n = \begin{cases} |x| & \text{for} \quad n = 0 \\ \frac{1}{2(n+1)}[(n - x)\,|1 - x|_{n-1} & \\ \quad +(n + x)\,|1 + x|_{n-1}] & \text{for} \quad n = 1, 2, 3, \ldots \end{cases} \tag{2.11}$$

With $\max_{n,\delta}$, a set of C^n-smooth shape-preserving blending operators $g_{\cap_{n,\delta}}, g_{\cup_{n,\delta}}$ and $g_{\setminus_{n,\delta}}$ can be constructed in the following way (ibid.):

$$\begin{cases} g_{\cap_{n,\delta}}(f_0, f_1) &= \max_{n,\delta}(f_0, f_1) \\ g_{\cup_{n,\delta}}(f_0, f_1) &= -g_{\cap_{n,\delta}}(-f_0, -f_1) \\ g_{\setminus_{n,\delta}}(f_0, f_1) &= g_{\cap_{n,\delta}}(f_0, -f_1) \end{cases} \tag{2.12}$$

where $\delta > 0, n = 0, 1, 2, \ldots$.

Both sharp and smooth joints can be produced from shape-preserving blending operators. With additional smoothness span controller $\delta > 0$, they are ideal choices for composition of implicit functions.

Figure 2.4 presents the intersection blending between implicit functions $f_0(x, y) = y - \sin(0.5x)$ and $f_1(x, y) = y - \cos(6x)$. Figure 2.4(a) shows the blending result with R_α function. $g_\cap$ is reduced to a max function when $\alpha = 1$. Sharp blending can be observed when the curves of the two functions joint. Figure 2.4(b) presents blending result using the soft max function. When $k = 10$, blending span is smaller than $k = 3$ and the shape of blending is preserved better also. In general, the larger the value of k, the better the blending result preserves the shape.

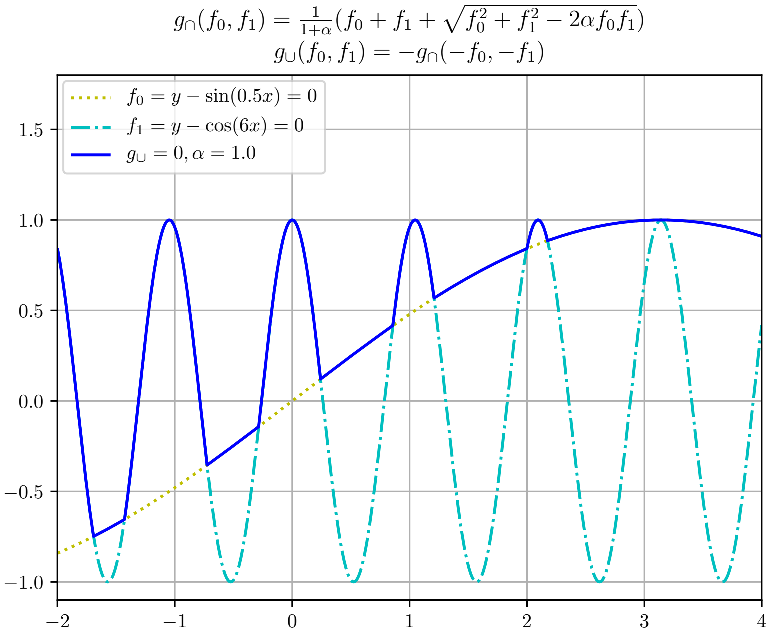

(a) R-Function as max function, $\alpha = 1$

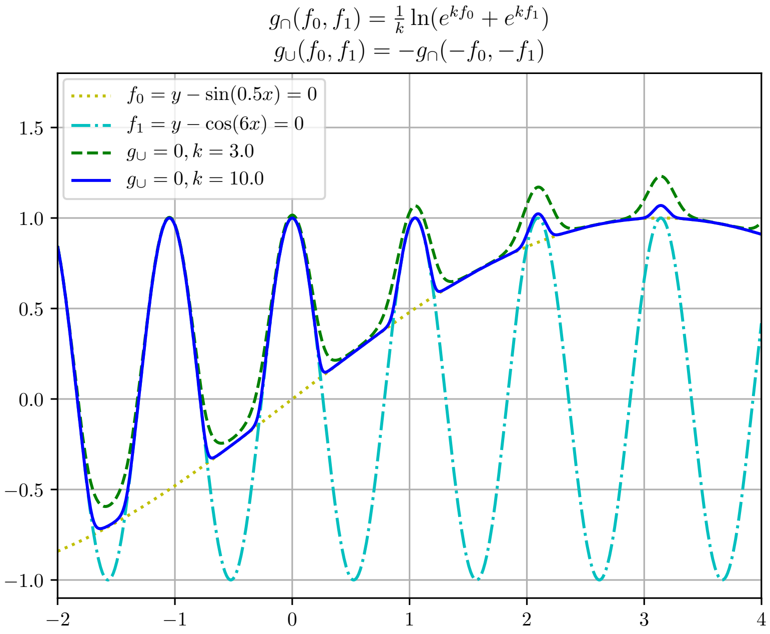

(b) Soft max Function

Figure 2.4: Implicit Intersection Blending

Figure 2.5 presents the intersection blending between implicit functions $f_0(x, y) = y - \sin(0.5x)$ and $f_1(x, y) = y - \cos(6x)$ using the shape-preserving blending operation. Both the two blending results are C^2 continuous, but smaller δ value gives narrower smoothness span and better preserves the original shapes of f_0 and f_1. The bulge at $x = \pi$ is also smaller.

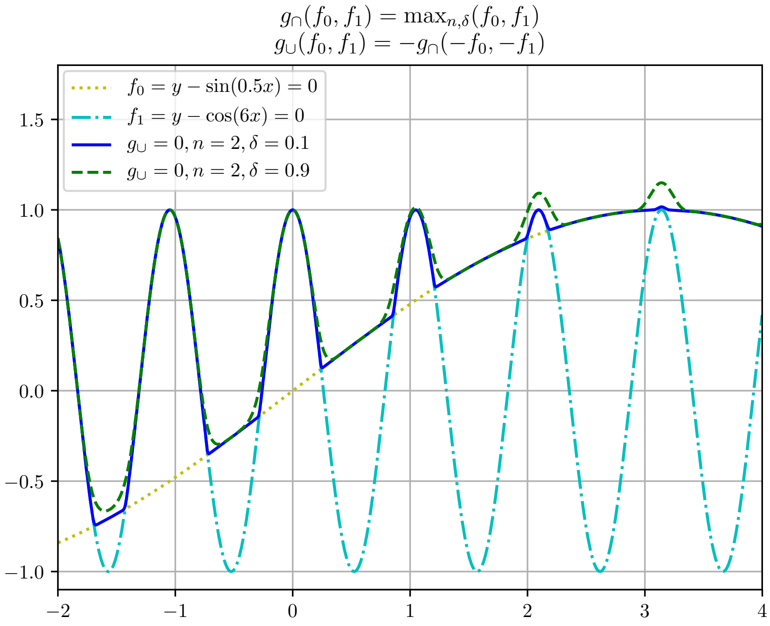

Figure 2.5: Shape-preserving Blending

Figure 2.6 presents an implicit geometry designed by the 0 level set of the implicit function

$$f(x, y, z) = g_{\cup_{2,0.5}}(g_\cap(g_\setminus(x - 0.2, x + 0.2), g_\setminus(y - 0.2, y + 0.2)), z) \tag{2.13}$$

where $g_\setminus$ and $g_\cap$ are sharp blending subtraction and intersection operators, $g_{\cup_{2,0.5}}$ is the C^2-smoothness shape-preserving union blending operator with smoothness span controller 0.5.

In addition to the CSG operations, blending operators can also be defined in other ways, such as linear blend (Bloomenthal 1997), hyperbolic blend (Kleck 1989), super-elliptic blend (Rockwood 1989) and convolution blend (Bloomenthal et al. 1991; Sherstyuk 1999). More literatures about implicit blending can be found at (Angles et al. 2017; Barthe et al. 1998; Barthe et al. 2003; Bernhardt et al. 2010; Gourmel et al. 2013; Groot et al. 2009; Hoffmann et al. 1985; Pasko et al. 1994; Pasko et al. 1995; Sabin 1968; Wyvill et al. 1998; Zanni et al. 2015).

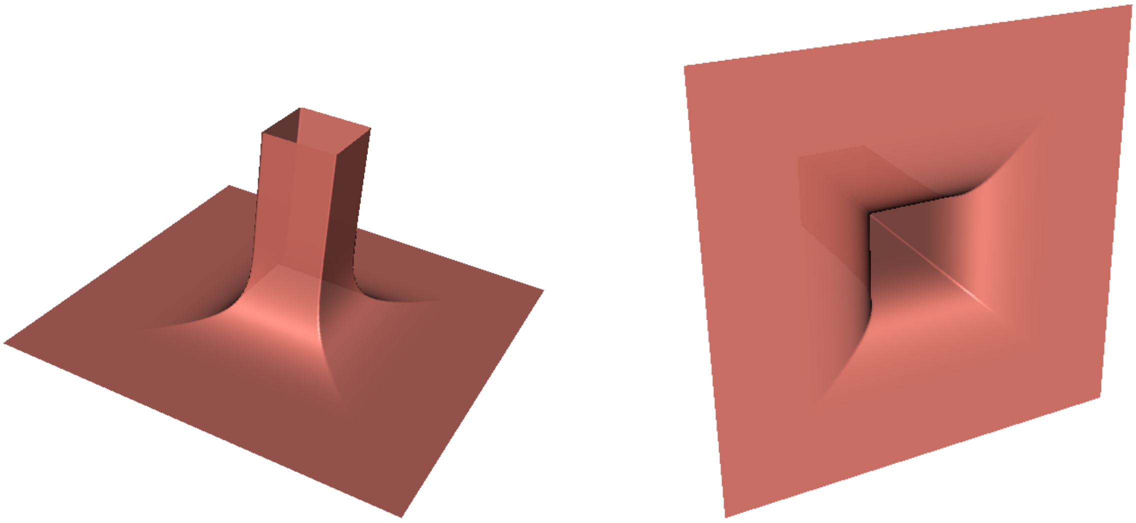

(a) (b)

Figure 2.6: A Blending between a Square Column and a Plane

2.5 Visualisation Techniques

In order to visually present the internal details of a volumetric image, the medical image and the modelling results are required to be rendered by visualisation techniques (Preim et al. 2008). A medical image is usually rendered as a volumetric object and the modelling results are usually rendered as a surface object.

2.5.1 Volume Rendering

A medical image dataset is a large 3D matrix or a group of 2D matrices generated with imaging techniques. In order to rebuild the structure of a Volume of Interest (VOI), it is helpful to visualise the dataset and interactively reconstruct organs or tissues in the VOI. Volume rendering is a visualisation technique for this purpose (Kaufman et al. 2005; Pommert et al. 1992).

The volume rendering can be generally categorised as direct volume rendering and indirect volume rendering (Ruikar et al. 2018). Direct volume rendering technique directly renders 2D projections of the volume from the discrete image dataset. All the data of the image can be observed simultaneously. Parallel computing is usually used to accelerate this rendering. In contrast, indirect volume rendering uses slices, textures or isosurfaces to simulate the volume. Indirect rendering is less commonly used although it is computational cheaper than direct rendering.

Direct volume rendering uses transfer functions to represent a voxel of the medical image with specific values, such as material value, colour value and opacity value. A transfer function is a Lookup Table (LUT) designed to accentuate important features and minimise less important or extraneous details of a huge dataset. Artefacts may be generated from different colour choices and data interactions.

There are mainly three transfer functions of volume rendering: colour transfer function, opacity transfer function and gradient opacity function. Colour transfer function is used to identify different tissues out of the image. It is modality-specific and anatomy-specific. For example, skin and bone have different intensity values and can be distinguished. Opacity transfer function controls the opacity of different tissue types such that the interior part of the image can be visualised. Gradient opacity function is used to adjust the opacity value of the image. The regions with low gradient values are decreased to highlight the boundaries between tissue types. The image is enhanced in this way for better identification of tissues (Levoy 1988).

2.5.2 Surface Rendering

A medical image can be evaluated as a discrete field function. Carefully selected isosurfaces extracted from this field correspond to different tissue types. The rendering of these isosurfaces is another visualisation technique of implicit modelling.

For the image-based modelling, an isosurface is a level set of the image. The voxels on this isosurface share a constant value to represent a specific tissue. An isosurface can either be directly extracted from the image volume or be generated with geometric modelling techniques. It is a surface existed inside the image volume space and can be rendered much faster than the rendering of the whole volume.

The most common used visualisation of surface rendering techniques are polygonisation and ray tracing. Polygonisation describes subdivision of a surface into polygons. It is a standard surface rendering method and has gained wide hardware support. A surface can be polygonised either as triangles or polygons. Normals of points and triangles are usually calculated during the polygonisation for better mesh description (Bloomenthal 1988). Ray tracing determines the visibility of surfaces by tracing imaginary rays of light from the viewer's eye to the object in the scene (Foley 1996). It involves creating a ray and tracing its path as it reflects or refracts through the scene. One can determine what light might arrive at its source from the other direction. Ray tracing is capable of generating high realistic rendering results but is also computational heavier (Wald et al. 2001).

2.6 Summary

The image-based vascular modelling is an interdisciplinary research filed. The complex structures of the vascular trees, the various shapes of the blood vessels and the flexible joints of the connections make the modelling task extremely hard. This chapter reviewed the vascular modelling techniques from several aspects on vascular skeleton, templates and segmentation of vascular images, and implicit modelling techniques for the following reasons:

- A single blood vessel is with simple shape and structure that both explicit modelling and implicit modelling are available techniques. However, a vascular tree consists of various blood vessels, each of which has its own unique geometry and property. What is more, considering the complex connections of these blood vessels, the explicit modelling shows impracticability on the modelling task. Although the implicit modelling is less controllable on the geometric shapes than the explicit counterpart, the convenient blending operations suit the vascular modelling very much.
- The basic geometric character of a blood vessel is its long thin shape. It is straightforward to consider a blood vessel as a curve represented as its skeleton or centreline and move a surface or a solid on the curve to get the structure of the vessel. Although a blood vessel can be directly reconstructed without the assistance of the skeleton, most of the existing vascular modelling techniques, the sweep surface method for instance, use skeleton-based approaches. Skeletonisation has been an independent research field on vascular modelling and the skeletons improve the accuracy of the modelling task.
- The shape of a blood vessel is a generalised cylinder and this cylinder can be roughly regarded as a truncated cone or a combination of several cones. This idea is the model-based vascular modelling. Although this method produces nice visualised blood vessels, the geometry of the vessel is too ideal to fit the real-world object. In most cases, the model-based vascular modelling is used for the analysis of hemodynamic or educational purpose.
- The avoid of using model-based method leads to the segmentation-based vascular modelling. Image segmentation is widely researched in image analysis and processing. The segmented vascular image extracts the vascular data points out of the background and other tissues of the medical image. These data points are usually fitted into surfaces or solids using specific methods. The segmentation-based vascular modelling reconstructs the geometry of the blood

vessel more faithfully than the model-based method. It closely cooperates with the blood vessel skeleton on modern vascular modelling techniques.

- Besides these aspects, the vascular modelling also shows diversity on the modelling scopes. A global modelling treat the vascular tree as a single modelling object without caring the shape differences between large blood vessels and the small ones or the disagreements of the intensive image parts and the weak regions (Liang et al. 2013). In contrast, a local modelling focuses on a local region of the whole image space in order for high-quality vascular modelling of the specific region. This localised strategy may require the assistance of the implicit modelling technique to blend localised modelling results together. It is often used by the high-accuracy vascular modelling techniques.
- The implicit function is the mathematical fundamental of implicit modelling technique. The implicit objects are the geometric objects represented with implicit functions. The blending operation plays the core work of implicit modelling, which combines different implicit objects together without complex computation. The visualisation technique renders the modelling result on the screen for interaction and better observation of the implicit objects.

Geometric vascular modelling is a popular research area on the reconstruction of human bodies. Most of the existing approaches reviewed in this chapter use skeleton and segmentation for the accurate geometric vascular modelling tasks. Although some of these approaches give good reconstruction results, there are lots of spaces to improve the modelling performance. For example, the sweep surface achieves satisfactory modelling results in some applications (Hong et al. 2012; Kretschmer et al. 2013), but this method is a two-step appoach requiring extra operations and the reconstruction accuracy cannot be guaranteed out of the cross-sections of the sweep surface. Not only the unnecessary computations should be avoided but also the modelling performance and accuracy could be improved.

Chapter 3

Skeleton Marching-based Vascular Reconstruction

3.1 Introduction

Reconstruction of blood vessels is to rebuild the geometric structures of blood vessel wall out of medical images. As discussed in previous chapters, this reconstruction can be mathematically categorised into explicit modelling and implicit modelling (Preim et al. 2008). Implicit modelling is the favoured method for its flexibility on implicit blending operations. This research uses implicit modelling technique for vascular reconstruction.

Vascular modelling aims at reconstructing the geometric structures of blood vessel wall extracted from segmentation result of vascular medical images. A blood vessel is in the shape of a thin tubular structure and is often represented as a centreline or skeleton of the tube. The skeleton of a blood vessel is an important geometric clue on vascular modelling. It has been widely discussed whether skeleton-based or skeleton-free modelling technique satisfy the requirement of vascular modelling (Hong et al. 2012; Kretschmer et al. 2013; Wu et al. 2011). In general, skeleton-free modellings, such as marching cube (Lorensen et al. 1987) and Multi-level Partition of Unity Implicits (MPUI) (Ohtake et al. 2003b), are prone to generate surfaces with poor quality and therefore additional smoothing operations are required. Yet the skeleton-based method is more straightforward and applicable for vascular modelling, since the skeleton is an immanent geometric property of tubular structures.

The sweep surface method is an intuitionistic way of skeleton-based vascular modelling technique. It generates a series of cross-sections along the skeleton by sweeping a surface and approximates these cross-sections to be a generalised cylinder. This is a two-step approximation modelling method. A cross-section is approximated as a spline, and a set of splines is approximated to be a generalised cylinder.

Inspired by sweep surface method, this chapter proposes the Skeleton Marching technique to produce high-performance computation and high-accuracy vascular tree using localised implicit geometric objects. Instead of using sweep surface, a marching implicit solid is used to sweep the blood vessel along the skeleton, which not only avoids the two-step approximation of sweep surface, but also improves the modelling performances.

3.2 Skeleton Marching

Skeleton marching is an implicit modelling technique for the geometric reconstruction of blood vessels. The skeleton of a blood vessel is first represented as a spline curve. This spline curve is then divided into several overlapped shorter segments, which assist a localised image segmentation technique to extract point clouds corresponding these segments. These small point clouds are then fitted and blended into a whole blood vessel represented as an implicit surface. All the locally reconstructed implicit blood vessels are then blended to represent the geometry of the whole vascular system.

Reconstructing a vascular tree with skeleton marching technique is similar to exploring a cave with multiple branching structures by following the cave skeleton, and thus can be directly implemented in a parallel manner, as each branch and each vascular segment can be reconstructed independently of other branches or vascular segments. The skeleton marching technique consists of subdivision of skeleton, localised implicit reconstruction, localised implicit object and parallel computing. Figure 3.1 illustrates the process of skeleton marching technique.

3.2.1 Subdivision of Skeleton

The basic idea of skeleton marching is localisation, which not only simplifies the modelling complexity but also accelerates the modelling speed. A vascular image contains highly complicated blood vessels together with large amount of non-vascular information. Due to the high complexity of the vascular structure, it is in general

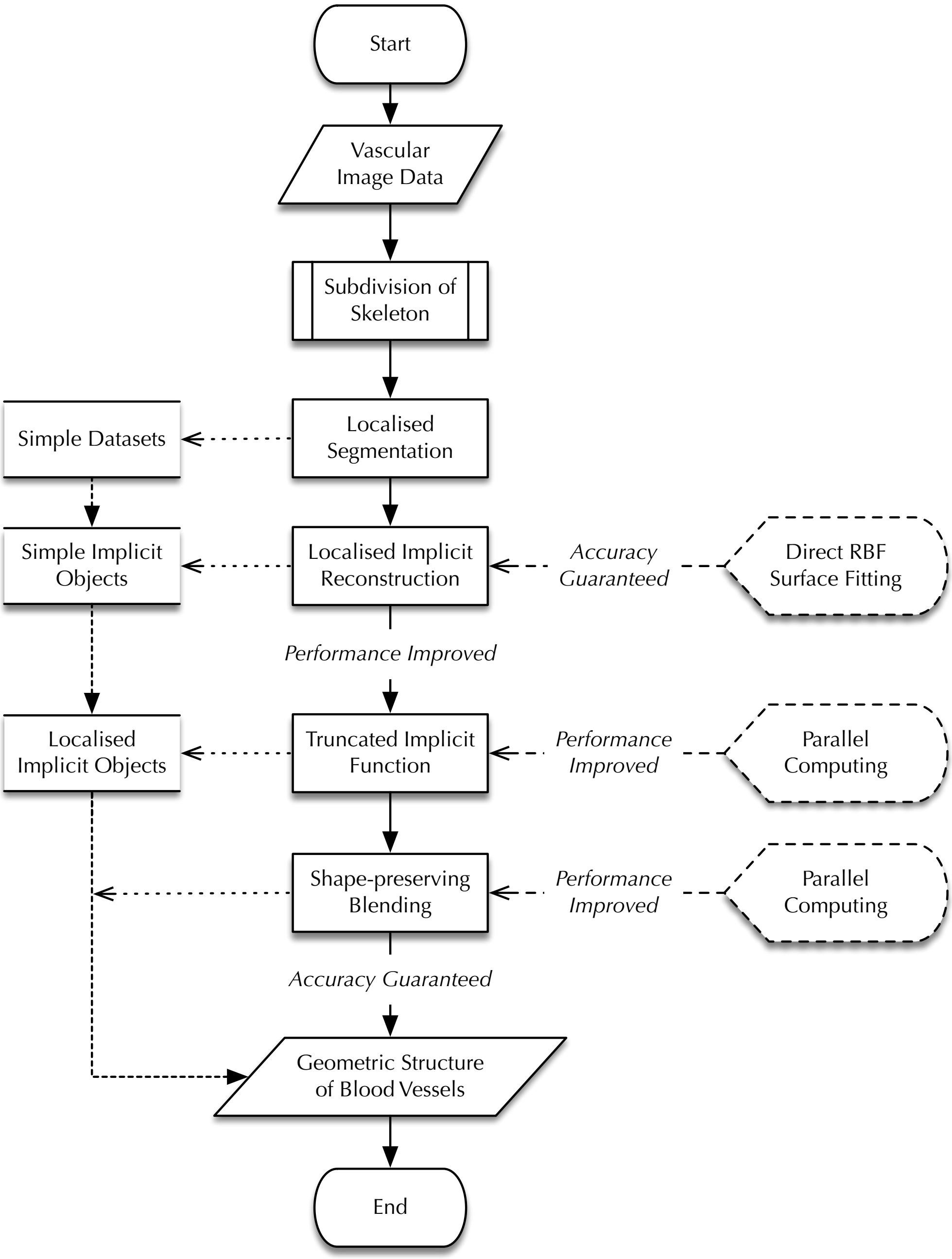

Figure 3.1: Flowchart of Skeleton Marching

difficult to produce satisfactory results for both large and small blood vessels globally. A localised region marching along the skeleton of the blood vessel is proposed to subdivide a vascular modelling into small modelling tasks for producing more robust and more accurate reconstruction results. The localised region on the skeleton contains a short segment of a blood vessel and this segment is going to be reconstructed as a localised implicit object. This object is a small generalised cylinder whose position and size are determined by the length and curvature of the skeleton enclosed in it.

In order to subdivide a blood vessel into short vascular segments with a reasonable shape, the skeleton of this blood vessel is regarded as a parametric curve such that its curvature and length can be acquired for the subdivision.

Suppose a 3D curve is represented as a parametric function $\boldsymbol{\gamma} : (\alpha, \beta) \to \mathbb{R}^3$, then the skeleton of a blood vessel can be represented as a parametric curve (Pressley 2010)

$$\boldsymbol{\gamma}(t) = (x(t), y(t), z(t)), t \in (\alpha, \beta) \tag{3.1}$$

The curvature of the curve $\boldsymbol{\gamma}$ is given by

$$\kappa = \frac{\|\dot{\boldsymbol{\gamma}} \times \ddot{\boldsymbol{\gamma}}\|}{\|\dot{\boldsymbol{\gamma}}\|^3} \tag{3.2}$$

The length of the curve started from point $\boldsymbol{\gamma}(t_0)$ is given by

$$s(t) = \int_{t_0}^{t} \|\dot{\boldsymbol{\gamma}}(u)\| du \tag{3.3}$$

With the curvature and length, a long and curvy skeleton can be subdivided into shorter and less curvy segments such that the corresponded vascular segments are in simple shapes. The neighboured segments will share an overlapped part which will be used as the blending connection after these segments being reconstructed as localised implicit objects.

This subdivision is delineated in Algorithm 1, which generates a set of knot pairs $\mathsf{seg}_k = (\alpha_k, \beta_k)$. One knot pair marks the two ends of a skeleton segment. The shape of this segment is controlled by L and K such that the curve of the segment is neither too long nor too curvy. Consequently the localised region surrounded the skeleton segment is simple enough. The data points in this small region can be easily extracted and reconstructed to be a localised implicit object.

In order to smoothly blend the neighboured localised implicit objects together, Algorithm 1 is designed that the start endpoint α_k of knot pair seg_k is in the middle of knot pair seg_{k-1}. This overlapped region is long enough to avoid unwanted bulges when blending.

Figure 3.2 gives an example of this subdivision. A medical volume containing a blood vessel is rendered in Figure 3.2(a). This blood vessel is very curvy and is

```
Algorithm 1: Division of an Unbranched Skeleton
parameter: $L$: threshold of length
           $K$: threshold of curvature
input    : curve: $\mathcal{C} = \{\boldsymbol{\gamma}(t) : t \in (\alpha, \beta)\}$
           knots: $\alpha = t_0 < t_1 < \cdots < t_n = \beta$
output   : knot pair: $\mathsf{seg}_k = (\alpha_k, \beta_k)$

$k \leftarrow 0$ ;
while $t_{i+1} \neq \beta$ do
    $i \leftarrow 0$ ;
    $j \leftarrow i + 1$ ;
    $\mathsf{len} \leftarrow s(t_j) - s(t_i)$ ;
    $\mathsf{cur} \leftarrow |\kappa(t_j) - \kappa(t_i)|$ ;
    if $\mathsf{len} > L$ or $\mathsf{cur} > K$ then
        $\mathsf{seg}_k \leftarrow (t_i, t_j)$;
        $k \leftarrow k + 1$ ;
        $i \leftarrow j$ ;
        $j \leftarrow i + 1$ ;
    else
        $j \leftarrow j + 1$ ;
    end
end
```

expected to be subdivided into shorter and less curvy segments. In Figure 3.2(b), a skeleton is shown as a curve inside the blood vessel. Nine markup knots are located with Algorithm 1, each markup knot α_k is paired with α_{k+2} such that two consecutive segments share a common part. These nine markup points produce seven segments shown in Figure 3.3.

3.2.2 Localised Implicit Reconstruction

Subdivision of vascular skeleton simplifies the reconstruction of a blood vessel by breaking down a big modelling task into many small sub-tasks. Due to the simplicity of each local vascular shape, the localised reconstruction of the region surrounded a skeleton segment is simple, accurate and efficient.

A skeleton segment is a short curve inside a localised blood vessel. The shape of the blood vessel segment is small and simple such that the point data of the vascular segment can be collected with any possible image segmentation algorithm. Consider the two end points of the segment have been determined, implicit deformable model is used in this research (Antiga et al. 2008). This segmentation technique evolves a level set inside a blood vessel from its start point to the endpoint and the points on

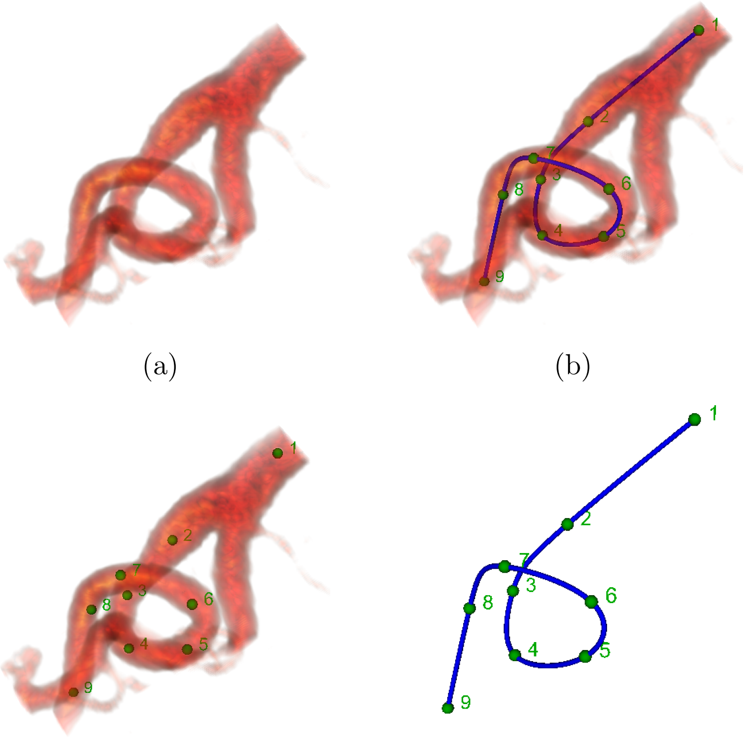

(a) (b)

(c) (d)

Figure 3.2: Subdivision of a Skeleton

the surface of the blood vessel are collected segment by segment. For a small blood vessel segment, this algorithm gives efficient and effective segmentation results.

Figure 3.4 presents localised segmentation results of seven vascular segments from a curvy blood vessel. Each segmentation result is a scatter point cloud. From Figure 3.4(a) to Figure 3.4(g), meshes are rendered with the data points for better observation. In Figure 3.4(h), all the data points are shown with different colours.

The localised segmentation collects the surface point clouds of the small blood vessels corresponding the skeleton segments. Each point cloud is a small dataset with a capsule-like shape and is expected to be reconstructed as a surface. Because of the simplicity of the small dataset, an uncomplicated surface fitting algorithm is preferred.

By using the implicit deformable model segmentation method (Antiga et al. 2008), the localised segmentation result is always a closed point cloud without holes and self-intersections, as shown in Figure 3.4. Although some of them have curvy parts, the general shape is always a capsule or deformed ellipsoid. Under such conditions, the direct Radial Basis Function (RBF) surface fitting with ellipsoid constraints is selected to reconstruct these localised blood vessel segments, which is a high-accuracy surface fitting method designed for small datasets (Li et al. 2004b).

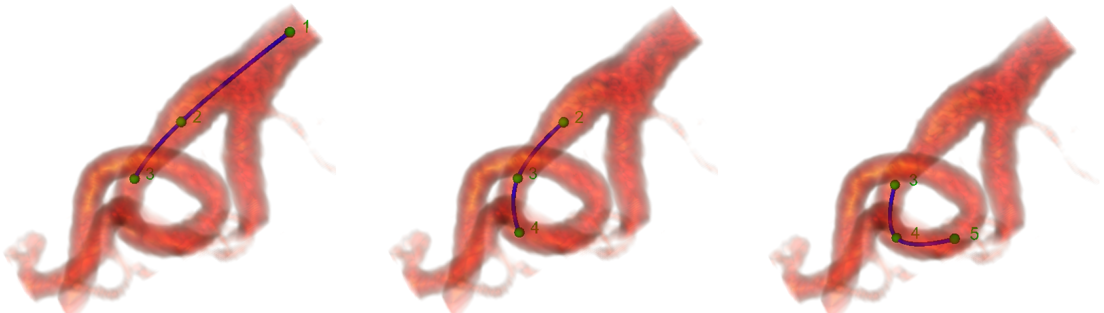

(a) Segment 0 (b) Segment 1 (c) Segment 2

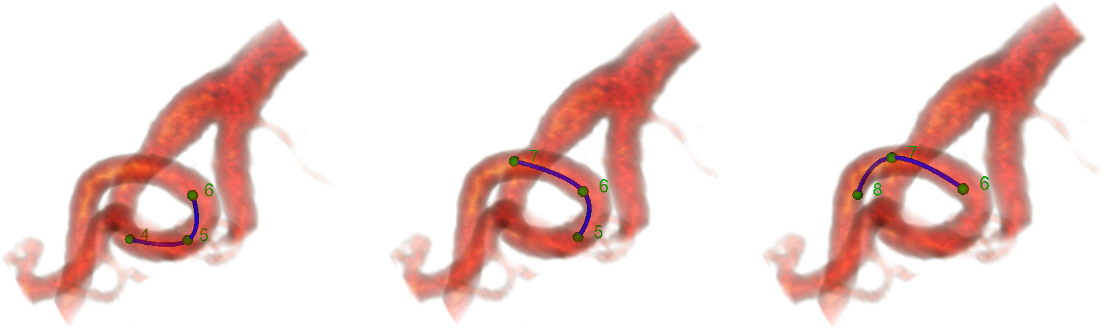

(d) Segment 3 (e) Segment 4 (f) Segment 5

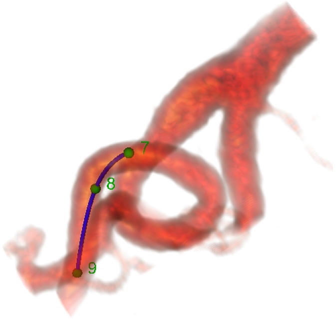

(g) Segment 6

Figure 3.3: Subdivided Skeleton Segments

In general, RBF method discretises implicit function as a linear combination of radial basis functions $\{\phi_i\}_{i=1}^n$ centred at the input surface points $\{\mathbf{P}_i\}_{i=1}^n$ (Canezin 2016; Coombe 2006), such that the implicitly blended function $\sum_{i=1}^n \gamma_i \phi_i(r_i)$ is the desired implicit surface, where r_i is distance from a general point $\mathbf{P}$ to the i-th point $\mathbf{P}_i$, and γ_i is the weight of the i-th radial basis function ϕ_i (Li et al. 2004a,b). The primary advantage of RBF is that no connection information of point in the dataset is required.

The general form of a radial basis function is:

$$f(\mathbf{X}) = \sum_i \gamma_i \phi(\|\mathbf{X} - \mathbf{C}_i\|) \tag{3.4}$$

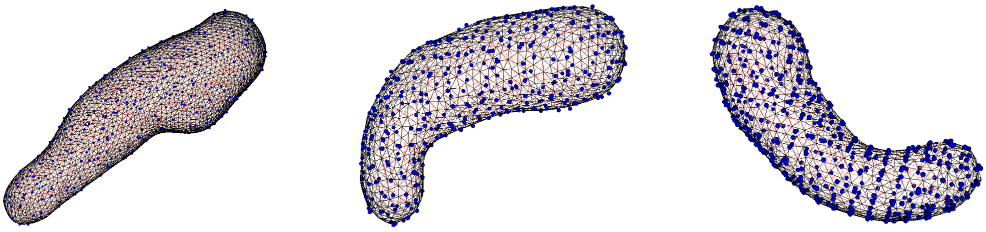

(a) 308 points (b) 384 points (c) 574 points

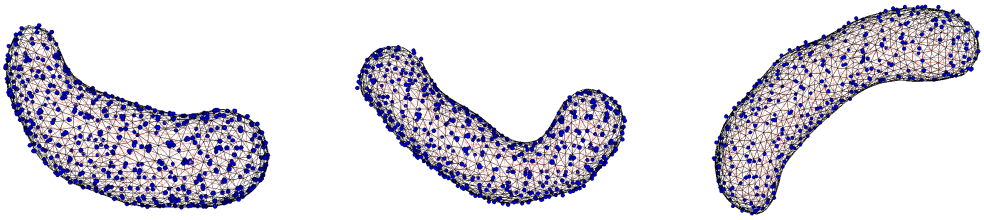

(d) 568 points (e) 568 points (f) 352 points

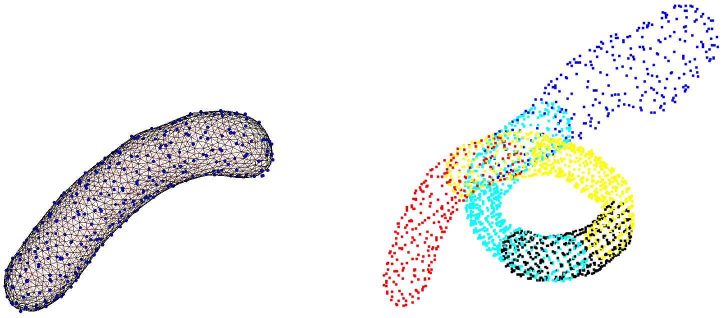

(g) 303 points (h) 3057 points

Figure 3.4: Localised Segmentations of a Curvy Blood Vessel

where $\gamma_i \in \mathbb{R}$ are the coefficients of the basis function and $\mathbf{C}_i$ are the centres of data points.

The direct RBF surface fitting with ellipsoid constraints is based on an assumption that the RBF-based surface fitting problem can be regarded as a blending of two implicit surfaces: a surface fitted by radial basis functions and a surface modelled by a low degree polynomial. Since the implicit surface of a radial basis function is always a blobby model, a polynomial constraint representing a closed-surface, such as an ellipsoid, is an ideal choice to deform the blob to be the desired shape.

Given a set of points $\mathcal{P} = \{\mathbf{P}_i\}_{i=1}^{n}$ from a surface, the direct RBF fitting with ellipsoid constraint is to fit points set $\mathcal{P}$ as an implicit function $f(\mathbf{X})$:

$$f(\mathbf{X}) = \sum_{i=1}^{n} \gamma_i \phi_i(\|\mathbf{X} - \mathbf{P}_i\|) + \sum_{j=1}^{m} \beta_j \psi_j(\mathbf{X}) \qquad (3.5)$$

where ϕ is a radial basis function and $\sum_{j=1}^{m} \beta_j \psi_j(\mathbf{X})$ is a polynomial always representing an ellipsoid, $\mathbf{X} = (x, y, z)$ is a general point.

Assume $f(\mathbf{P}_i) = 0, i = 1, 2, \ldots, n$, then $f(\mathbf{X}) = 0$ can be expressed in the following matrix form:

$$\begin{bmatrix} \Phi & \Psi \\ \Psi^T & 0 \end{bmatrix} \begin{bmatrix} \boldsymbol{\gamma} \\ \boldsymbol{\beta} \end{bmatrix} = \begin{bmatrix} 0 \\ 0 \end{bmatrix} \tag{3.6}$$

where

$$\begin{aligned} \Phi &= [\phi_1, \phi_2, \ldots, \phi_n] \\ \Psi &= [\psi_1, \psi_2, \ldots, \psi_m] \\ \boldsymbol{\gamma} &= [\gamma_1, \gamma_2, \ldots, \gamma_n]^T \\ \boldsymbol{\beta} &= [\beta_1, \beta_2, \ldots, \beta_m]^T \end{aligned}$$

As shown in (Li et al. 2004b), the solution to Equation 3.6 can be obtained by solving an eigensytem subject to the condition that $\sum_{j=1}^{m} \beta_j \psi_j(\mathbf{X})$ always represents an ellipsoid.

The direct RBF surface fitting with ellipsoid constraint is especially suitable for the reconstruction of small datasets like the localised segmentation results shown in Figure 3.4. For one thing, this method is fast for small dataset. As a one-step fitting algorithm based on the solution of the eigensystem in Equation 3.6, this direct fitting technique does not require additional information such as surface normals and extra fitting layers. The fitting is fast when the dataset is small. In addition, because of the ellipsoid constraint, this method always gives bounded fitting results which is the expected shape of a vascular segment. As the fitting results are expressed as implicit functions, it is easier to combine the reconstructed vascular segments together using implicit blending operations. Furthermore, since each closed vascular segment has a simple shape, the corresponding implicit shape has a simple form, whose computational cost can be dramatically saved. This will be discussed in the next section. The last but not least, this method is a high-accuracy surface fitting method when the shape of the datasets are simple. The fitting errors are very small and can be negligible.

Figure 3.5 presents localised modelling results of a curvy blood vessel corresponding the segmentation results of Figure 3.4. Both the reconstructed surfaces and the data points are rendered. The whole curve blood vessel is given in Figure 3.5(h). It is the blending result of the implicit objects shown in other seven subfigures. The blending smoothness can be any degree by using the shape-preserving blending operators in Equation 2.12, but in this figure the smoothness degree is set to $n = 2$ with a smoothness span controller $\delta = 0.2$.

Table 3.1 gives the distance errors of the localised modelling results of the seven subfigures in Figure 3.5(a) to Figure 3.5(g). The distance is measured from each data point to the reconstructed surface. The distance error is evaluated by the standard deviation of all the distances of a localised reconstruction result. It is shown that the errors are so small that the data points can be regarded as on the surface.

Table 3.1: Distance Error of the Localised Implicit Reconstruction

Localised Reconstruction	Number of Points	Standard Derivation (millimetres)
(a)	308	2.46677×10^{-10}
(b)	384	1.56189×10^{-10}
(c)	574	1.49556×10^{-9}
(d)	568	1.72521×10^{-9}
(e)	568	2.89805×10^{-10}
(f)	352	4.96290×10^{-10}
(g)	303	1.31824×10^{-10}

3.2.3 Localised Implicit Object

The localised reconstruction of vascular segments generates a group of bounded small implicit objects $\mathcal{O}_0, \mathcal{O}_1, \dots \mathcal{O}_n$, which are defined by a set of implicit functions $f_0, f_1, \dots, f_n$ in an image space $\mathbb{U} \subset \mathbb{R}^3$. Although each individual implicit object $\mathcal{O}_i$ takes only a small region $\mathbb{U}_i \subset \mathbb{U}$, the evaluation of the corresponding implicit function f_i is crossing the whole image space $\mathbb{U}$. Its evaluation is expected to be limited inside $\mathbb{U}_i$ and as the implicit object $\mathcal{O}_i$ is only a locally defined implicit object.

Definition 3.1 (Localised Implicit Object)**.** An implicit object $\mathcal{O}_* = \{\mathbf{X} \in \mathbb{U}_* : f(\mathbf{X}) \leqslant 0\}$ is said to be a *Localised Implicit Object* if it is a bounded object defined in $\mathbb{U}_* \subset \mathbb{U}$, such that $\{\mathbf{X} \in \mathbb{U}_* : f(\mathbf{X}) \leqslant 0\} = \{\mathbf{X} \in \mathbb{U} : f(\mathbf{X}) \leqslant 0\}$, where $\mathbb{U} \subset \mathbb{R}^3$.

A localised implicit object $\mathcal{O}_i$ is a set defined in domain $\mathbb{U}_i \subset \mathbb{U}$ and is expected to be blended with another localised implicit object $\mathcal{O}_j$ defined in $\mathbb{U}_j \subset \mathbb{U}$. However, these two implicit objects cannot be blended together directly because the domains of the corresponding implicit functions are different. In order to achieve this blending, their domains have to be extended to the origin domain $\mathbb{U}$. The truncated implicit function is used to do this extension.

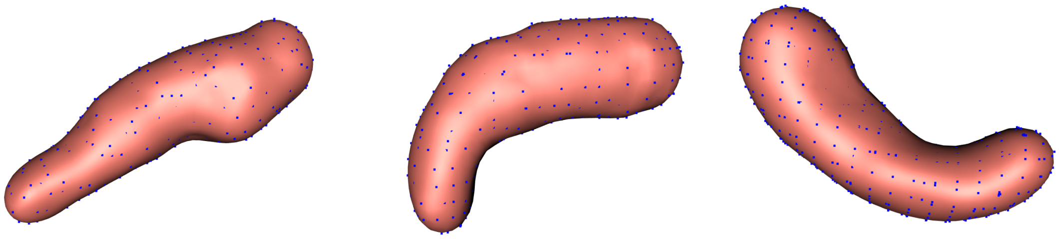

(a) Segment 0 (b) Segment 1 (c) Segment 2

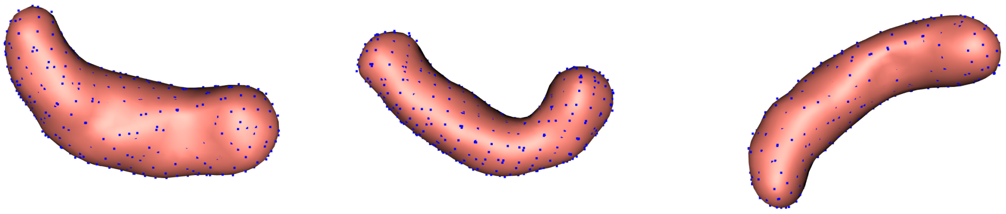

(d) Segment 3 (e) Segment 4 (f) Segment 5

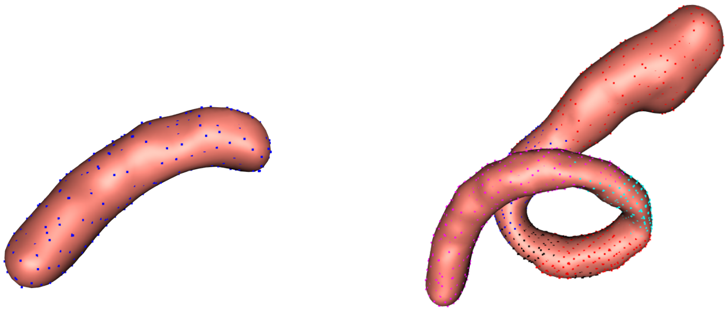

(g) Segment 6 (h) Blending Result

Figure 3.5: Localised Reconstruction of a Curvy Blood Vessel

Definition 3.2 (Truncated Implicit Function)**.** A field function $\bar{f} : \mathbb{R}^3 \to \mathbb{R}$ is said to be a *Truncated Implicit Function* (*TIF*) of an implicit function f if there exists a sub-domain $\mathbb{U}_* \subset \mathbb{R}^3$, such that the implicit solid $\mathcal{O}_* = \{\mathbf{X} \in \mathbb{U}_* : \bar{f}(\mathbf{X}) \leqslant 0\}$ is a localised implicit object.

For a normal implicit function f, let $\mathbb{U}_*$ be the domain on which it is truncated, then the truncated implicit function of f on $\mathbb{U}_*$ can be expressed in the following form: The truncated implicit function $\bar{f}$ equals to a normal implicit function f inside $\mathbb{U}_*$ but is truncated outside the domain. With the truncated implicit function, a localised implicit object can be defined as:

$$\bar{f}(\mathbf{X}) = \begin{cases} f(\mathbf{X}) & \mathbf{X} \in \mathbb{U}_* \\ c \gg 1 & \text{otherwise} \end{cases} \tag{3.7}$$

where c is a sufficient large constant.

With the truncated implicit function, a group of localised implicit objects can be quickly evaluated inside their localised defining domains and be blended together in a global domain. It dramatically improves the performance of the geometric reconstruction process when the number of the localised implicit objects is large and sizes of them are small.

Figure 3.6 demonstrates how the truncated implicit function works. In Figure 3.6(a), isocontours of implicit function $f(x, y) = (0.5x^2 - 1)^2 + 2y^2 - 1.2$ are shown and the 0 level set $Z(f) = \{f = 0\}$ is marked. Since an implicit object is an interior implicit solid $\{f \leqslant 0\}$, the evaluation outside $Z(f)$ should be avoided. In Figure 3.6(b), the implicit function f has been truncated to be inside a sub-domain enclosing $Z(f)$ such that the unwanted evaluation outside this sub-domain is eliminated.

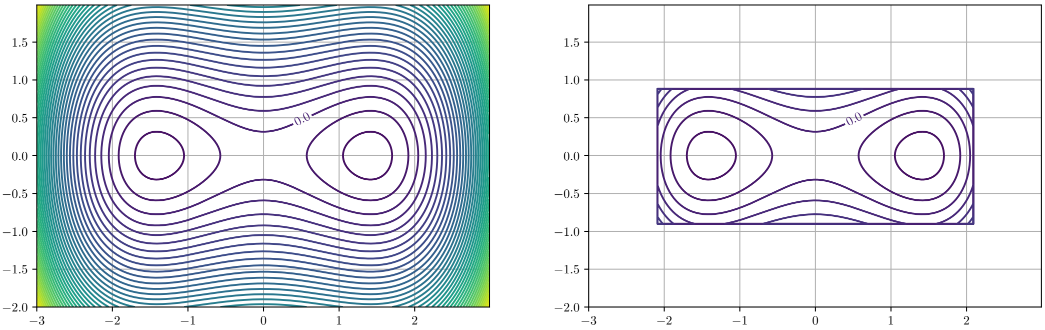

(a) Isocontours without TIF

(b) Isocontours with TIF

Figure 3.6: Isocontours of an Implicit Function

However, since an implicit function cannot explicitly represents an implicit surface, there is no direct way to generate points or surfaces of an implicit function (Bloomenthal 1995b). In order to located the sub-domain $\mathbb{U}_i$ of the localised implicit object $\mathcal{O}_i$, the location of the localised segmentation will be used as a substitution. Consider the small size of the localised segmentation, a minimum cubic bounding box is chosen to be the sub-domain $\mathbb{U}_i$.

Figure 3.7 shows the differences between a globalised implicit object and a localised implicit object with their minimum bounding box. The branched blood vessel has been subdivided into 41 simple vascular sections and their data points on the vascular walls, which are rendered as blue points, have been extracted by the implicit deformable model segmentation method (Antiga et al. 2008). A same one simple vascular section has been reconstructed as a capsule-like object with red colour. Although the two objects are geometrically identical, they are generated from difference domains. The fitting of Figure 3.7(a) uses the global domain and costs 35.34 seconds on a CPU. In contrast, Figure 3.7(b) costs 4.89 seconds inside a localised domain. The domains are marked with a red frame box. The whole point data are rendered in the figures to show the size of the global domain.

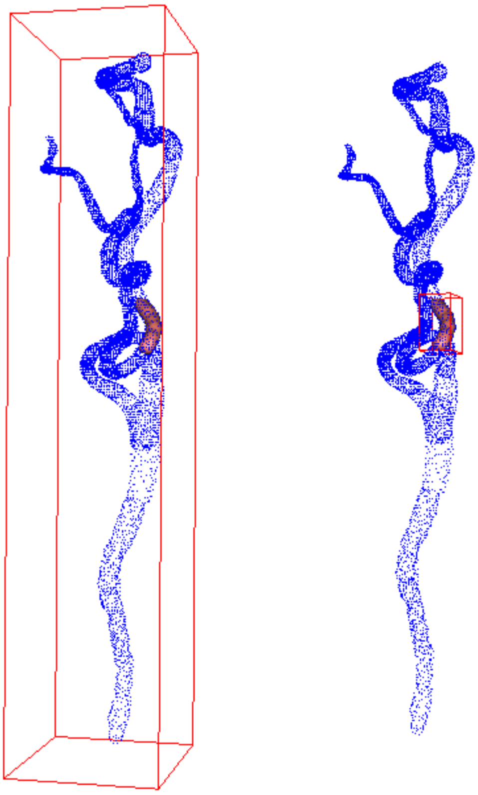
(a) (b)

Figure 3.7: Globalised Implicit Object and Localised Implicit Object

Table 3.2 compares the fitting speeds of the blood vessel segments in Figure 3.5. The globalised fitting costs much more time than the localised fitting since the localised fitting uses truncated implicit function such that only the sub-domain of the localised implicit object is evaluated and the fitting is much faster.

Table 3.2: CPU Fitting of Blood Vessel Segments (seconds)

Segment	Number of Points	Globalised Fitting	Localised Fitting
0	308	34.76	5.16
1	384	42.45	5.21
2	574	60.61	6.25
3	568	62.24	5.71
4	568	61.03	5.73
5	352	38.45	5.13
6	303	35.34	4.89

Figure 3.8 compares the fitting speed of each blood vessel segments. The speed remains at a low level of the globalised fitting using the normal implicit function. Averagely nine points are fitted per second. In contrast, the fitting speed of using

the localised implicit function is about ten times faster, and the speed is growing when the number of points is increasing.

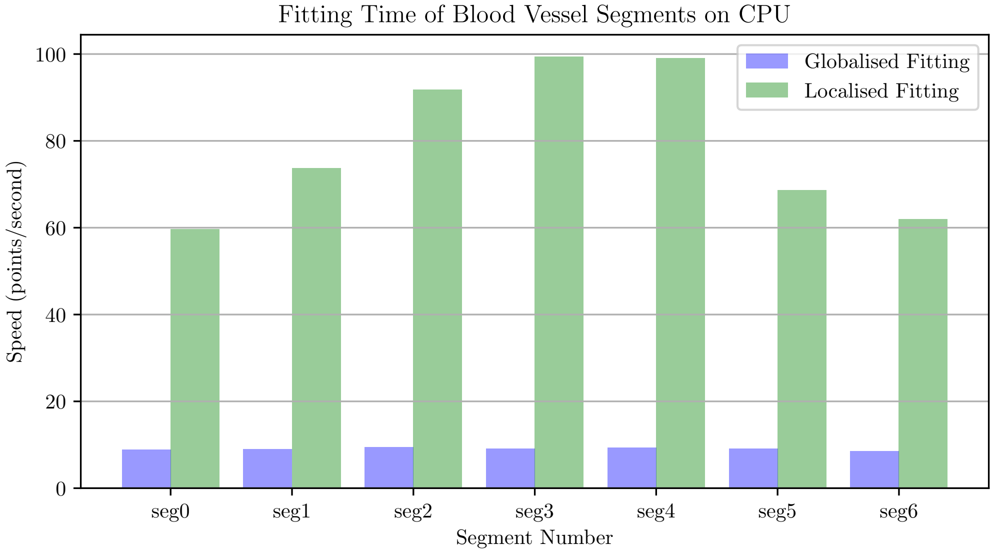

Figure 3.8: CPU Fitting Comparison of Blood Vessel Segments

By using the truncated implicit function, the fitting speed of the localised implicit object is dramatically improved at the algorithmic level. Since the fitting of one localised implicit object is independent to the others, the fitting efficiency can be further improved by using parallel computing techniques.

3.2.4 Parallel Computing

The subdivision of vascular skeleton turns a big modelling task into many small subtasks, each of them is regarded as a localised reconstruction and generates a localised implicit object. A notable feature of the localised implicit objects is that they are independent to the others such that the localised reconstructions are friendly with parallel computing techniques.

Parallel computing is a computational technique that simultaneously carries out a calculation as many sub-calculations to improve the computational efficiency (Almasi et al. 1989). There are several different types of parallel computing, but only data parallelism is used in this research.

Data parallelism distributes the data across multiple processors for parallel computing. It receives great attentions with the fast developing of General-purpose Computing on Graphics Processing Units (GPGPU). The massive parallel processors and memories on a GPGPU are able to process complicated tasks in a parallel manner and significantly improve the computational efficiency (Owens et al. 2007).

Data parallelism has been used on the RBF fitting with ellipsoid constraint to improve the performance of the vascular reconstruction. For a point cloud $\mathcal{P} = \{\mathbf{P}_i\}_{i=1}^n$ from the localised segmentation, the implicit function Equation 3.6 is expressed and distributed over the GPGPU as a kernel of parallel computing. The solution is transferred back to the host programme on CPU for further processing.

Table 3.3 compares the fitting time of the blood vessel segments based on Table 3.2. In this table, column 3 and 4 show the globalised fitting time on CPU and GPU. The improvement of the fitting on GPU is significantly. Column 5 and 6 give the localised fitting on CPU and GPU, but the fitting on GPU is even slower. This is because the localised implicit objects of the blood vessel segments are too small to be accelerated. Data transformation between CPU and GPU slows down the acceleration. The fitting speed comparison is given in Figure 3.9. The experiments are remotely running on an HPC with an Intel(R) Xeon(R) CPU E5–2680 and a Nvidia Tesla K40M GPU.

Table 3.3: Fitting Time of Blood Vessel Segments (seconds)

		Globalised Fitting		*Localised Fitting*	
Segment	Number of Points	CPU	GPU	CPU	GPU
0	308	34.76	5.48	5.16	5.47
1	384	42.45	6.00	5.21	5.49
2	574	60.61	7.12	6.25	6.10
3	568	62.24	7.01	5.71	6.15
4	568	61.03	7.12	5.73	6.15
5	352	38.45	5.66	5.13	5.72
6	303	35.34	5.57	4.89	5.41

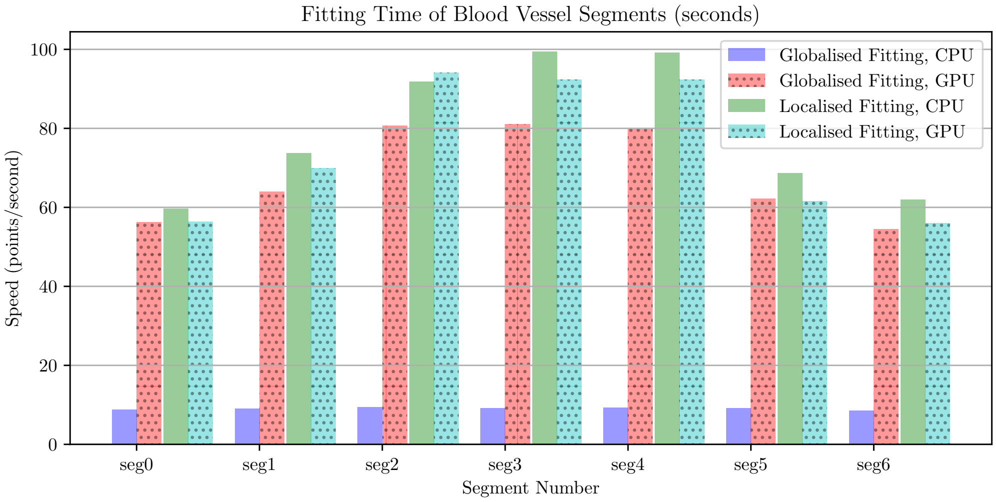

Figure 3.9: Fitting Speed Comparison of Blood Vessel Segments

Besides the data parallelism of the modelling on one implicit object, multiple localised modellings can be processed concurrently. This is also regarded as task parallelism (Subhlok et al. 1993). Localised implicits and localised modelling are designed for this purpose. Because the calculation of one localised implicit object is independent of the others, different localised implicits can be configured into different streams for concurrent computing. What is more, higher parallelism can be achieved when multiple GPU devices are available.

3.3 Discussion and Experiments

A skeleton marching technique is proposed in this chapter using the localised implicit objects for the reconstruction of blood vessels. The segmentation, surface fitting and parallel computing of a single localised implicit object have been discussed to illustrate the proposed method. However, it is worth to stress that this method is designed for the reconstruction of the vascular tree rather than blood vessel segments. This section discusses the advantages and limitations of the proposed method with further experiment results.

3.3.1 Discussion

The vascular reconstruction with skeleton marching is a high-accuracy and high-performance computation vascular reconstruction method. Compared with the sweep surface method, it has several distinctive advantages on blood vessel reconstruction:

- No coordinate transformation is required. Each vascular segment is reconstructed to be a localised implicit object inside the image space. This reconstruction does not need the Frenet coordinate.

- The dataset of each localised reconstruction does not need to be sorted out. The reconstruction of a vascular segment is a surface fitting on an unorganised dataset. The coordinates of the data points are the only prerequisite of this fitting.

- All data points are used by the proposed method. The reconstruction of a blood vessel segment is based on a 3D point cloud rather than a surface of points. No data point will be neglected.

- The fitting of a localised implicit object is a one-step fitting. The data points of a vascular segment are directly reconstructed as an implicit object. No further fitting operation is required.

- The proposed method is a high-performance computation vascular reconstruction. On the one hand, the localised implicit object limited the evaluation of each vascular segment reconstruction inside a small region. The fitting efficiency is dramatically improved. On the other hand, the proposed method is parallel computing-friendly. All localised implicit objects can be reconstructed in a parallel manner to save more computational time.

- This vascular reconstruction is a high-accuracy implicit modelling technique. For one thing, the direct RBF fitting with ellipsoid constraint is a high-accuracy surface fitting method. Various shapes can be accurately captured and represented. For another, the blended shape of the localised implicit objects are preserved as much as possible by using the shape-preserving implicit blending operations. Both the smoothness degree and smoothness span can be flexibly controlled to adjust the blending results.

The main drawback of the proposed method is the overuse of data points. In order to blend neighboured vascular segments together, each segment has overlapped regions with its neighbours and the data points in these regions will be processed twice. This overuse of data points guarantees the smoothness of blending result but slightly declined the modelling efficiency. However, the size of the overlapped region are controlled by the length and curvature of the vascular segments such that this negative issue can be suppressed as much as possible. This overuse can be observed in Figure 3.4(h). The size of the overlapped regions will be optimised in the future work.

In the rest of this section, the reconstructions of an unbranched blood vessel, a branched blood vessel and a blood vessel tree are presented to demonstrate how the proposed method works.

3.3.2 Experimental Results

Unbranched Blood Vessel

In the previous parts of this chapter, the reconstruction of an unbranched blood vessel has been detailedly discussed. In this section, another reconstruction of an unbranched blood vessel is presented in Figure 3.10. Figure 3.10(a) shows a volume rendering of this blood vessel. The skeleton has been represented as a cubic Hermite spline and 13 ordered knots have been positioned on it using Algorithm 1. Spline segments are divided in such a way that knot t_i is paired with t_{i+2}. Each segment overlaps with its neighbours, this is to make sure that the adjacent locally fitted implicits blended smoothly. Figure 3.10(b) gives the localised segmentation of each spline segment. Random colours distinguish different point clouds, for which small and simple shapes can be observed. Figure 3.10(c) shows the localised modelling result of one point cloud. Figure 3.10(d) presents the blending result of all modelling results with point clouds rendering. The shape-preserving blending operations are used (Li 2007). Figure 3.10(e) shows the reconstructed blood vessel without point clouds.

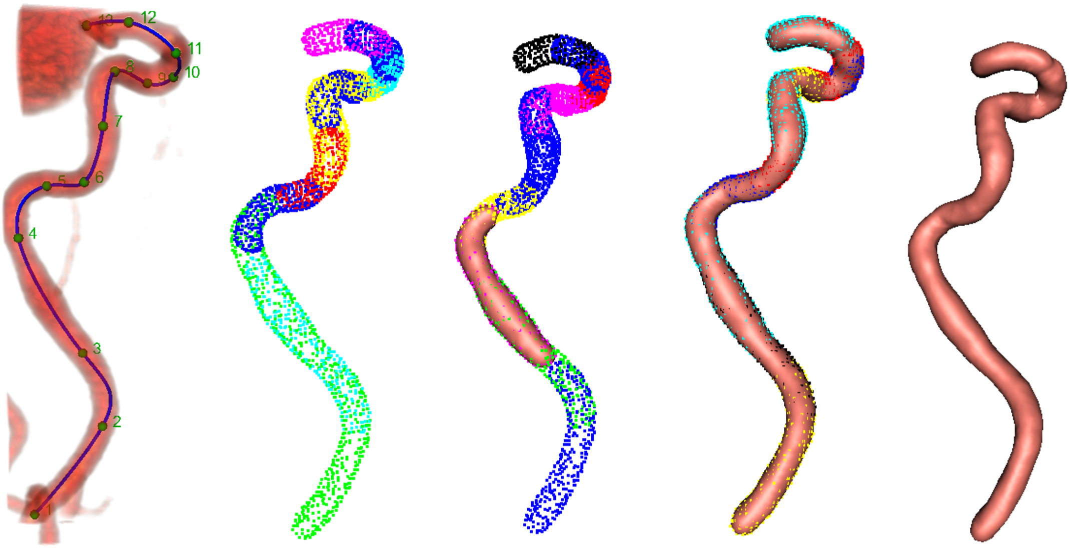

(a) (b) (c) (d) (e)

Figure 3.10: Reconstruction of an Unbranched Blood Vessel

Branched Blood Vessel

Figure 3.11 shows a branched blood vessel reconstructed with the proposed method. The blood vessel in Figure 3.10 can be found at the top right part. Figure 3.11(a), Figure 3.11(b) and Figure 3.11(c) give the point clouds, point clouds on blood vessel wall and blood vessel wall as implicit surface respectively.

This branched blood vessel consists of 59 segments from 7 smaller unbranched blood vessels. Each segment corresponds to a small point cloud extracted with localised segmentation. Small and simple-shaped implicit objects are fitted from these point clouds and then blended together to create the final result. The segmentation and surface fitting of one point cloud has no relation to the others and therefore are parallel-friendly. The underlying implicit function of the surface fitting is represented as truncated implicit function which makes the fitting very fast.

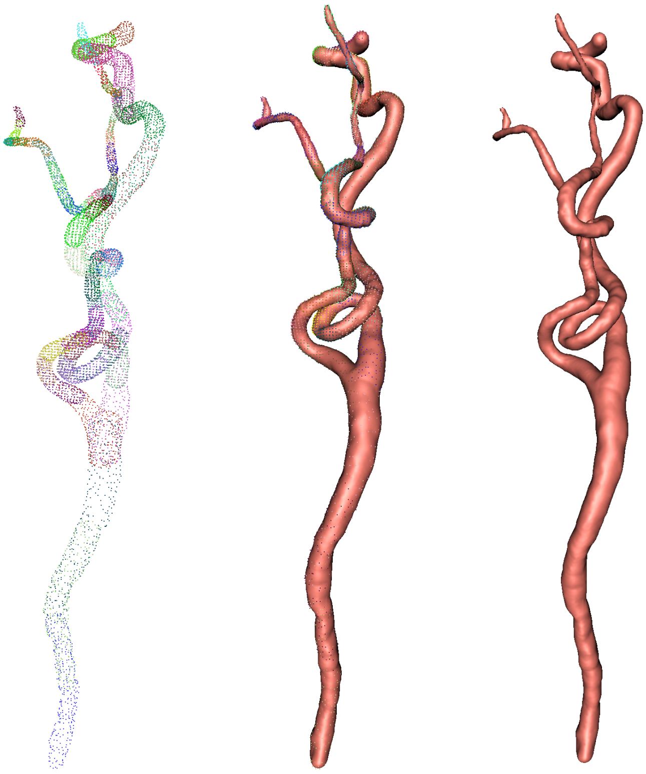

(a) (b) (c)

Figure 3.11: Reconstruction of a Branched Blood Vessel

Blood Vessel Tree

The reconstruction of a blood vessel tree is similar to the reconstruction of branched blood vessels. The blood vessel tree is firstly interactively disassembled into many unbranched blood vessels with overlapped parts to their neighbours. Then a single unbranched blood vessel is subdivided along its skeleton to be vascular segments with simple and less curvy shape. These small segments will be reconstructed into localised implicit objects.

Figure 3.12 presents a reconstructed blood vessel tree with 294 segments from 58 unbranched blood vessels. The original image is rendered as a volume in Figure 3.12(a). In Figure 3.12(b), the point clouds of the 294 segments are rendered with random colours. In Figure 3.12(c), both the points and the reconstructed surface are rendered. Figure 3.12(d) gives the reconstructed vascular tree without the points.

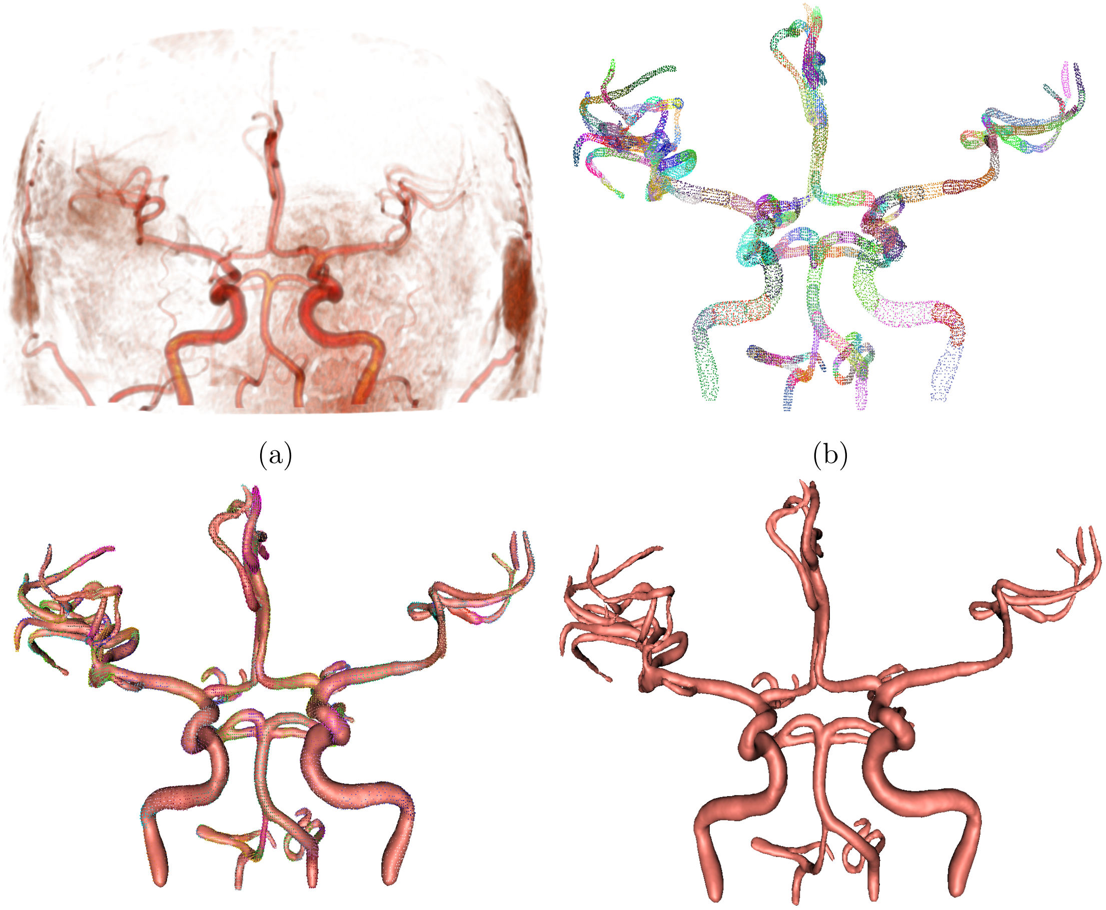

(a) (b)

(c) (d)

Figure 3.12: Reconstruction of Blood Vessel Tree

The flowchart in Figure 3.13 illustrates this reconstruction. Localised segmentation is applied on short blood vessel segments guided by skeleton segments, then localised segmentation results are fitted in parallel to produce a set of simple localised implicits. Implicit blending operation combines them together to get the final vascular tree. Compared with Figure 3.1, this figure emphasises the parallel computing used in the Skeleton Marching technique.

Parallel computing plays an important role in the proposed reconstruction method. For a single localised modelling on one point cloud, data parallelism aims at the acceleration of the RBF fitting. Multiple localised modellings are accelerated by task parallelism. This two-step parallel computing greatly improves the modelling performance.

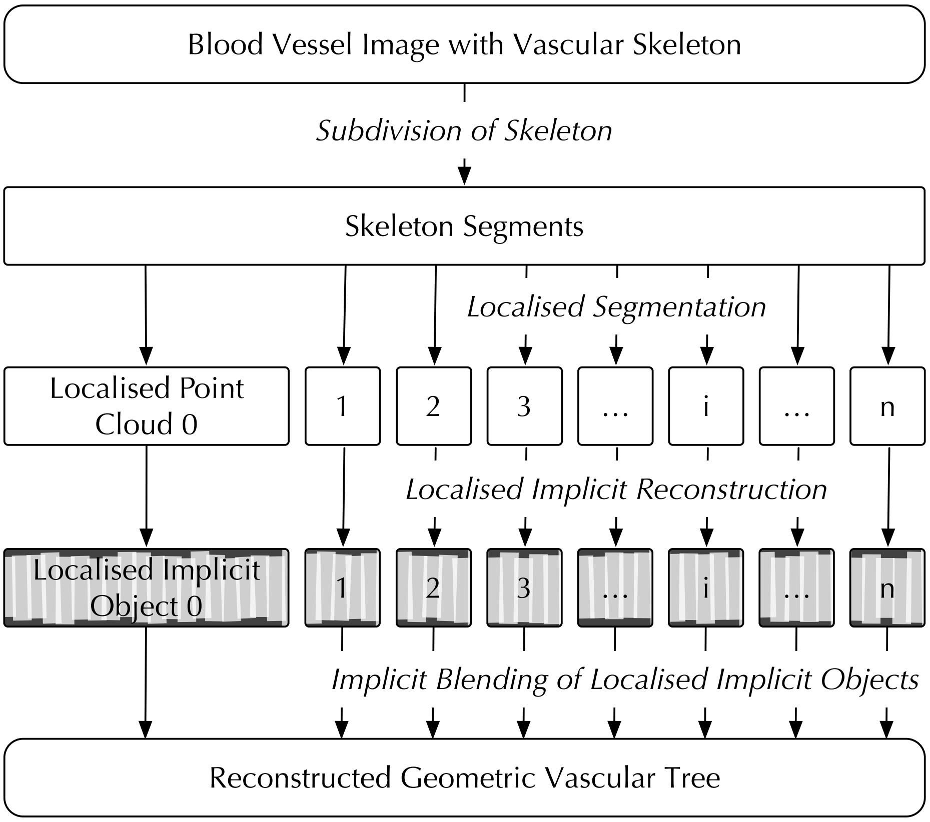

Figure 3.13: Flowchart of Skeleton Marching on Parallel Computing

Parallel Computing

Table 3.4 compares the performances of reconstructing blood vessel(s) on CPU and GPU with globalised fitting and localised fitting. Dataset A, B and C in the first column correspond to the reconstructed blood vessel(s) in Figure 3.10(c), Figure 3.10(e) and Figure 3.11(c)respectively. The number of data points of these datasets are $316, 4196$ and 17503.

Figure 3.14 gives a comparison of the modelling speed of the three examples in Table 3.4. The first bars show the globalised fitting speed on the CPU remains at a stable level. The second bars reflect the rapid growing of globalised fitting speed on the GPU when the number of data points increases. In contrast, the modelling speed differences between the localised fitting over the CPU and GPU are not such significant. The performance of the localised fitting on GPU is even worse than the CPU counterpart when the dataset is small, but its advantage is emerging with the increasing of the size of the dataset. This is because the localised fitting makes the evaluation of each fitting as small as possible, while parallel computing gives limited improvement on calculation with small sizes.

Table 3.4: Fitting Time of Blood Vessels (seconds)

		Globalised Fitting		*Localised Fitting*	
Example	Number of Points	CPU	GPU	CPU	GPU
A	316	36.70	5.79	5.40	5.61
B	4196	437.02	25.12	15.30	12.09
C	17503	1823.99	93.48	52.25	35.24

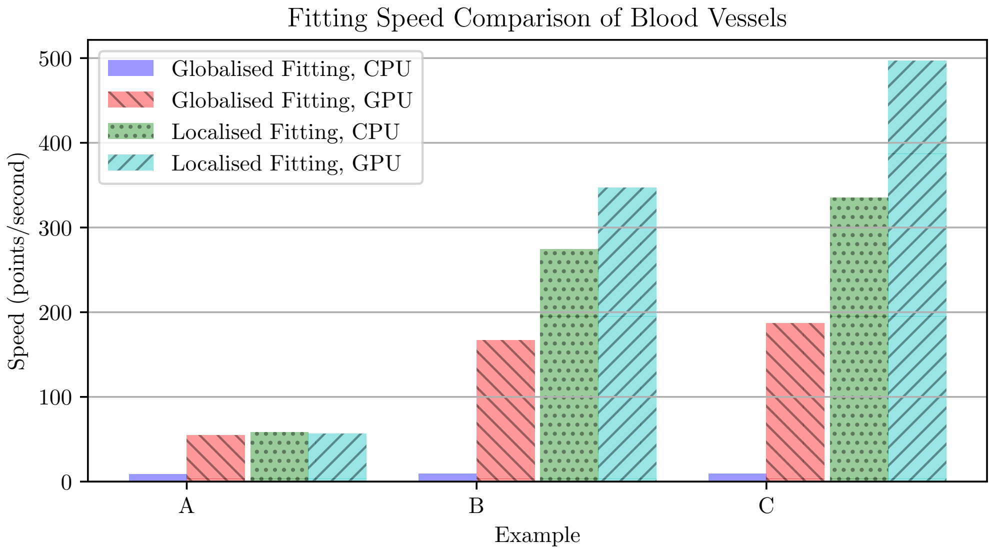

Figure 3.14: Fitting Speed Comparison of Blood Vessels

3.4 Summary

The skeleton-based vascular modelling is the mainstream approach on the accurate reconstruction of blood vessels out of medical images. Among the existing skeleton-based vascular modelling techniques, the sweep surface method allows a high-accuracy modelling results at the cross-sections but it is far less accurate at the vascular sections between two consecutive sweep surfaces. What is more, the performance of the this method is discounted on its two-step approximation. In order to avoid this problem and improve the performance of geometric vascular modelling, this chapter proposes skeleton marching technique to give a one-step and parallel-friendly geometric reconstruction of the blood vessels.

With the proposed technique, a vascular tree is firstly divided along the vascular skeleton into short simple blood vessel sections and a small simple point cloud is extracted from each of these vessel sections using a segmentation technique. Then a set of simple implicit shapes are reconstructed in parallel from the set of point clouds. A high-accuracy vascular tree is finally generated by blending these localised implicit objects together using shape-preserving blending operations. Compared with the CPU-intensive implementation, much less time is required using the proposed parallel implicit fitting technique.

Chapter 4

Vascluar Tissue Modelling with Thin Implicit Patch

4.1 Introduction

In geometric modelling, an object is usually represented as a surface which has no thickness. Although it is convenient to analyse and visualise surface-based objects, there are two limitations of representing objects as surfaces. For one thing, a surface-based object without thickness neither exists in real world nor can be manufactured in a proper way. Thickening techniques are required to covert a surface to be a thin solid for manufacturing. For another, a surface-based object lacks the description of interior structures of the corresponding real-world object. Even though a surface can be converted to a thin solid using a certain geometric processing tool, it is in general difficult to covert a traditional parametric representation into volumetric object with highly complex interior geometric structures (Wang et al. 2013).

In terms of vascular reconstruction, a blood vessel is commonly regarded as a long thin solid and represented as a tubular surface. The vascular wall is usually considered as a surface object such that its complex tissue structures are often ignored. However, as shown in Figure 4.1, a real vascular wall is not simply a surface object, it is actually a solid object with highly complicated multi-layer geometric structures. Combining accurately reconstructed vascular surfaces with realistically modelled interior vascular tissue structures is not only a necessary task for 3D vascular printing, but can make relevant analysis and simulation more accurate and more meaningful.

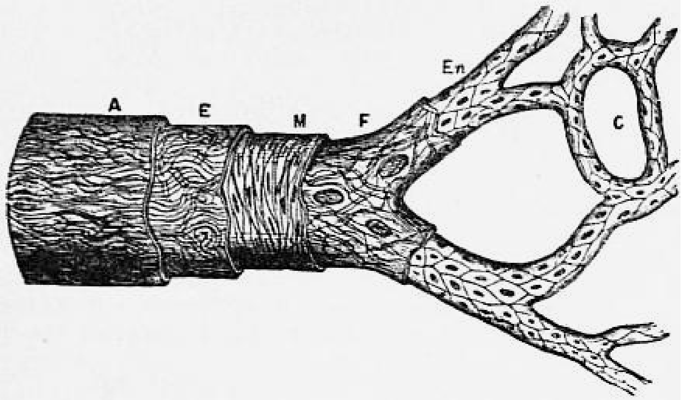

Figure 4.1: Diagram of the Structure of an Artery (Britannica 1911)

As can be seen later, reconstructing a vascular wall with a thickness and embedding interior structures can be easily achieved by using implicit modelling technique. This is mainly due to the fact that an implicit function is a field representation, which can be used to represent a geometric object both as a solid and a surface. Many objects in the real world cannot be simply treated as surface or solid, but mixtures of both, such as a blood vessel wall, a football, or an empty teapot. These objects have thin solid surfaces with specific internal material structures and it is not straightforward to effectively represent both their external shapes and their internal geometric structures. Implicit modelling provides an ideal representation for modelling real-world geometric objects. Secondly, implicit objects can be easily combined together to generate complicated objects. Therefore a thin solid object can be directly obtained from an implicit surface using certain implicit blending operations. In addition, once an object has been represented as an implicit function, it is easy to analyse its geometric properties, which is especially important for Computer-aided Manufacturing (CAM). What is more, when a surface geometry is represented implicitly, the surface-to-solid conversion operation is easier to operate and less computationally expensive than the method based on explicit representations (Maekawa 1999; Musialski et al. 2015).

This chapter discusses how to convert a surface-based object into a thin solid object with a required interior geometric structure using implicit modelling technique. A novel technique called Thin Implicit Patch (TIP) is proposed for modelling solid objects with their internal geometric structures. With the thin implicit patch, any surface-based objects can be easily converted into thin implicit surfaces. Any required interior structures can then be designed and embedded inside the thin surfaces for the purpose of additive manufacturing. Figure 4.2 illustrates the thin implicit patch technique.

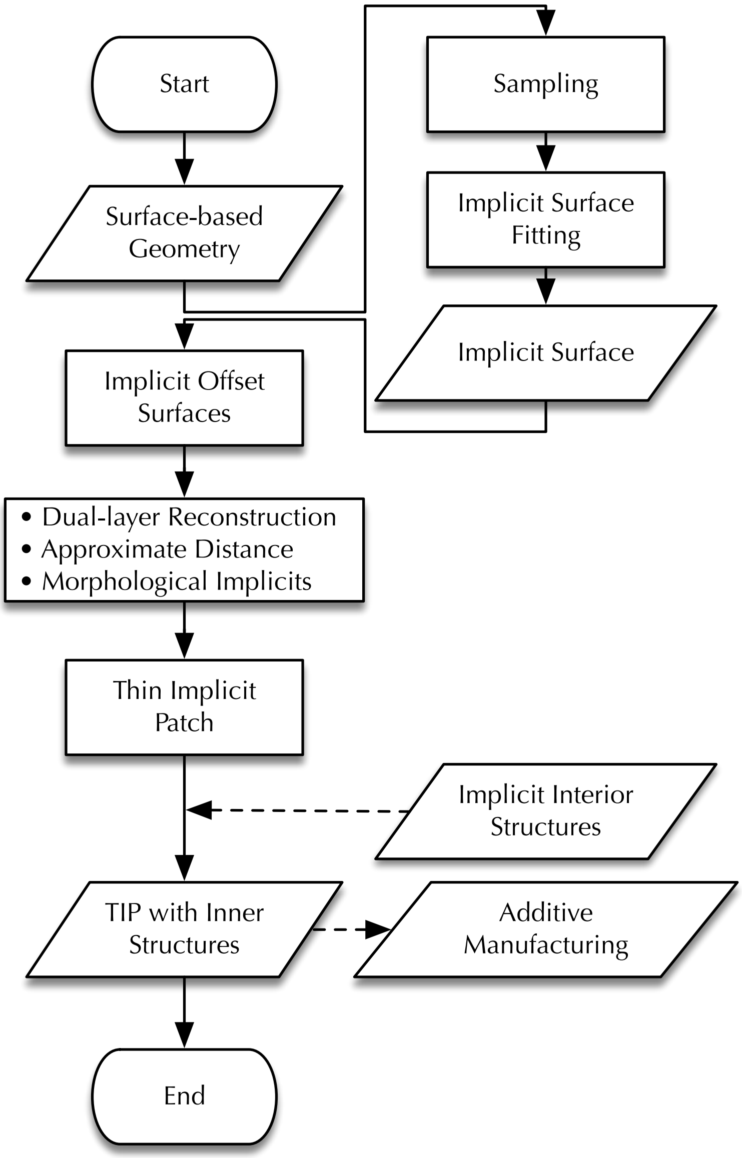

Figure 4.2: Flowchart of Thin Implicit Patch

4.2 Thin Implicit Patch

A Thin Implicit Patch (TIP) is a thin implicit solid in 3D space. In contrast with thickened thin solid converted from parametric surfaces, a thin implicit patch is directly represented as an implicit function.

Definition 4.1 (Thin Implicit Patch)**.** An implicit object Ξ defined by a field function $f(\mathbf{X})$ is said to be a *Thin Implicit Patch (TIP)* if there exists a finite surface patch $\mathcal{S}$, such that all points on the surface of Ξ have approximately the same distance to surface $\mathcal{S}$.

For an implicit surface $\mathcal{S} = Z(f)$ defined by function f, it is easy to construct a thin solid by formula $\Xi = g_{\setminus}(\mathcal{S}, \mathcal{S} + d)$, where d is a positive constant. For example, Figure 4.3 presents a simple thin solid based on the implicit object in Figure 2.6.

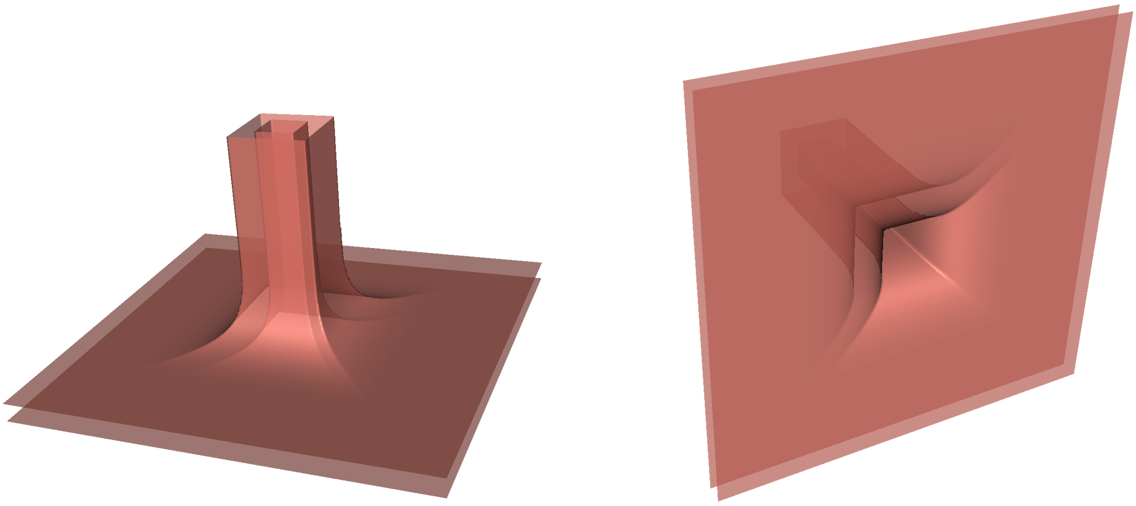

(a) (b)

Figure 4.3: A Simple Thin Solid

However, the thin solid constructed in this way is not thin implicit patch described in Definition 4.1 , since the thickness of the thin solid is neither uniform nor controllable. Figure 4.4 demonstrates this non-uniformity. Thin solid in Figure 4.4(a) is based on implicit function $f(x, y, z) = g_{\cup 2,0.9}(\frac{1}{4}x^2 + 4y^2 + z^2 - 1, 4x^2 + \frac{1}{4}y^2 + z^2 - 1)$ and formula $\Xi = g_{\setminus}(Z(f), Z(f) + 0.2)$ chopped by the implicit plane $f(x, y, z) = z$. As can been seen directly, the thickness is non-uniform. Figure 4.4(b) shows its intersecting surface on unit plane z.

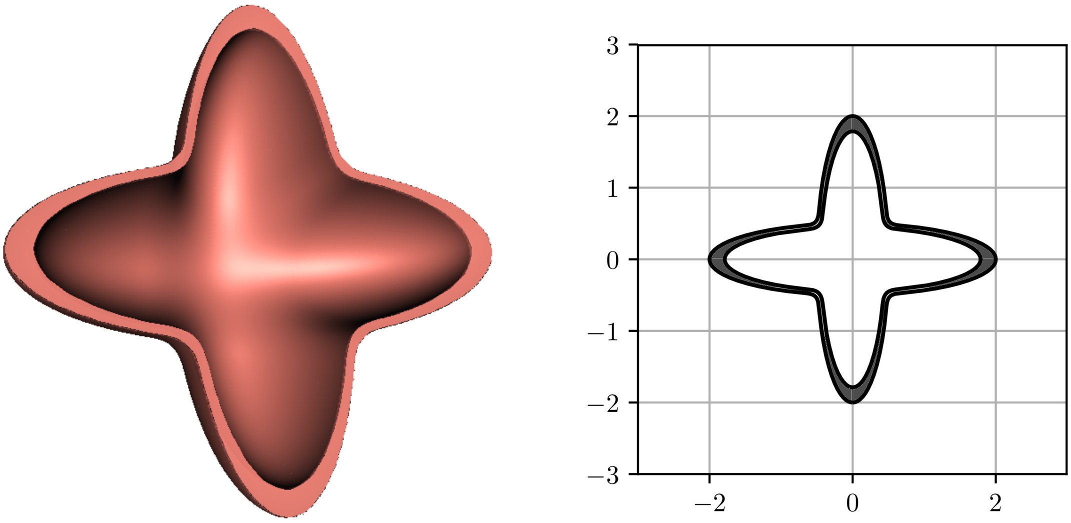

(a) A 3D Object (b) An Intersecting Plane of the Object

Figure 4.4: Thin Implicit Solid with Non-uniform Thickness

The object in Figure 4.5 is converted from the Clebsch Cubic Surface with the formula $\Xi = g_\cap(g_\setminus(\mathcal{S}, \mathcal{S}+100), f)$, where $\mathcal{S}$ is the Clebsch Cubic Surface defined by Equation 2.6. The thin solid in Figure 4.6 is converted from a Bézier surface patch using formula $\Xi = g_\setminus(\mathcal{S}, \mathcal{S}+100)$, where $\mathcal{S}$ is the implicit surface of the Bézier patch. The non-uniform thickness of the two objects can be directly observed. This non-uniformity is due to the same reason explained in the previous example. Here, the constant value $d = 100$ has no geometric meaning.

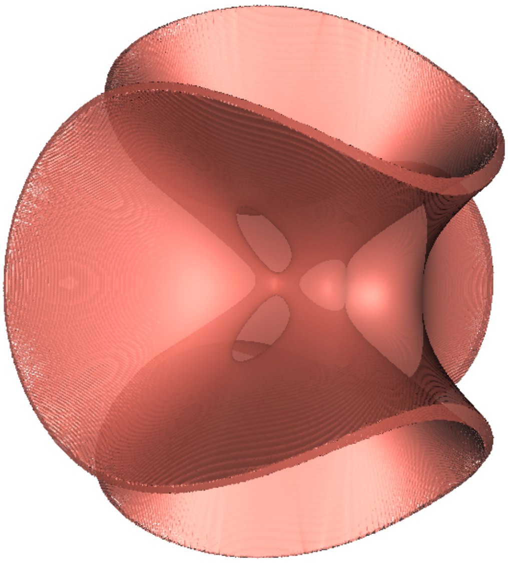

Figure 4.5: Thin Implicit Solid of Clebsch Surface with Non-uniform Thickness

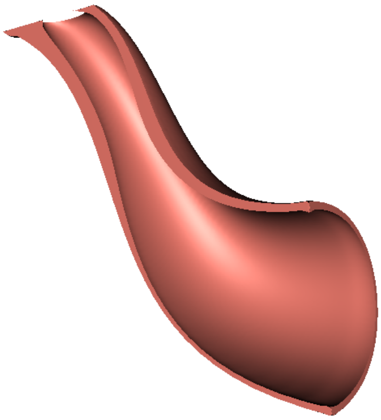

Figure 4.6: Thin Implicit Solid of Bézier Surface with Non-uniform Thickness

Although these objects are easy to construct, they are not thin implicit patch according to Definition 4.1 , since the thickness is non-uniform. In order to control the thickness of a thin implicit patch such that the corresponding geometric object approximately satisfies the condition described in Definition 4.1 , implicit offset surface is proposed to define uniform thin implicit patch.

4.2.1 Implicit Offset Surface

A thin solid converted from a surface has two surfaces. The two surfaces are offset surfaces of the original surface. Mathematically, an offset surface $\bar{\bar{\mathcal{S}}}$ of a given surface $\mathcal{S}$ is a surface reconstructed from surface $\mathcal{S}$ such that the distance from any point on the surface $\bar{\bar{\mathcal{S}}}$ to $\mathcal{S}$ is constant. The surface $\mathcal{S}$, from which an offset surface is generated, is often referred to as the generator surface. Generally, it is difficult to find out an exact offset surface for a given surface $\mathcal{S}$ if $\mathcal{S}$ is parametrically represented. This is because finding the offset surface often involves an optimisation process which can be very challenging if the given parametric surface has a complex shape. In addition, the offset surface may self-intersect and may not be able to give a geometrically meaningful result. Complex additional operations are often needed to solve this problem (Maekawa 1999).

In this research, an algorithm for finding the offset surface is proposed by using implicit functions. With the proposed technique, the non-implicit surfaces are firstly converted into implicit surfaces by implicit modelling techniques. As is shown later, it is much easier to acquire an offset surface from an implicitly represented surface.

Definition 4.2 (Implicit Offset Surface)**.** An Implicit Offset Surface (IOS) is an implicit surface reconstructed from a given surface representation such that the reconstructed implicit surface has a constant distance to the given surface.

In general, two implicit offset distance functions can be generated by extruding the given surface along and against the surface normal. The distance between the two different implicit offset surfaces is always a constant, therefore the subtraction blending of the two implicit offset surfaces always gives a uniform-thickness solid. Thus, a thin implicit patch can be defined with two implicit offset surfaces.

Definition 4.3 (Thin Implicit Patch)**.** A *Thin Implicit Patch (TIP)* Ξ is the implicit surface obtained by blending two implicit offset surfaces from a given surface $\mathcal{S}$:

$$\Xi = \bar{\bar{\mathcal{S}}}_{d_0} \backslash \bar{\bar{\mathcal{S}}}_{d_1} \tag{4.1}$$

where $\bar{\bar{\mathcal{S}}}_{d_0}$ and $\bar{\bar{\mathcal{S}}}_{d_1}$ are implicit offset surfaces of $\mathcal{S}$, $d_0 < d_1$ are two constants. The thickness value of thin implicit patch Ξ is $d = d_1 - d_0$.

Based on the representation of the generator surface, a thin implicit patch and its implicit offset surfaces can be constructed from dual-layer reconstruction, approximate distance or morphological implicits.

4.2.2 TIP as Dual-layer Reconstruction

If the generator surface is a parametric surface, then accurate sampling points can be extract to generate implicit offset surfaces.

Here, an approximate method fro converting an explicit geometric surface, such as a parametric surface, is proposed by fitting an implicit surface to a set of points sampled from the surface. More specifically, an implicit offset surface $\bar{\bar{\mathcal{S}}}_d = Z(\bar{\bar{f}})$ with distance d to a surface object $\mathcal{S} = Z(f)$ can be approximately built by sampling n distinct points $\{\mathbf{P}_i\}_{i=1}^{n} \in \mathcal{S}$, such that $\bar{\bar{f}}(\mathbf{P}_i + d\mathbf{N}_i) = 0$, where $\mathbf{N}_i = \frac{\nabla f(\mathbf{P}_i)}{|\nabla f(\mathbf{P}_i)|}$, $i = 1, 2, \ldots, n$.

In the above description, $\mathcal{S} = Z(f)$ is the implicit surface converted from the generator parametric surface, which can be regarded as an implicit offset surface with a distance $d = 0$ to the generator surface.

The thin implicit patch constructed in this way is a blending of a dual-layer reconstruction. This section illustrates this construction technique with the implicit reconstruction of the legendary Utah teapot.

Utah Teapot

The Utah teapot is a classical parametric geometry constructed with Bézier surfaces (Prautzsch et al. 2002).

A Bézier curve is a parametric curve. The curve passes its end control points and its shape is controlled by other control points. An n-degree Bézier curve can be defined using Bernstein polynomial with $n+1$ control points $\mathbf{P}_0, \mathbf{P}_1, \mathbf{P}_2, \ldots, \mathbf{P}_n$ as:

$$\mathcal{C}(t) = \sum_{i=0}^{n} \mathbf{P}_i B_{i,n}(t) \tag{4.2}$$

where

$$B_{i,n}(t) = C_n^i t^i (1-t)^{n-i}, \ i = 0, 1, 2, \ldots, n \tag{4.3}$$

Bézier curve can also be presented in matrix form. For instance, the cubic Bézier curve can be rewritten in the following way:

$$\mathcal{C}(t) = [1, t, t^2, t^3] \begin{bmatrix} 1 & 0 & 0 & 0 \\ -3 & 3 & 0 & 0 \\ 3 & -6 & 3 & 0 \\ -1 & 3 & -3 & 1 \end{bmatrix} \begin{bmatrix} \mathbf{P}_0 \\ \mathbf{P}_1 \\ \mathbf{P}_2 \\ \mathbf{P}_3 \end{bmatrix} \tag{4.4}$$

A Bézier surface can be defined to have different orders, depending on the size of control points used. A Bézier patch defined by $(n+1)(m+1)$ control points can be expressed in the following form:

$$\mathcal{S}(u, v) = \sum_{i=0}^{n} \sum_{j=0}^{m} \mathbf{P}_{i,j} B_{i,n}(u) B_{j,m}(v) \tag{4.5}$$

For example, a bicubic Bézier patch in matrix form can be expressed in the following form:

$$\mathcal{S}(u, v) = \mathbf{U} \cdot \mathbf{M} \cdot \mathbf{P} \cdot \mathbf{M}^T \cdot \mathbf{V}^T \tag{4.6}$$

where

$$\mathbf{U} = [1, u, u^2, u^3] \qquad \mathbf{V} = [1, v, v^2, v^3]$$

$$\mathbf{M} = \begin{bmatrix} 1 & 0 & 0 & 0 \\ -3 & 3 & 0 & 0 \\ 3 & -6 & 3 & 0 \\ -1 & 3 & -3 & 1 \end{bmatrix} \qquad \mathbf{P} = \begin{bmatrix} \mathbf{P}_{00} & \mathbf{P}_{01} & \mathbf{P}_{02} & \mathbf{P}_{03} \\ \mathbf{P}_{10} & \mathbf{P}_{11} & \mathbf{P}_{12} & \mathbf{P}_{13} \\ \mathbf{P}_{20} & \mathbf{P}_{21} & \mathbf{P}_{22} & \mathbf{P}_{23} \\ \mathbf{P}_{30} & \mathbf{P}_{31} & \mathbf{P}_{32} & \mathbf{P}_{33} \end{bmatrix}$$

The classic Utah teapot consists of 32 cubic Bézier patches. Figure 4.7 presents one of these parametric patches corresponding to a half of the teapot spout, where the 16 control points are shown as follows:

$$\begin{bmatrix} \mathbf{P}_{00} \\ \mathbf{P}_{01} \\ \mathbf{P}_{02} \\ \mathbf{P}_{03} \\ \mathbf{P}_{10} \\ \mathbf{P}_{11} \\ \mathbf{P}_{12} \\ \mathbf{P}_{13} \\ \mathbf{P}_{20} \\ \mathbf{P}_{21} \\ \mathbf{P}_{22} \\ \mathbf{P}_{23} \\ \mathbf{P}_{30} \\ \mathbf{P}_{31} \\ \mathbf{P}_{32} \\ \mathbf{P}_{33} \end{bmatrix} = \begin{bmatrix} 1.700 & 0.000 & 1.425 \\ 1.700 & -0.660 & 1.425 \\ 1.700 & -0.660 & 0.600 \\ 1.700 & 0.000 & 0.600 \\ 2.600 & 0.000 & 1.425 \\ 2.600 & -0.660 & 1.425 \\ 3.100 & -0.660 & 0.825 \\ 3.100 & 0.000 & 0.825 \\ 2.300 & 0.000 & 2.100 \\ 2.300 & -0.250 & 2.100 \\ 2.400 & -0.250 & 2.025 \\ 2.400 & 0.000 & 2.025 \\ 2.700 & 0.000 & 2.400 \\ 2.700 & -0.250 & 2.400 \\ 3.300 & -0.250 & 2.400 \\ 3.300 & 0.000 & 2.400 \end{bmatrix} \times 100 \tag{4.7}$$

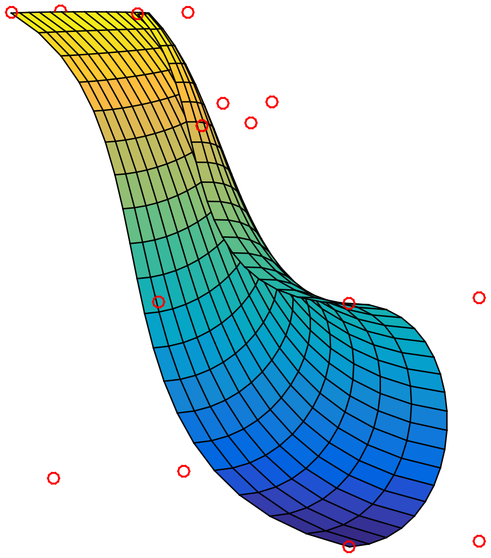

Figure 4.7: A Bézier Patch of Utah Teapot

With Equation 4.6, a collection of accurate sampling points $\mathcal{P} = \{\mathbf{P}_i\}_{i=1}^{n}$ can be directly extracted. These points are used to generate implicit offset surfaces of $\mathcal{S}(u, v)$. The coefficients $\boldsymbol{\gamma}$ and $\boldsymbol{\beta}$ of Equation 3.6 based on the 16 control points of Equation 4.7 are $\boldsymbol{\gamma} = [2.17210, -3.57079 \times 10^1, 1.92390 \times 10^1, 7.21065, 1.20099 \times 10^{-1}, -2.29573 \times 10^1, 1.06950 \times 10^1, 2.70430, 4.51216 \times 10^{-1}, 1.28569 \times 10^1, -2.48906 \times 10^1, 5.25909, 7.82499, 8.59436, -1.58211 \times 10^1, 9.35959]$ and $\boldsymbol{\beta} = [2.25205 \times 10^4, 3.51007 \times 10^1, -2.70181 \times 10^1, -9.38856 \times 10^1, -6.26586 \times 10^{-2}, -2.03431 \times 10^{-2}, -1.11525 \times 10^{-1}, 8.04324 \times 10^{-1}, 3.92215 \times 10^{-1}, 4.27144 \times 10^{-1}]$, where the $\boldsymbol{\beta}$ are the 10 coefficients of an ellipsoid.

Utah Teapot with TIP

After a point cloud $\mathcal{P} = \{\mathbf{P}_i\}_{i=1}^{n}$ has been sampled from a Bézier surface patch used for modeling the Utah teapot, the patch can be approximately converted into a thin implicit patch.

Figure 4.8 illustrates this conversion process. Sampling points are firstly extracted and fitted into an implicit surface in Figure 4.8(a). RBF fitting with ellipsoid constraint is then used to give a rounded boundary result. The unwanted rounded redundancy comes from the ellipsoid constraint and has been trimmed to a correct shape showing in Figure 4.8(b). The trimming planes come from the control points of the Bézier patch. In Figure 4.8(c), the prospective half spout is represented as thin implicit patch in formula $\Xi = g_{\setminus}(\mathcal{S}_{-1}, \mathcal{S}_1)$, where $\mathcal{S}$ is the implicit surface in Figure 4.8(b). Compared with the object in Figure 4.6, the thickness d has clear geometric meaning.

This construction can be flexible. For instance, let $\mathcal{Q}_0 = \mathcal{P} - d_0\mathcal{N}$ and $\mathcal{Q}_1 = \mathcal{P} + d_1\mathcal{N}$, a uniform thin implicit patch with thickness $(d_0 + d_1)$ is given by $\Xi = g_{\setminus}(\mathcal{S}_{-d_0}, \mathcal{S}_{d_1})$, where $\mathcal{S}_{-d_0}$ and $\mathcal{S}_{d_1}$ are implicit offset surfaces fitted from $\mathcal{Q}_0$ and $\mathcal{Q}_1$ respectively.

4.2.3 TIP as Approximate Distance

The thickness d of a thin implicit patch Ξ can be regarded as the approximate distance of the generator surface $\mathcal{S}$.

The Euclidean Distance to Geometric Objects

The Euclidean distance to a geometric object can be represented as the distance function. A distance function is an implicit function precisely gives the Euclidean distance from a point in space to the surface of a geometric object (Osher et al. 2006).

Definition 4.4 (Distance Function)**.** Let $\partial\Omega$ be a surface, a *Distance Function* of $\partial\Omega$ is defined as follows (ibid.):

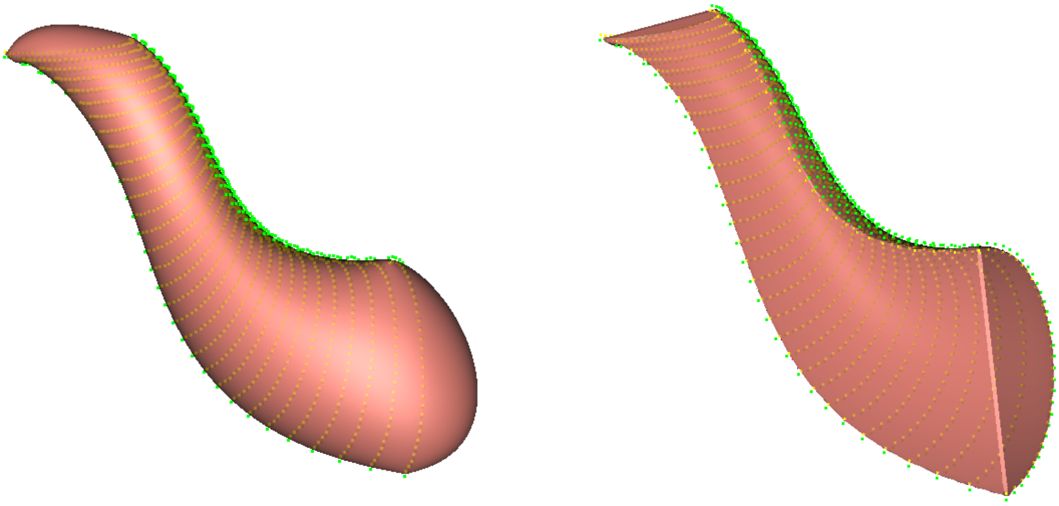

(a) Implicit Object of Bézier Patch

(b) Trimmed Implicit Object of Bézier Patch

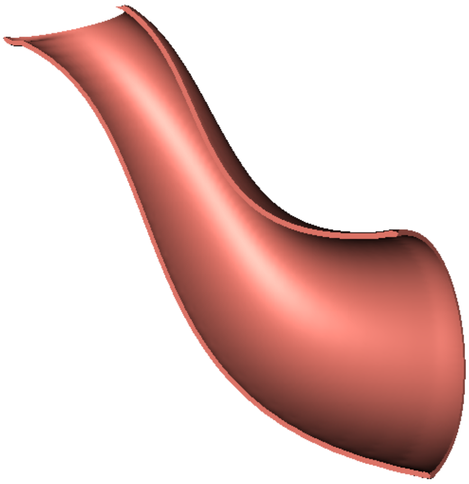

(c) Thin Implicit Patch of Bézier Patch

Figure 4.8: Parametric Surface to Thin Implicit Patch

$$d(\mathbf{X}) = \min_{\mathbf{X}_I \in \partial\Omega} (\|\mathbf{X} - \mathbf{X}_I\|) \tag{4.8}$$

where $\| \bullet \|$ is the Euclidean length of a vector.

A distinct property of distance function is $\|\nabla d\| \equiv 1$, since d is a Euclidean distance. Besides, the distance function implies that $\mathbf{X} \in \partial\Omega$ when $d(\mathbf{X}) = 0$.

A Signed Distance Function (SDF) is an implicit function defined with $\|\phi(\mathbf{X})\| = d(\mathbf{X})$ for all $\mathbf{X}$ (Osher et al. 2006). More specifically:

$$\phi(\mathbf{X}) = \begin{cases} -d(\mathbf{X}) & \text{for} \quad \mathbf{X} \in \Omega^- \\ 0 & \text{for} \quad \mathbf{X} \in \partial\Omega \\ d(\mathbf{X}) & \text{for} \quad \mathbf{X} \in \Omega^+ \end{cases} \tag{4.9}$$

The same shape can be represented by either normal implicit function or signed distance function. For example, a 2D unit sphere can be represented as the 0 level set of $f(\mathbf{X}) = x^2 + y^2 - 1$ as a normal implicit function, or $\phi(\mathbf{X}) = \sqrt{x^2 + y^2} - 1$ as an SDF. But the later one has property $\|\nabla\phi\| = 1$ when $\mathbf{X} \neq 0$ such that the level sets with same steps give evenly changed concentric circles. Figure 4.9 shows this difference. Level set $0, 0.2, 0.4, \ldots$ are displayed. The evenly changed isocontours can be observed from Figure 4.9(b).

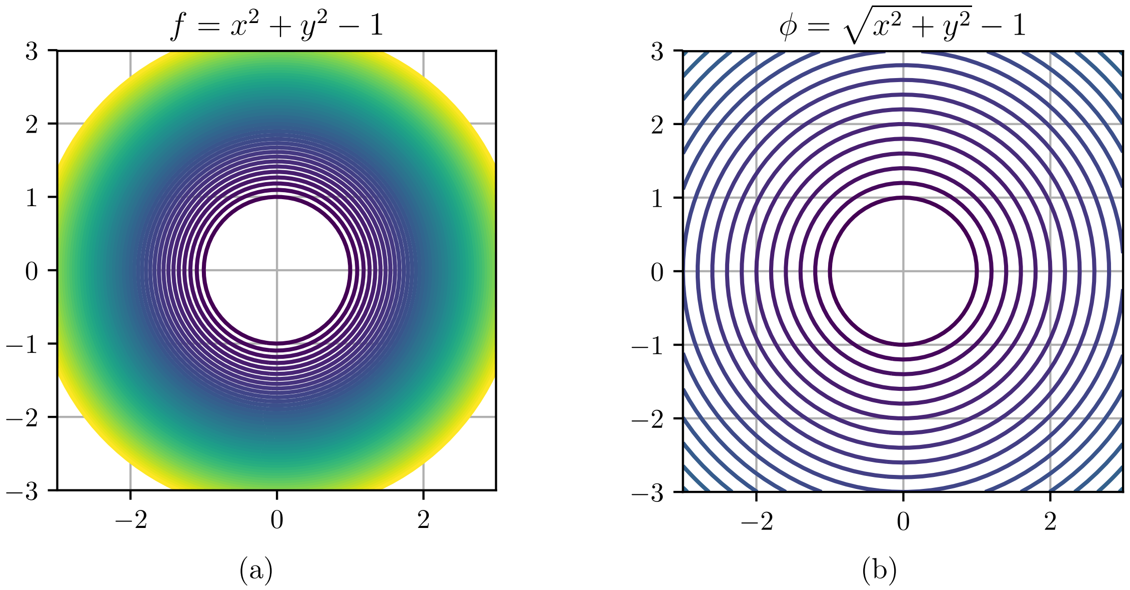

(a) (b)

Figure 4.9: Comparison between Implicit Function and SDF

The Signed Distance Function can be used to construct skeletal surfaces based on simple geometries (Bloomenthal 1990). For example, in 3D space the shape of the SDF of a point is a sphere, a line segment will give a capsule, and a Bézier curve produces a curvy tube. Complex geometries can be generated from simple skeletons in this way. However, it is heavy to compute an SDF and there is no closed-form solution when the degree of the skeletal expression is greater than 2. For instance, a cubic Bézier curve has no closed-form signed distance function, as it has to solve a quintic function. Numerical solutions is used to approximate the result in this circumstance.

Approximate Distance

As discussed before, the gradient of a distance function keeps a constant value. If the underlying implicit function of an implicit solid is a distance function, formula $\Xi = g_{\setminus}(\mathcal{S}, \mathcal{S} + d)$ will give a thin implicit patch with uniform thickness d. Although an implicit function is not necessarily to be a distance function, the value of the generalised normal $\mathbf{N} = \frac{\nabla f}{|\nabla f|}$ remains to 1. When distance d is small, the value of this generalised normal is a good approximation of d (Taubin 1988, 1991).

Definition 4.5 (Approximate Distance)**.** Let $f : \mathbb{R}^3 \to \mathbb{R}$ be an implicit function, $\mathbf{P} \in \mathbb{R}^3$ be a regular point, $Z(f) = \{\mathbf{X} \in \mathbb{R}^3 : f(\mathbf{X}) = 0\}$. The *Approximate Distance* from $\mathbf{P}$ to $Z(f)$ is an algebraic distance (Taubin 1991):

$$\tilde{d}(\mathbf{P}, Z(f)) \approx \frac{|f(\mathbf{P})|}{|\nabla f(\mathbf{P})|} \tag{4.10}$$

The approximate distance can be explained by the Taylor decomposition. For any $\mathbf{P} \in \mathbb{R}^3$, let $\mathbf{Q} \in Z(f)$ be the nearest point from $\mathbf{P}$ to $Z(f)$ such that $\mathbf{Q} = \mathbf{P} - \boldsymbol{\varepsilon}$, where $\boldsymbol{\varepsilon}$ is the vector from $\mathbf{Q}$ to $\mathbf{P}$, then $f(\mathbf{Q}) = f(\mathbf{P} - \boldsymbol{\varepsilon}) = 0$. With the Taylor decomposition, $f(\mathbf{P} - \boldsymbol{\varepsilon}) = f(\mathbf{P}) - \nabla f(\mathbf{P}) \cdot \boldsymbol{\varepsilon} + o(|\boldsymbol{\varepsilon}|^2) = 0$, where the dot $(\cdot)$ is the dot product. Since $f(\mathbf{Q}) = 0$, when $|\boldsymbol{\varepsilon}|$ is small enough, $f(\mathbf{P}) - \nabla f(\mathbf{P}) \cdot \boldsymbol{\varepsilon} \approx 0$. Let $\tilde{d}$ be the distance from $\mathbf{P}$ to the surface $Z(f)$, then $\boldsymbol{\varepsilon} = \tilde{d} \frac{\nabla f(\mathbf{P})}{|\nabla f(\mathbf{P})|}$. Thus $\tilde{d} \approx \frac{|f(\mathbf{P})|}{|\nabla f(\mathbf{P})|}$.

When the gradient ∇f does not analytically exist, numerical techniques, such as the finite difference, can be used to calculate the gradient of a given implicit function.

Let $f = f(x, y, z)$ be an implicit function, its first-order central difference on the x direction is:

$$D_x^o f := \frac{\partial f}{\partial x} \approx \frac{f_{i+1} - f_{i-1}}{2\Delta x} \tag{4.11}$$

where Δx is the unit step on x direction of Cartesian grid, f_i is the function value at the i-th grid.

The formulas of y and z directions can be obtained similarly, and the gradient of f can be numerically represented as:

$$\nabla f = \left[\frac{\partial f}{\partial x}, \frac{\partial f}{\partial y}, \frac{\partial f}{\partial z}\right] \approx [D_x^o f, D_y^o f, D_z^o f] \tag{4.12}$$

When $\|\nabla f\| = 0$, the average gradient is estimated from the neighbours of the current position for evaluation.

Figure 4.10 demonstrates the approximate distances of implicit function $f(x, y) = (0.8x^2 - 1)^2 + 2y^2 - 1.2$. Contours of level sets $0.0, 0.1, 0.2, 0.3$ and 0.4 are shown. The smaller the value of the level set, the better the approximate distance is preserved.

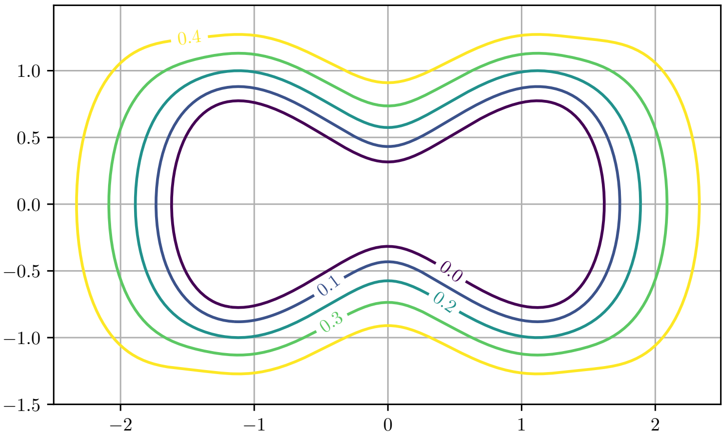

Figure 4.10: Approximate Distance

Distance Function with TIP

The approximate distance illustrates that an implicit function can be regarded as a distance function when the distance value is small. Both the implicit offset surface and thin implicit patch can then be redefined with distance function.

Definition 4.6 (Implicit Offset Surface)**.** An *Implicit Offset Surface* of an implicit surface $\mathcal{S} = Z(f)$ is $\bar{\bar{\mathcal{S}}}_d = Z(\tilde{d}) + d$, where $\tilde{d}$ is the approximate distance of f, d is a small constant.

Definition 4.7 (Thin Implicit Patch)**.** A *Thin Implicit Patch (TIP)* Ξ is the implicit blending of two implicit offset surfaces from surface $\mathcal{S}$:

$$\Xi = \bar{\bar{\mathcal{S}}}_{d_0} \backslash \bar{\bar{\mathcal{S}}}_{d_1} = g_{\backslash}(Z(\tilde{d}) + d_0, Z(\tilde{d}) + d_1) \tag{4.13}$$

where $d_0 < d_1$ are two small constants.

Figure 4.11 gives an example of this thin implicit patch. The thin patch in the figure is based on formula $\Xi = g_{\backslash}(Z(\tilde{d}), Z(\tilde{d}) + 0.2)$, where $\tilde{d} = \frac{f}{|\nabla f|}$ and $f = g_{\cup_{2,0.9}}(\frac{1}{4}x^2 + 4y^2 + z^2 - 1, 4x^2 + \frac{1}{4}y^2 + z^2 - 1)$. Compared with Figure 4.4, the thin implicit patch gains a uniform thickness. The object in Figure 4.11(c) and Figure 4.11(d) are a same object converted from the Clebsch Cubic Surface with the formula $\Xi = g_\cap(g_\setminus(\mathcal{S}, \mathcal{S}+0.1), f)$, where $\mathcal{S}$ is the Clebsch Cubic Surface defined by Equation 2.6, $f(x, y, z) = x^2 + y^2 + z^2 - 4$. In Figure 4.11(c), it is rendered in a translucent colour to see the thickness of each part. Compared with Figure 4.5, the thickness is uniform.

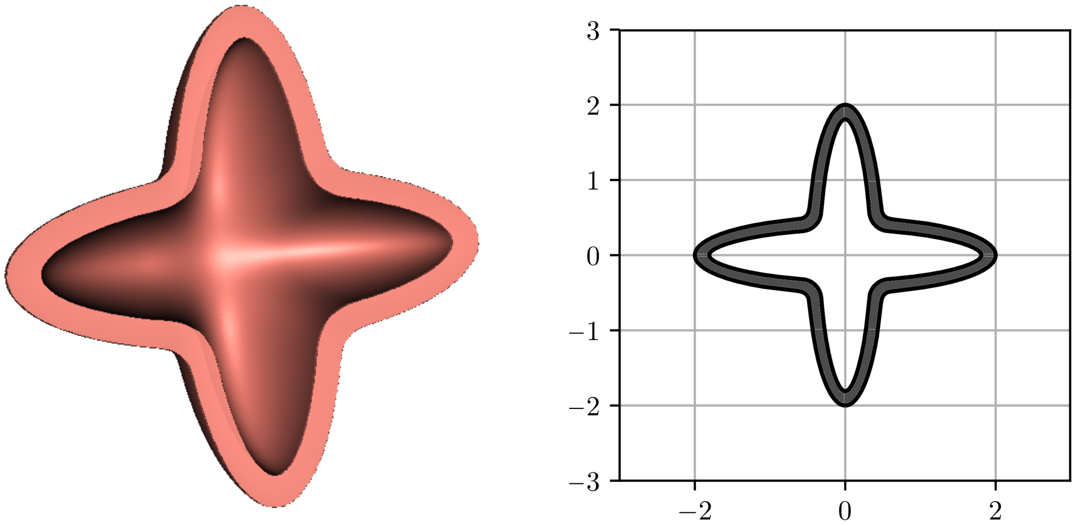

(a) Thin Implicit Patch (b) 2D Thin Implicit Patch

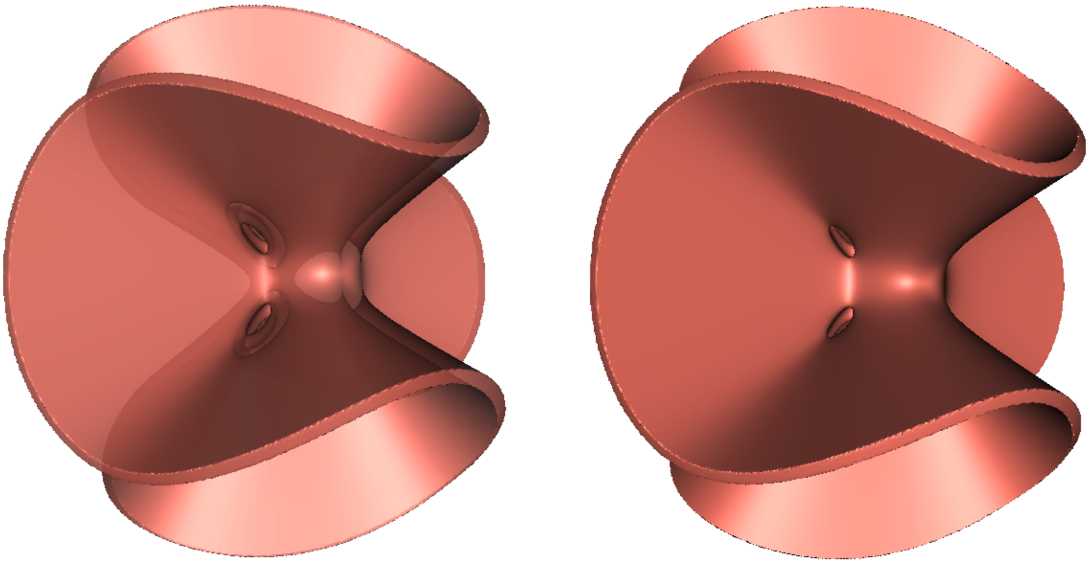

(c) TIP of Clebsch Surface (d) TIP of Clebsch Surface

Figure 4.11: Thin Implicit Patch with Approximated Distance

The underlying implicit function can be more complex. Figure 4.12 gives the thin-patched Utah teapot spout with formula $\Xi = g_\setminus(Z(\tilde{d}), Z(\tilde{d})+2)$, where $\tilde{d} = \frac{f}{|\nabla f|}$ and f is the implicit function reconstructed from point cloud sampled from parametric surface in Figure 4.7. Compared with the dual-reconstructed spout in Figure 4.8(c), this spout has the same shape but requires only one implicit reconstruction.

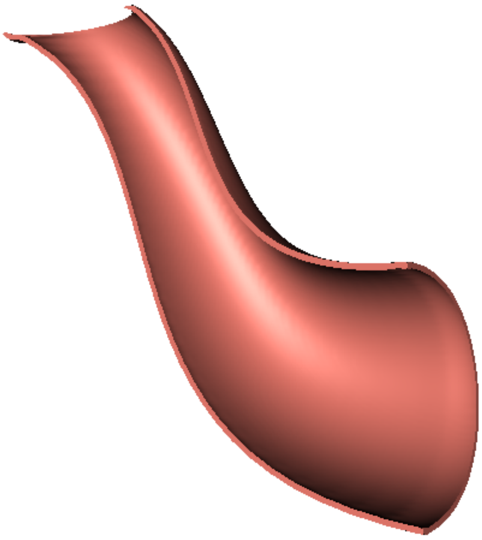

Figure 4.12: Thin Implicit Spout with Approximated Distance

4.2.4 TIP as Morphological Implicits

Uniform thin implicit patch can also be constructed as morphological implicits.

Mathematical morphology is a technique to analyse and process geometrical structures based on set theory (Haralick et al. 1987). The two basic operations of mathematical morphology is dilation and erosion. For binary image A and structuring element B, dilation is defined as $A \oplus B = \{x \mid B_x \cap A \neq \varnothing\}$, and erosion is defined as $A \ominus B = \{x \mid B_x \subseteq A\}$, where $B_x = \{x + b \mid b \in B\}$. Dilation gives thicken effect and erosion gives narrowing effect on images. Dilation and erosion are also known as Minkowski sum and difference (Lien 2010; Schneider 1993; Varadhan et al. 2006).

Definition 4.8 (Morphological Implicits)**.** Let $\mathcal{O} = \{\mathbf{X} \in \mathbb{R}^3, \alpha \in \mathbb{R} : f(\mathbf{X}) \leqslant \alpha\}$ be an implicit solid, $\mathcal{B} = \{\mathbf{X} \in \mathbb{R}^3, \tau \in \mathbb{R}^+ : \|f(\mathbf{X})\| \leqslant \tau\}$ be an implicit solid sphere with radius τ. *Morphological Implicits* are dilation and erosion results between $\mathcal{O}$ and $\mathcal{B}$:

$$\begin{cases} \mathcal{O} \oplus \mathcal{B} & = & \{\mathbf{X} \mid \mathcal{B}_{\mathbf{X}} \cap \mathcal{O} \neq \varnothing\} \\ \mathcal{O} \ominus \mathcal{B} & = & \{\mathbf{X} \mid \mathcal{B}_{\mathbf{X}} \subseteq \mathcal{O}\} \end{cases} \tag{4.14}$$

where $\mathcal{B}_{\mathbf{X}} = \{\mathbf{X} + \mathbf{b} \mid \mathbf{b} \in \mathcal{B}\}$ is the translation of structuring element $\mathcal{B}$ with $\mathbf{X}$.

Figure 4.13 and Figure 4.14 show the morphological dilation and erosion of function $f = g_{\cup_{2,0.9}}(\frac{1}{4}x^2+4y^2-1, 4x^2+\frac{1}{4}y^2-1)$ and structure element $\mathcal{B} = \sqrt{x^2+y^2}-0.1$. Sub-figures (a) show the 0 level set of f, and (b) show the morphological results in dashed lines together with the original shapes in solid lines. The morphological implicit is an implicit offset surface of the original shape.

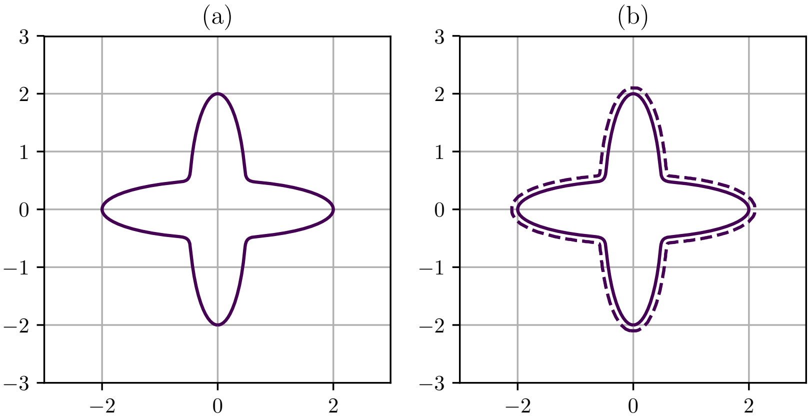

Figure 4.13: Implicit Dilation

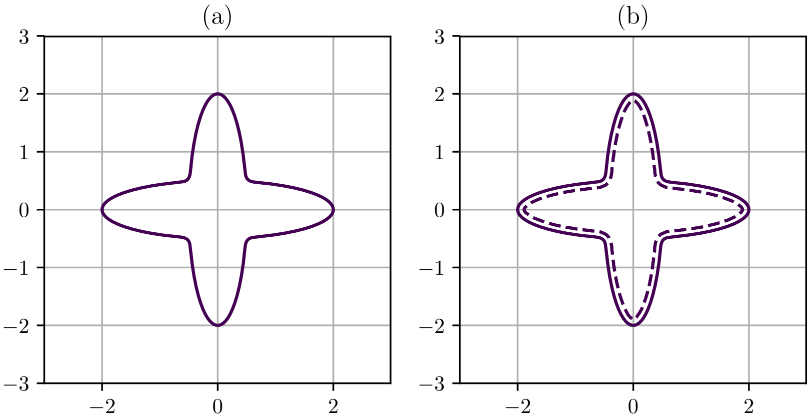

Figure 4.14: Implicit Erosion

With morphological implicits, outward and inward uniform thin implicit patches are defined as:

$$\begin{cases} \Xi_\tau^+ &= g_{\setminus}(\mathcal{O}, \mathcal{O} \oplus \mathcal{B}) \\ \Xi_\tau^- &= g_{\setminus}(\mathcal{O} \ominus \mathcal{B}, \mathcal{O}) \end{cases} \tag{4.15}$$

Figure 4.15 and Figure 4.16 present the outward and inward uniform thin implicit patches. Compared with the thin implicit patch generated with approximate distance in Figure 4.11, these two results give sharp corners when the original shape has negative curvatures, which should be avoided. Although morphological implicits can be used on any implicit objects, the computation is quite heavy especially in 3D conditions.

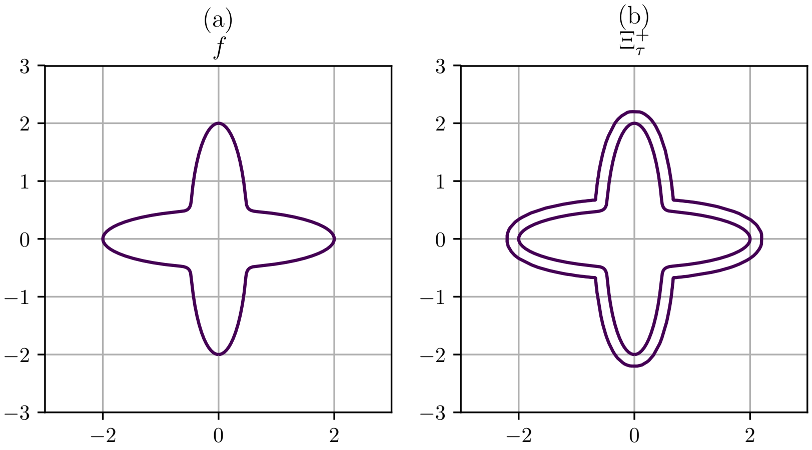

Figure 4.15: 2D Outward Thin Implicit Patch

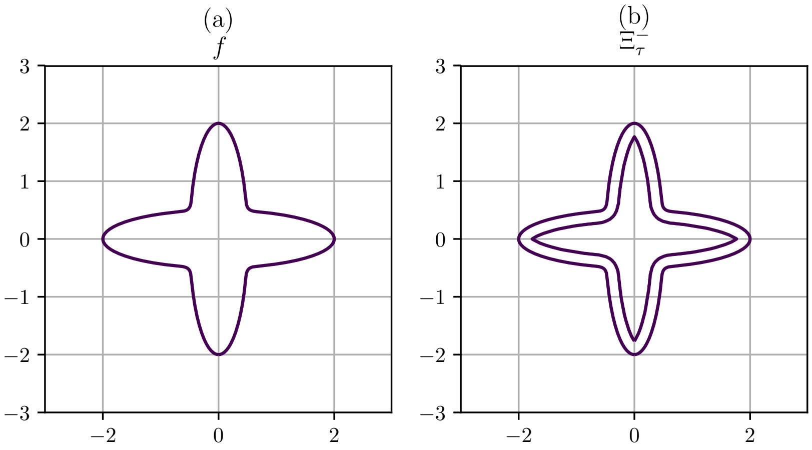

Figure 4.16: 2D Inward Thin Implicit Patch

4.3 Implicit Interior Structures

Converting a surface-based object into a thin-patched object has a direct application on additive manufacturing. With the proposed technique, a visible surface can be converted to be a printable thin solid. Though it is relatively a simple task to convert a surface into a thin solid, this thin solid does not contain any interior structures and cannot correctly represent a real-world object. For example, the vascular wall shown in Figure 4.1 has multi-layered structures and should not be simply considered as a thin-patched surface.

With the traditional parametric surface based Computer-aided Design (CAD) techniques, it is very difficult to design and model complicated biological tissue structures and embed them inside a geometric object, since explicitly represented geometric objects are difficult to blend. In contrast, the thin implicit patch is represented as implicit functions such that implicit blending operations can be used to embed the interior structures inside the patch. The implicit represented interior structures are called Implicit Interior Structures (IIS) in this research.

It is a challenging task to geometrically represent the interior vascular structures because of their high irregularity and complexity. These kind of structures are usually regarded as porous structures (Liu et al. 2014; Scheffler et al. 2006). A porous structure can either be reconstructed from real-world porous object or be designed as an artifact. For the real-world porous object, its existing structure is required to be attained in advance. But in many cases, such as the vascular wall of a medical image, the interior structures of the vascular wall cannot be acquired yet. For an artifact design, a porous structure can be either regular-shaped pores or irregular-shaped pores. Regular porous structures are easier to design but are not natural and realistic. Irregular porous structures are favoured as the representation of a real-world object but require flexible control of the irregularity and intricacy (Hollister et al. 1992; Kou et al. 2010).

This section shows how to design and model both regular and irregular porous structures using implicit functions and how to embed them into the thin implicit patch as implicit interior structures.

4.3.1 Implicit Porous Structures

Porous structures are 3D solid structures with interconnected pores (Chow et al. 2007). In geometric modelling, porous structures are usually designed based on models (Coutelieris et al. 2012). For example, the lattice model packs unit cells into regular patterns to form regular-shaped porous structures (Gibson et al. 2014; Hollister et al. 2002); the stochastic model generates cells with stochastic processes to form the regular pattern (Schroeder et al. 2005a). The voronoi model uses voronoi cell to aggregate high-degree irregular porous structures (Kou et al. 2010).

Porous structures can be represented as implicit functions. The porous geometric structures defined using are called implicit porous structures.

Definition 4.9 (Implicit Porous Structure)**.** An implicit object $\aleph$ of a field function $f(\mathbf{X})$ is said to be an *Implicit Porous Structure* if $\aleph = Z(f)$ is a porous structure, where $Z(f)$ is the 0 level set of f.

The shapes of implicit porous structures are various. Both regular-shaped and irregular-shaped porous structures can be easily generated by implicit functions. Figure 4.17 gives several examples of implicit porous structures.

Regular boxes are given in Figure 4.17(a). The lattice structure is generated with the implicit function $f(x, y, z) = \text{sign}(\sin(\frac{1}{2}x)) + \text{sign}(\sin(\frac{1}{2}y)) + \text{sign}(\sin(\frac{1}{2}z)) + \frac{1}{2} = 0$. They are rendered in translucent colour to make their inner structures visible.

The object in Figure 4.17(b) is a regular-shaped ellipsoidal porous structure generated by the implicit function $f(x, y, x) = \cos(2x)\sin(3y)\cos(4z) - \frac{1}{2} = 0$. The structure looks like many ellipsoids.

In Figure 4.17(c), a pseudo irregular-shaped porous structure is given by the implicit function $f(x, y, z) = 2 - \cos(2x + \pi y) - \cos(2x - \pi y) - \cos(2y + \pi z) - \cos(2y - \pi z) - \cos(2z - \pi x) - \cos(2z + \pi x) = 0$. The geometry of this implicit porous structure is complex and can be regarded as an irregular-shaped structure.

Fox example, Figure 4.18 shows the subtraction blending result between the TIP of Clebsch Surface in Figure 4.11(d) and an implicit porous structure. The function of the porous structure is $f(x, y, x) = \cos(4x)\sin(6y)\cos(8z) - \frac{1}{2} = 0$.

Since implicit functions can be blended together easily, the implicit porous structures can be designed with a variety of ways (Li et al. 2018). However, no matter how complex the shape of the structure is, it can always be easily embedded into existing implicit objects. This research focuses on how to embedded the implicit porous structures into the thin implicit patches.

4.3.2 TIP with Inner Structures

Thin solids with interior structures are widely existed in the real world. As shown in Figure 4.19, both the skin and the leaf have multiple layers with different cells, and a vascular wall consists of many different tissues. All these structures can be regarded as implicit porous structures inside a thin implicit patch.

The basic idea of the embedment of an implicit porous structure inside a thin implicit patch is a trimming operation of the structure such that it has a similar shape but is thinner than the patch.

Let $\bar{\bar{\mathcal{S}}}_{d_0}, \bar{\bar{\mathcal{S}}}_{d_1}, \bar{\bar{\mathcal{S}}}_{d_2}$ and $\bar{\bar{\mathcal{S}}}_{d_3}$ be four implicit offset surfaces of $\mathcal{S}$, where $d_0 < d_1 <$

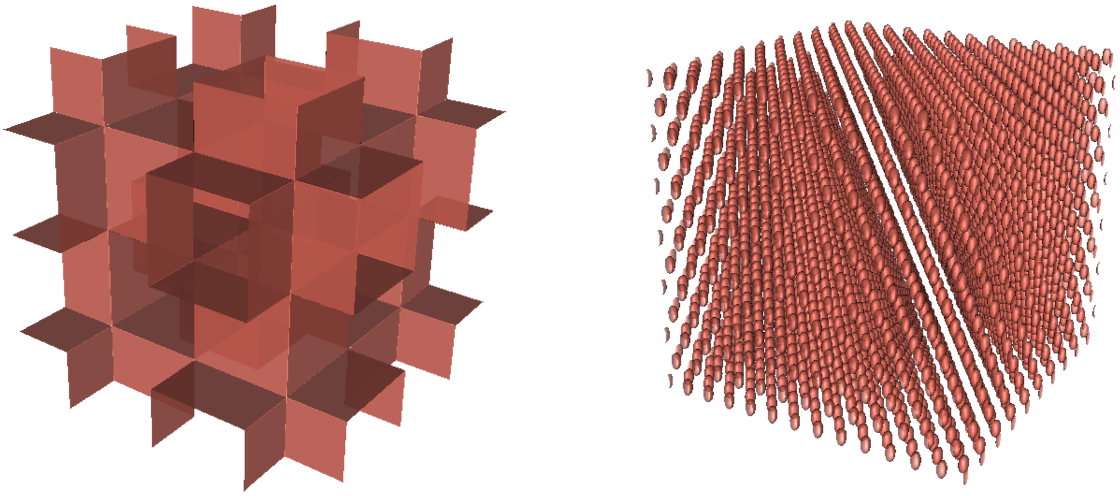

(a) Boxes (b) Ellipsoids

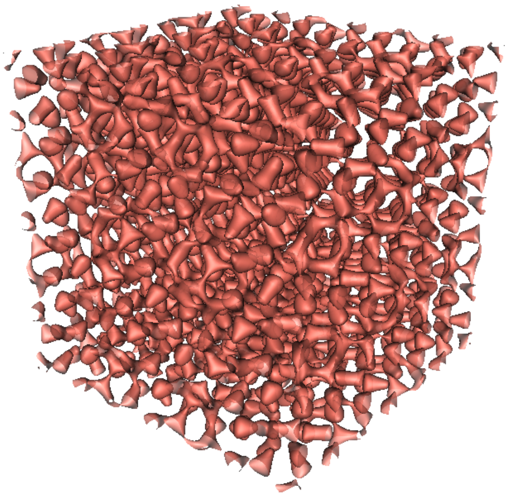

(c) Irregular Structure

Figure 4.17: Implicit Porous Structures

$d_2 < d_3$. Let $\aleph$ be an implicit porous structure. An inner-structured thin implicit patch can be directly constructed in the following way:

$$\begin{array}{lrcl} \text{(a)} & \Xi^{+} & = & \bar{\bar{\mathcal{S}}}_{d_0} \backslash \bar{\bar{\mathcal{S}}}_{d_3} \\ \text{(b)} & \Xi^{-} & = & \bar{\bar{\mathcal{S}}}_{d_1} \backslash \bar{\bar{\mathcal{S}}}_{d_2} \\ \text{(c)} & \Xi^{\#} & = & \Xi^{-} \backslash \aleph \\ \text{(d)} & \Xi & = & \Xi^{+} \backslash \Xi^{\#} \end{array} \tag{4.16}$$

where Ξ^{+} and Ξ^{-} are the outer and inner thin implicit patches, $\Xi^{\#}$ is the inner thin patch deformed by the implicit porous structure $\aleph$, Ξ is the inner-structured thin implicit patch.

For example, in Figure 4.20, an inner-structured thin implicit patch is con-

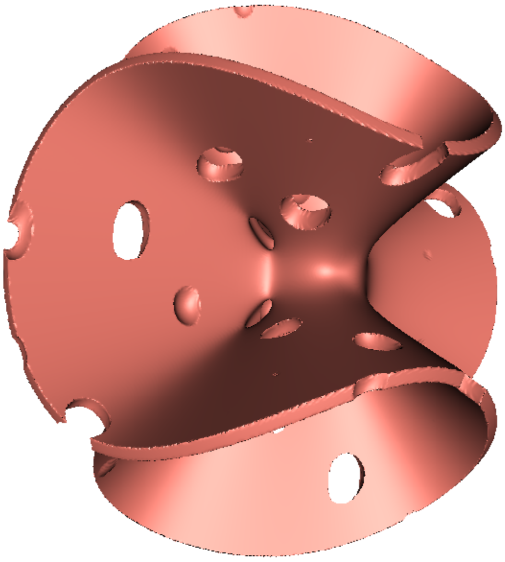

Figure 4.18: Porous Structure on TIP of Clebsch Surface

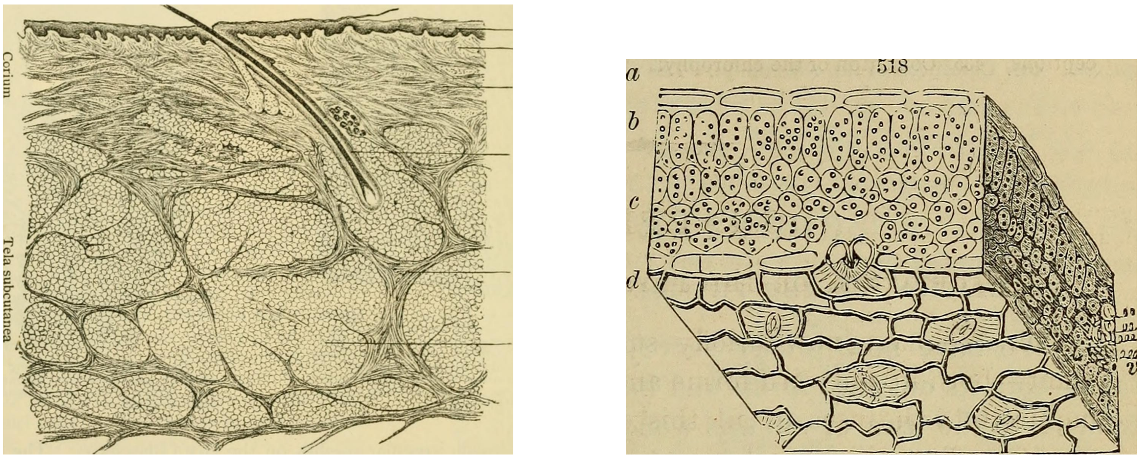

(a) Skin (Dwight et al. 1923)

(b) Leaf (Wood 1870)

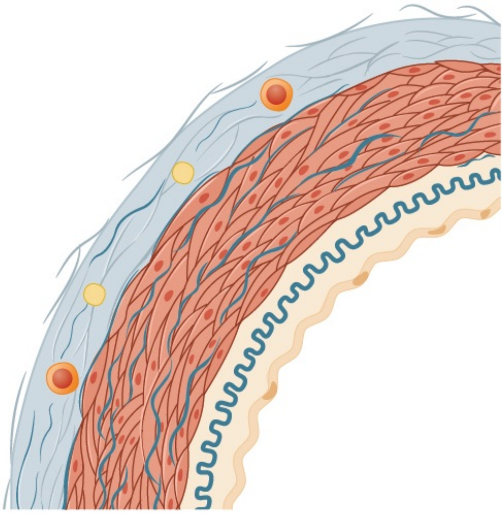

(c) Vascular Wall (Betts 2013)

Figure 4.19: Interior Structures of Real-world Thin Solids

structed based on the implicit function $f(x,y,z) = g_{\cup_{2,0.9}}(\frac{1}{4}x^2 + 4y^2 + z^2 - 1, 4x^2 + \frac{1}{4}y^2 + z^2 - 1)$. Let $\mathcal{S} = Z(f)$ and $d_0 = 0, d_1 = 0.2, d_2 = 0.4, d_3 = 0.6$, then

- in Figure 4.20(a), the outer implicit patch is given by $\Xi^+ = \bar{\bar{\mathcal{S}}}_{d_0} \backslash \bar{\bar{\mathcal{S}}}_{d_3}$
- in Figure 4.20(b), the inner implicit patch is give by $\Xi^- = \bar{\bar{\mathcal{S}}}_{d_1} \backslash \bar{\bar{\mathcal{S}}}_{d_2}$
- in Figure 4.20(c), the structured inner implicit patch is constructed by $\Xi^\# = \Xi^- \backslash \aleph$, where $\aleph$ is the implicit porous structure shown in Figure 4.17(b)
- in Figure 4.20(d), the final inner-structured thin implicit patch is generated by $\Xi = \Xi^+ \backslash \Xi^\#$

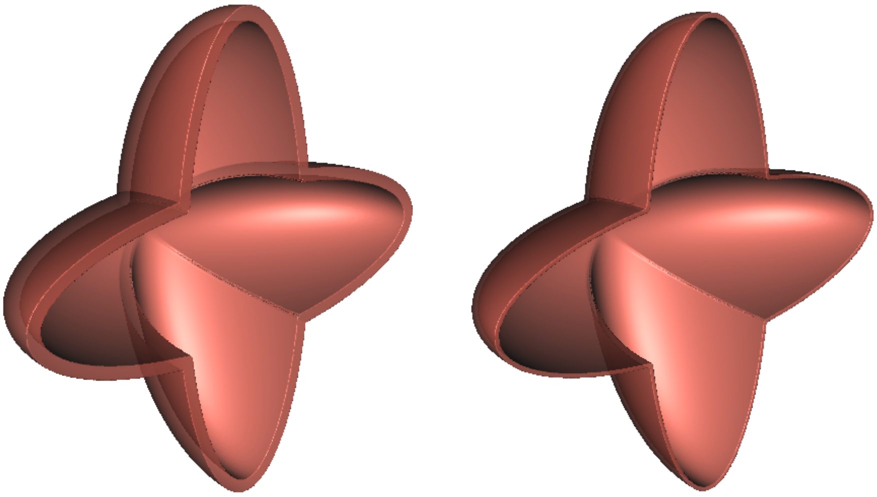

(a) $\Xi^+ = \bar{\bar{\mathcal{S}}}_{d_0} \backslash \bar{\bar{\mathcal{S}}}_{d_3}$ (b) $\Xi^- = \bar{\bar{\mathcal{S}}}_{d_1} \backslash \bar{\bar{\mathcal{S}}}_{d_2}$

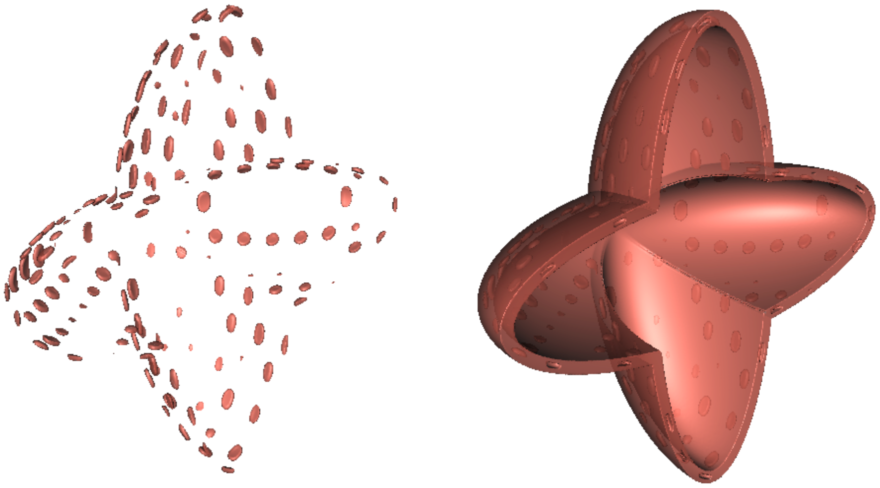

(c) $\Xi^\# = \Xi^- \backslash \aleph$ (d) $\Xi = \Xi^+ \backslash \Xi^\#$

Figure 4.20: Inner-structured Thin Implicit Patch

With the proposed method, for instance, the thin solid spout of the Utah teapot can be embedded with certain porous structures directly. Let $\mathcal{S}$ be the implicit surface expressed as the approximate distance, $\aleph$ be the implicit porous structure shown in Figure 4.17(c), $d_0 = 0, d_1 = 1, d_2 = 2, d_3 = 3$, according to Equation 4.16, the outer implicit patch, inner implicit patch, structured thinner implicit patch and the inner-structured thin implicit patch are given in Figure 4.21.

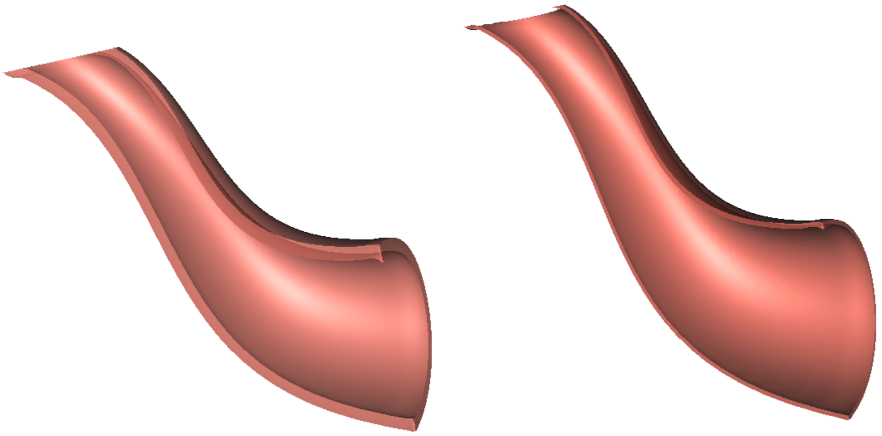

(a) $\Xi^+ = \bar{\bar{\mathcal{S}}}_{d_0} \backslash \bar{\bar{\mathcal{S}}}_{d_3}$ (b) $\Xi^- = \bar{\bar{\mathcal{S}}}_{d_1} \backslash \bar{\bar{\mathcal{S}}}_{d_2}$

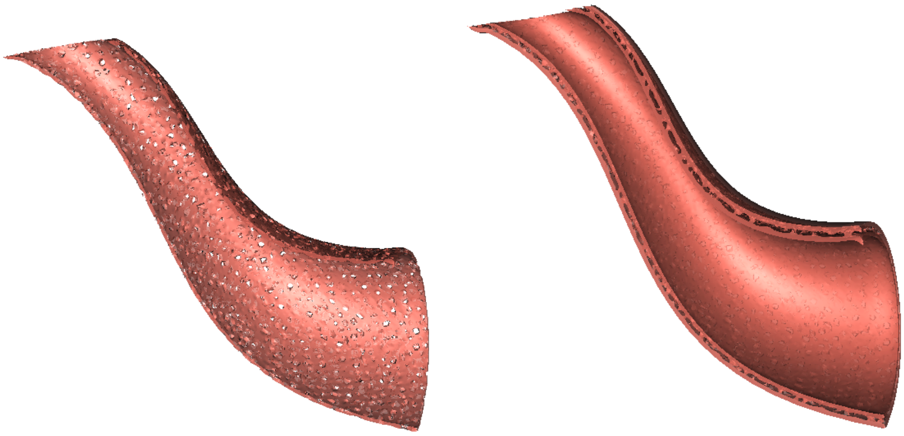

(c) $\Xi^\# = \Xi^- \backslash \aleph$ (d) $\Xi = \Xi^+ \backslash \Xi^\#$

Figure 4.21: Inner-structured Spout

4.3.3 Multi-layer TIP

More implicit porous structures can be embedded into a same thin solid to make multi-layer inner structure within a thin implicit patch.

Let $\mathcal{S}$ be an implicit surface, $\bar{\bar{\mathcal{S}}}_{d_i}$ be the implicit offset surfaces of $\mathcal{S}$. A thin implicit patch with n layers of interior structures can be constructed in the following way:

$$\begin{aligned}
\Xi^{+} &= \bar{\bar{\mathcal{S}}}_{d_0} \backslash \bar{\bar{\mathcal{S}}}_{d_{2n+1}} \\
\Xi_i^{-} &= \bar{\bar{\mathcal{S}}}_{d_{2i-1}} \backslash \bar{\bar{\mathcal{S}}}_{d_{2i}} \\
\Xi_i^{\#} &= \Xi_i^{-} \backslash \aleph_i \\
\Xi &= \Xi^{+} \backslash \Xi_0^{\#} \backslash \Xi_1^{\#} \backslash \ldots \backslash \Xi_i^{\#} \backslash \ldots \backslash \Xi_n^{\#}
\end{aligned} \tag{4.17}$$

where Ξ^{+} is the outer thin implicit patch, Ξ_i^{-} is the i-th inner thin implicit patch, $\aleph_i$ is the i-th implicit porous structure, $\Xi_i^{\#}$ is the i-th structured inner thin implicit patch, $\bar{\bar{\mathcal{S}}}_{d_i}$ is an implicit offset surface of $\mathcal{S}$, $i = (0, 1, \ldots, n-1)$, d is a small constant such that $d_{2i-1} < d_{2i}$.

Figure 4.22 shows an implicitly modelled multi-layer blood vessels tissue structures for a section of a blood vessel. It is modelled as a thin solid with three layers of implicit porous structures. This simulated vascular wall is peeled layer by layer to show its inner structures. It is generated in the following way:

$$\begin{aligned}
\Xi^{+} &= \bar{\bar{\mathcal{S}}}_{d_0} \backslash \bar{\bar{\mathcal{S}}}_{d_7} \\
\Xi_0^{-} &= \bar{\bar{\mathcal{S}}}_{d_1} \backslash \bar{\bar{\mathcal{S}}}_{d_2} \\
\Xi_0^{\#} &= \Xi_0^{-} \backslash \aleph_0 \\
\Xi_1^{-} &= \bar{\bar{\mathcal{S}}}_{d_3} \backslash \bar{\bar{\mathcal{S}}}_{d_4} \\
\Xi_1^{\#} &= \Xi_1^{-} \backslash \aleph_1 \\
\Xi_2^{-} &= \bar{\bar{\mathcal{S}}}_{d_5} \backslash \bar{\bar{\mathcal{S}}}_{d_6} \\
\Xi_2^{\#} &= \Xi_2^{-} \backslash \aleph_2 \\
\Xi &= \Xi^{+} \backslash \Xi_0^{\#} \backslash \Xi_1^{\#} \backslash \Xi_2^{\#}
\end{aligned} \tag{4.18}$$

In Figure 4.23, the spout of the Utah teapot has been modelled as a TIP with inner structures with embedded three-layer implicit porous structures created based on the formula Equation 4.17. Theoretically, the implicit porous structures can be embedded into any implicit solid to make various geometries with complicated interior structures. More examples will be given in the next section.

In this section, a porous structure design technique using implicit functions is developed. With the proposed technique, a geometric object with a required interior geometric structure can be represented as an implicit function. It can be further extended from the perspective of interior geometric structure design to interior structure reconstruction when the actual internal geometric structures, such as the vascular tissue structures, can be digitally captured.

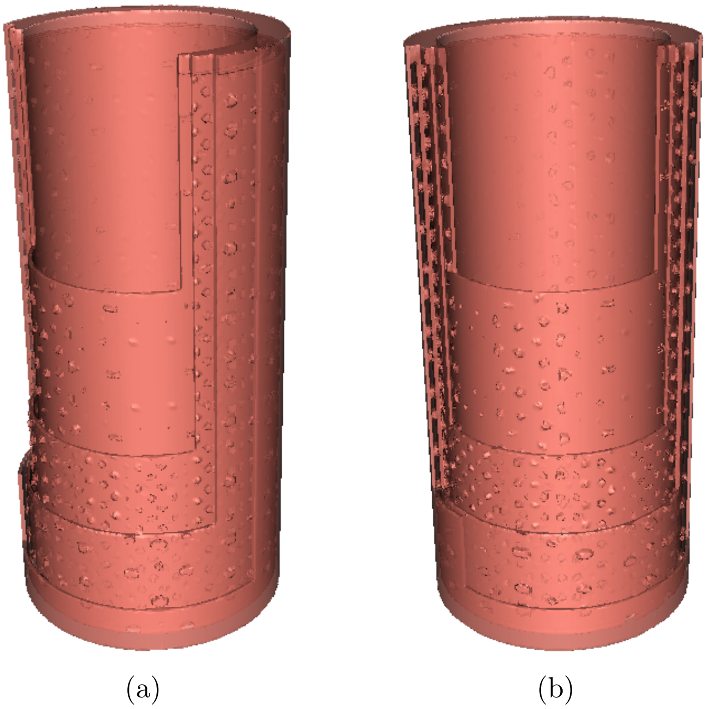
(a) (b)

Figure 4.22: A Simulated Vascular Wall with Multi-layers

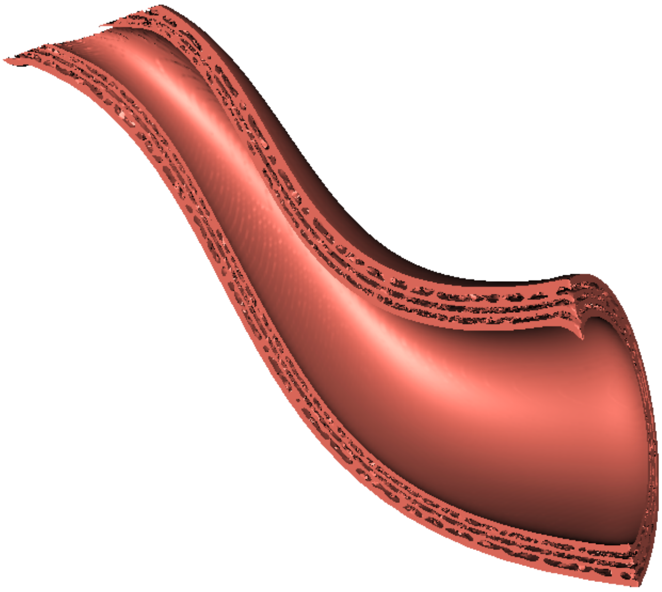

Figure 4.23: The Spout with Multi-layer Interior Structures

4.4 Discussion and Experiments

In previous sections, both the implicit surface and the parametric surface have been converted into thin solid together with a certain embedded interior material structure. Multiple thin implicit patches can be combined together to build more complex thin-patched objects with shape-preserving implicit blending operations. In this section, some more experimental results are presented to demonstrate the flexibility, advantages, as well as the limitations of the proposed method.

4.4.1 Discussion

Firstly, the prospered method is capable of converting any surface-based objects into thin implicit solid surfaces. The half teapot shown in Figure 4.24 is a blending of nine thin implicit solid patches, each of which is obtained by converting a bicubic Bézier surface patch used for building the classic Utah teapot. In general, geometric complexity can always be divided into simple ones and converted into a set of thin implicit solid patches with the proposed method, which are then combined them together to form a whole thin solid.

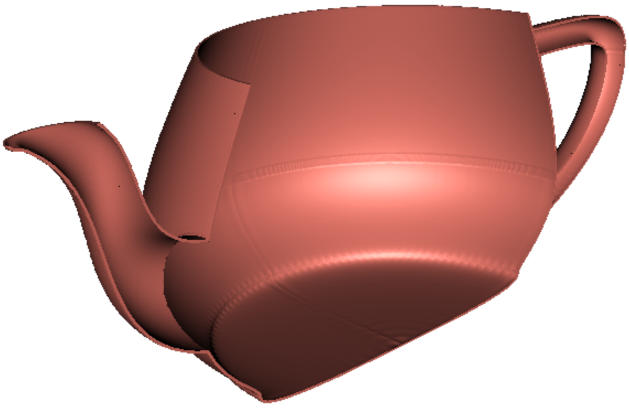

Figure 4.24: Printable Half Teapot

Secondly, the implicitly represented shapes of thin solids can be easily edited. For example, the original Utah teapot was designed for visualisation purpose without eliminating unwanted connections inside it. Figure 4.25(a) shows unwanted connection between the teapot body and the spout. As an implicit object, this redundancy can be easily removed by using subtraction blending operation. The trimmed connection is shown in Figure 4.25(b). The connection between the handle and the teapot body also has this problem. Figure 4.26 compares the original connection designed for the Utah teapot and the trimming result of these unwanted parts.

In addition, the internal material structures can be embedded inside the thin solid patch with the proposed method. Figure 4.27 shows the thin solid surface converted from the half teapot, together with embedded porous internal material structures. Figure 4.27(a) gives the rendering of the geometric model and Figure 4.27(b) presents the printed result. It is worth noting that it is difficult to build this thin-solid porous

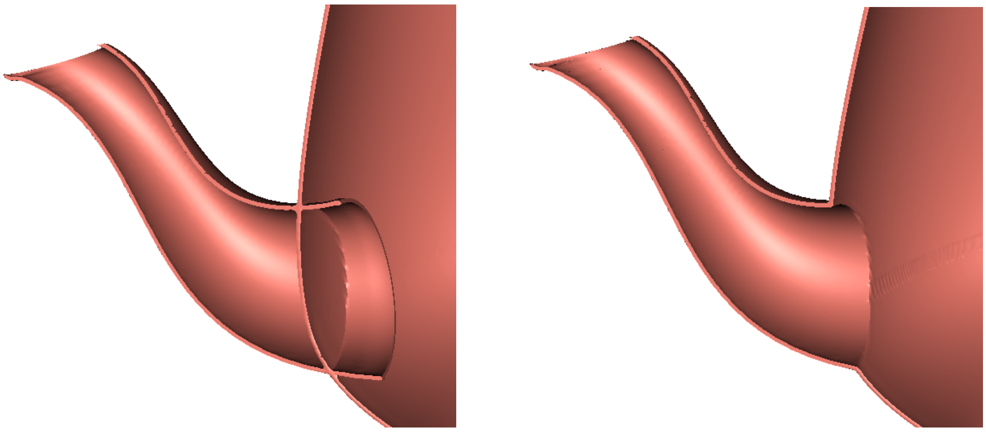
(a) Unwanted Connection (b) Trimmed Connection

Figure 4.25: Inner Connection of Spout and Body of the Utah Teapot

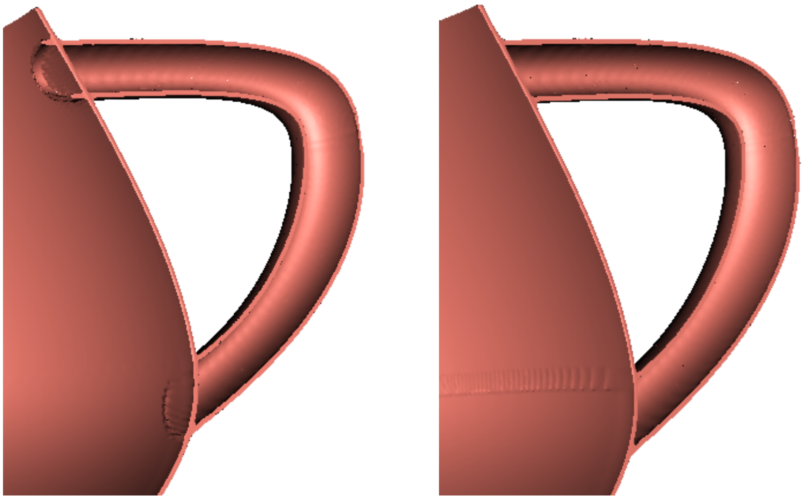
(a) Unwanted Connection (b) Trimmed Connection

Figure 4.26: Inner Connection of Handle and Body of the Utah Teapot

object using parametric offset surfaces and related thickening techniques from the original bicubic Bézier patches.


(a) (b)

Figure 4.27: Thin Implicit Patch of the Utah Teapot

The main limitation of the proposed method is that an additional trimming process needs to be applied after the implicit fitting operation. This is because an implicitly represented object constructed from this method will always generate a relatively rounded boundary and has to be trimmed to create the thin-solid surface. Figure 4.8(a) and Figure 4.8(b) compare the non-trimmed and the trimmed implicit objects. The required trimming plane or surface should be carefully constructed to give the correct result.

4.4.2 Further Experimental Results

The proposed method can also be used on unorganised points. These points are sampled from real-world objects and have been reconstructed as implicit objects.

Human Face

Figure 4.28 presents a human face reconstructed from sampling points and printed as a thin implicit surface.

Figure 4.28(a) gives the original point cloud. These points are collected from a real human face. An implicit object is reconstructed from these points and rendered as an implicit surface in Figure 4.28(b). This implicit surface is trimmed and converted into a thin patch shown in Figure 4.28(c). The thin patch is printed out using a 3D printer. Figure 4.28(d) shows the printed result.

In this example, the porous interior structures have been embedded into the thin solid geometric surface but are not easy to observe in Figure 4.28(d), since the patch is very thin. Note that the redundant parts at the shoulder of the head in Figure 4.28(b) come from the inaccurate implicit surface fitting (Li et al. 2004b).

Human Tibia

Figure 4.29 shows a reconstructed human tibia represented as a thin implicit patch with porous structures on it.

Figure 4.29(a) shows an implicitly reconstructed tibia object. The sampling points collected from a real tibia is not shown. With the proposed method, this implicitly represented tibia is converted as a thin implicit patch. Figure 4.29(b) renders the thin-patched tibia together with the original points. The thin-patched

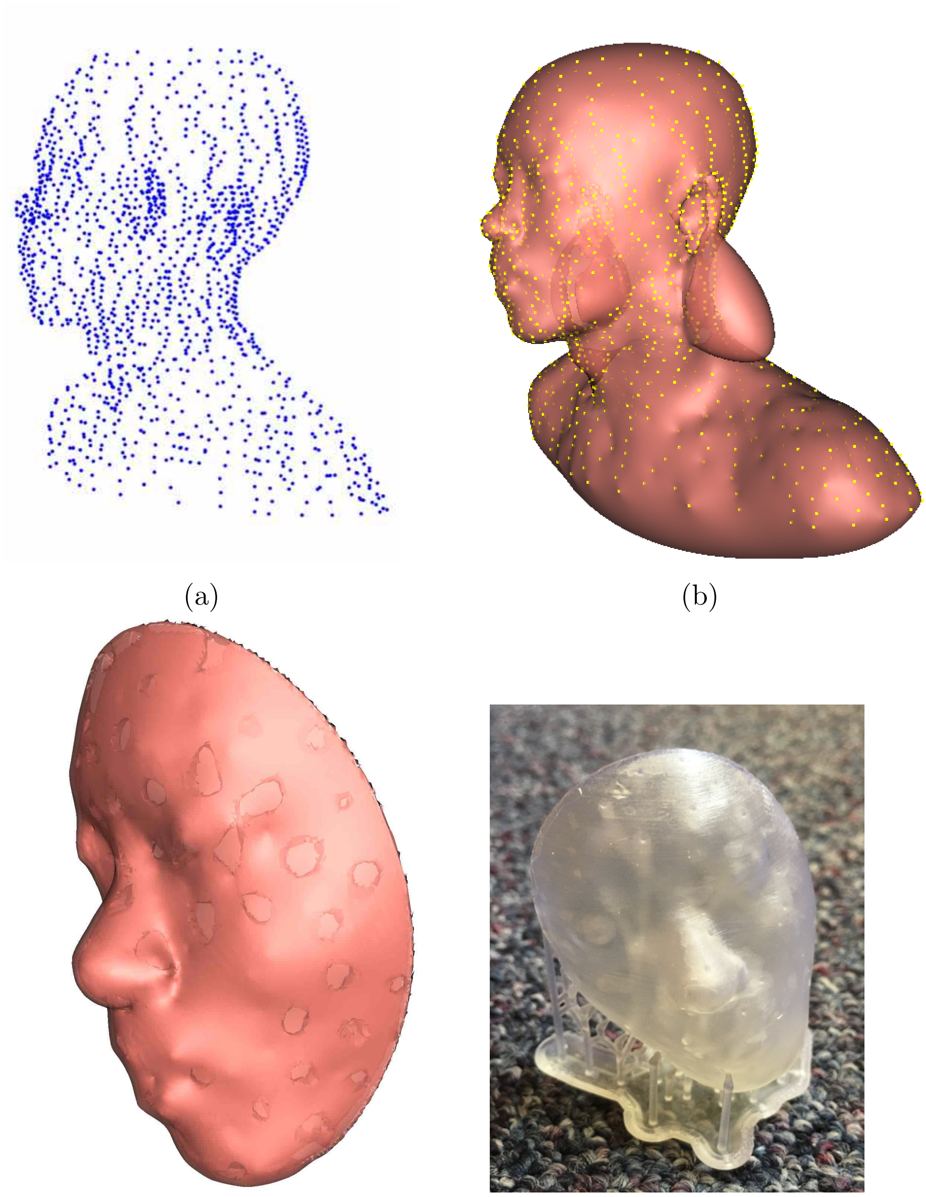

(a) (b)

(c) (d)

Figure 4.28: Thin Implicit Patch of a Face

tibia is chopped by a plane to show its inner side. Figure 4.29(c) embeds porous structures onto the thin-patched tibia. This tibia has been printed out and shown in Figure 4.29(d).

Blood Vessel

The thin implicit patch is initially proposed to model the tissue structures of the blood vessel wall. By suing the proposed method, the original surface-based blood vessel geometric representation can be converted into a thin solid surface patch represented as an implicit function. Because the shape of a blood vessel segment

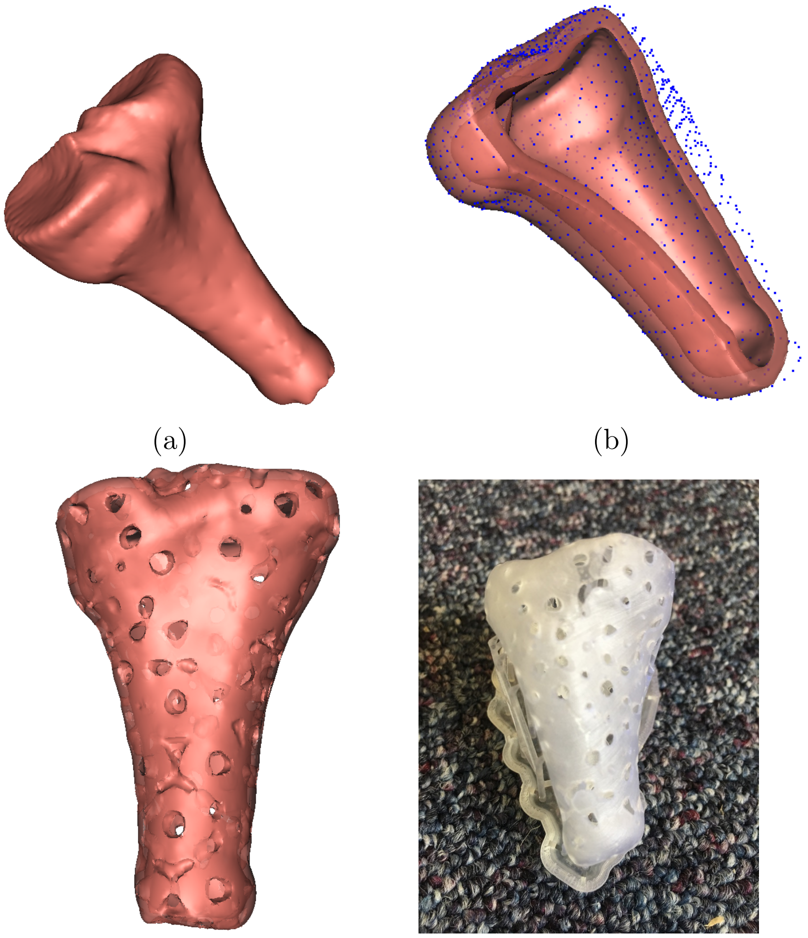

(a) (b)

(c) (d)

Figure 4.29: Thin Implicit Patch of a Tibia

is a short thin generalised cylinder, the conversion does not need extra trimming operations.

Figure 4.30 presents the blood vessel segments with thin solid wall modelled with the proposed TIP method corresponding to Figure 3.5. They are rendered with a translucent colour to show the thickness. No interior structures are integrated in this example.

The thin solid blood vessel wall segments in Figure 4.30(a) to Figure 4.30(h) are achieved by converting the surface objects shown in Figure 3.5(a) to Figure 3.5(h) using the approximate distance method.

Interior structures can be integrated into the thin-patched curvy blood vessel. Figure 4.31 shows this integration. Figure 4.31(a) shows a porous structure embedded into the vessel wall. The blending of the thin solid vascular surface and the modelled interior porous structure is shown in Figure 4.31(b).

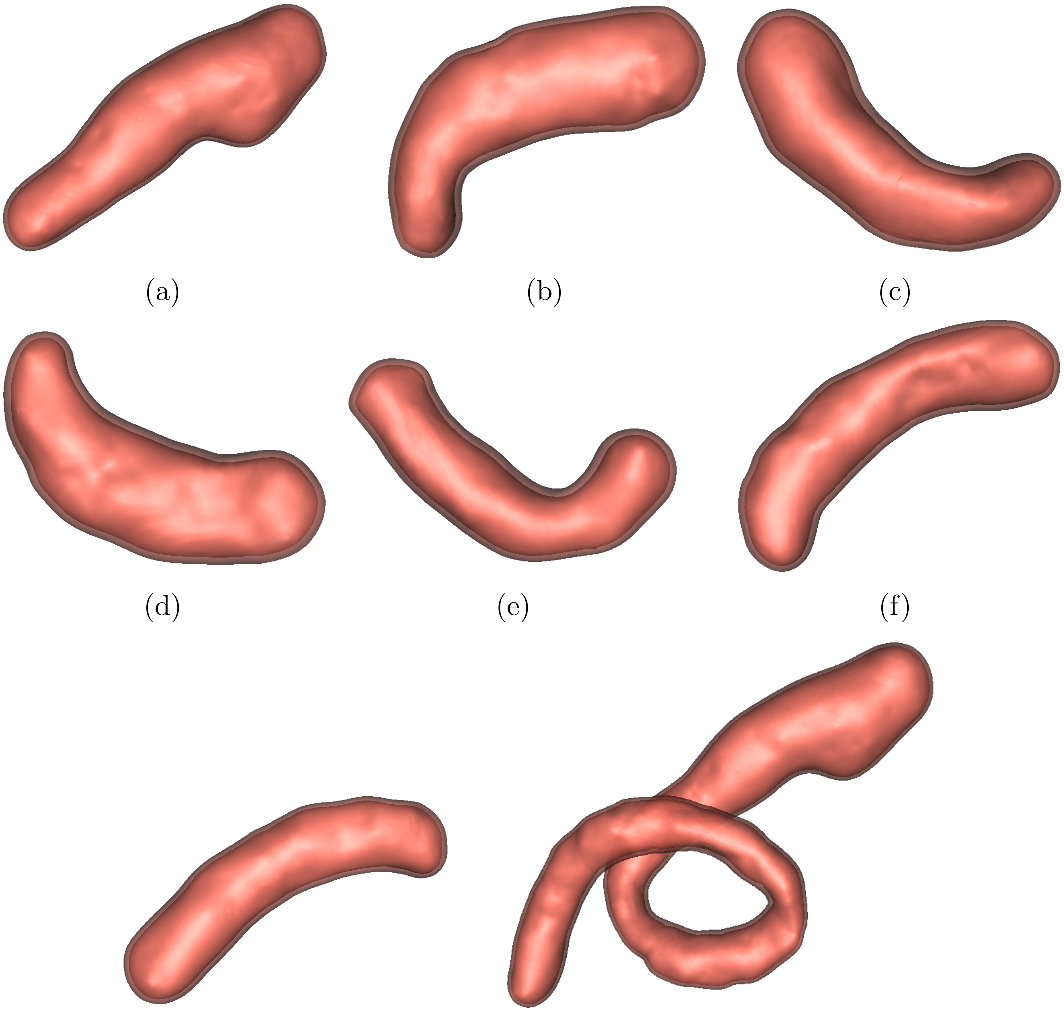

(a) (b) (c)

(d) (e) (f)

(g) (h)

Figure 4.30: Thin-patched Blood Vessel

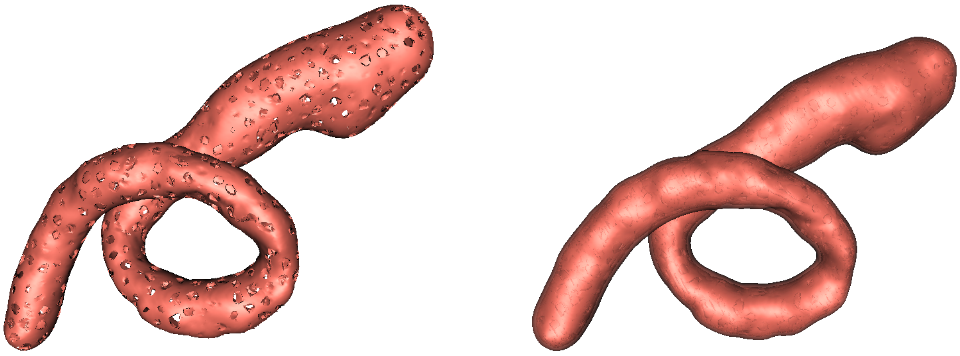

(a) (b)

Figure 4.31: Blood Vessel with Interior Structures

The proposed method can be used on more complex blood vessel. Figure 4.32 shows the TIP-represented branched blood vessel converted from Figure 3.11. For better observation only the middle part is shown. Figure 4.32(a) gives a rendering result without interior structures being integrated. Figure 4.32(b) shows the porous structures to be embedded into the blood vessels wall. Figure 4.32(c) shows the blending result of the thin solid vascular solid wall and the modelled interior structure.

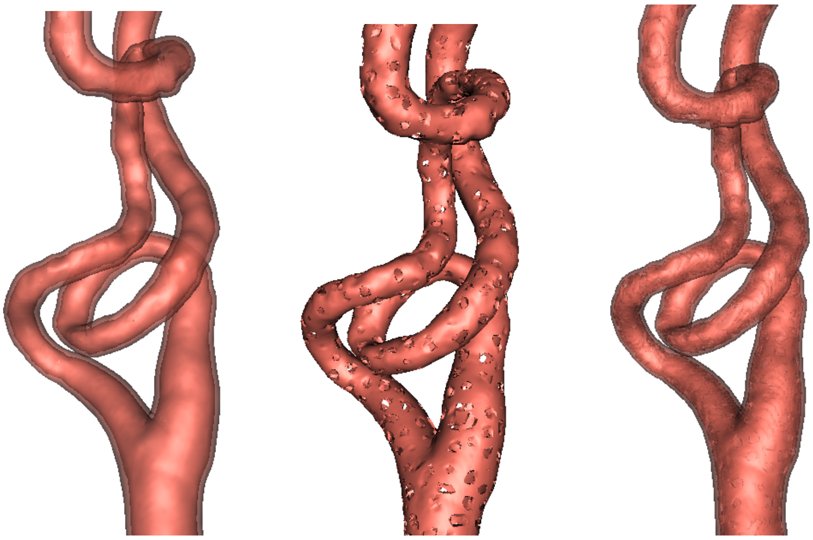

(a) (b) (c)

Figure 4.32: Branched Blood Vessel with Interior Structures

Multi-layer Vascular Wall

As shown in Figure 4.1, a real vascular wall consists of multiple layers of different issues. These issues can be simulated with the multi-layer implicit porous structures inside the vascular wall.

Figure 4.33 provides a cross-section view of the multi-layered blood vessel tissue structure. Figure 4.33(a) gives a longitudinal cross-section view of the vascular wall and Figure 4.33(b) provides a close-up view to show the details of this section. Figure 4.33(c) and Figure 4.33(d) show two cross-sections of this wall.

4.5 Summary

To the author's best knowledge, all the existing geometric vascular modelling techniques are surface-based, where the complex vascular wall tissue structures are rarely considered. However, the real-world blood vessels are with solid walls and a wall consists of multiple layers with interior material structures. The surface-based object cannot faithfully represent the geometries of the real-world blood vessels. In order

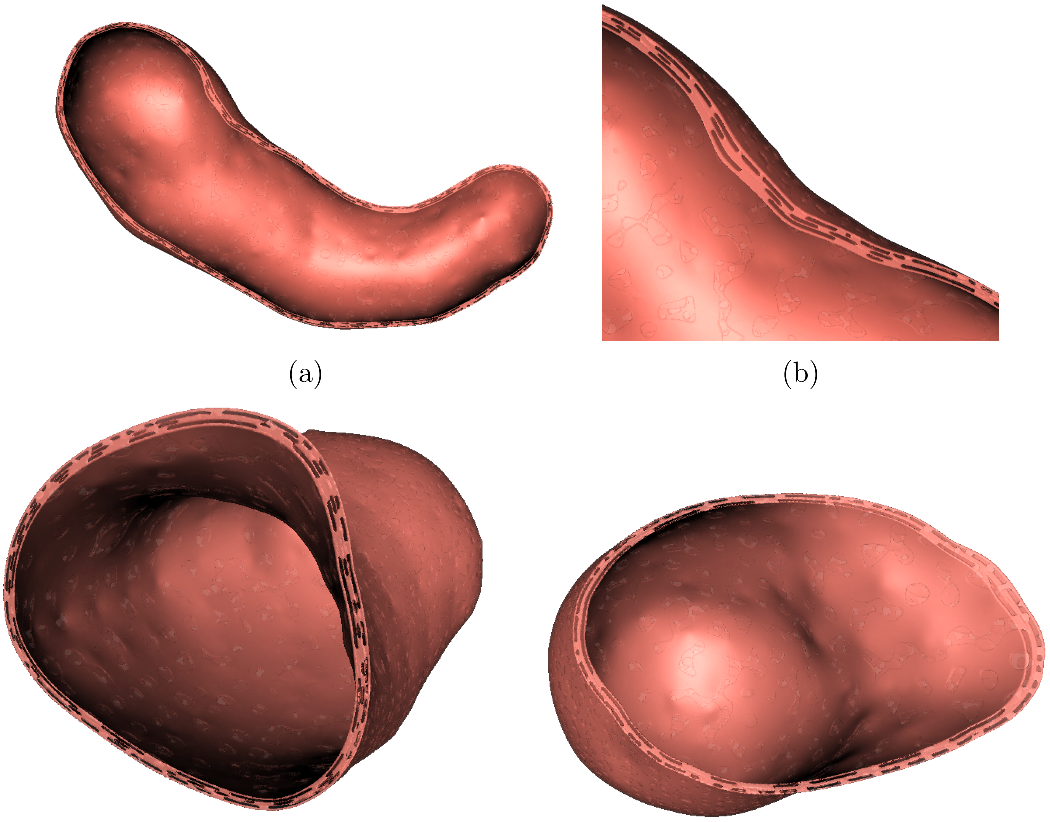
(a) (b)

(c) (d)

Figure 4.33: A Multi-layer Vascular Wall

to solve this problem, this chapter presents a technique to convert the surface-based implicit object to the thin implicit solid with interior structures to give a correct representation of the reconstructed blood vessels.

The thin implicit patch is proposed to convert a surface-based object to be a thin solid object. With the proposed method, the surface of the original object is first represented as an implicit surface by using the direct RBF surface fitting with ellipsoid constraint, then one or more implicit offset surfaces are generated with implicit blending operations. A thin solid is acquired by blending these offset surfaces. The implicitly modelled interior structures are used to simulate the internal structures of a solid. These structures can either be designed with implicit functions or be modelled from real-world objects. Since they are implicit objects, the implicit blending operations can embed them inside another implicit object. With TIP, both the single-layer and multi-layer thin implicit patches can be easily generated. The reconstruction of the Utah teapot is used as an example to illustrate how the proposed techniques work and how to embed porous structures into the converted thin-solid.

The proposed methods have been used on the reconstruction of thin solids from the real world. A human face and a human tibia have been converted into thin implicit patches with interior structures embedded. These two items have been printed out with a 3D printer, as implicitly represented geometric objects are additive manufacturing friendly and can be printed directly using 3D printers. Blood vessels reconstructed with the method proposed in Chapter 4 are also thin-patched and inner-structured. A short segment of this blood vessel is constructed with a multi-layer vascular wall. These examples demonstrate that the proposed methods can not only convert surface to thin solid with the desired thickness but also be able to edit the shape and interior material structures of the thin solid.

The proposed methods can be used on the fine solid reconstruction of real-world objects with sophisticated structures. The future study of this method will be high-accuracy and high-performance geometric reconstruction of multi-layer vascular walls.

Chapter 5

Conclusion and Future Work

The geometric vascular modelling plays an essential role in the applications of computer-assisted surgery and minimally invasive vascular surgery. The complicated blood vessels extracted from the medical images are required to be accurately reconstructed branch by branch and then combined together to be a complete vascular tree. This reconstructed vascular tree is an integrated geometry such that further geometrical and biomedical analysis can be continued.

It is a challenging job to reconstruct the geometric structures of blood vessels because these blood vessels are of a complicated tree structure with various branches and joints. How to faithfully represent the shape of a single blood vessel and how to effectively combine different blood vessels together to make a complete vascular geometry place huge difficulties on the vascular modelling task. Although variety of vascular modelling techniques have been proposed, they are either too ideal on the shape representation to give the accurate description of blood vessels or too inefficient on the reconstruction of the surface approximation to give a high-performance computation vascular modelling. Besides, blood vessels are with highly complex tissue structures, but the existing vascular modelling techniques are all surface-based, the true structure of the vascular wall cannot be faithfully reflected. In order to solve these problems, this research sought to develop a new image-based geometric vascular modelling technique to give fine descriptions on the vascular wall with an advanced modelling approach.

In this research, a high-performance computation parallel vascular geometry reconstruction technique, called Skeleton Marching, has been proposed. There are several distinguished advantages of this technique.

First, this technique can provide accurate reconstruction with low computational complexity. It allows to divide the blood vessels into short and less curvy segments such that both the segmentation and the surface fitting only target very small point datasets sampled from very simple geometries. The direct RBF surface fitting with ellipsoid constraint guarantees the accuracy of the surface fitting of each vascular segments, and the shape-preserving blending operations assure the joints combined by different blood vessels hold the original shape as much as possible. Both of these two algorithms are with low time complexity.

Secondly, unlike some other methods, such as the sweep surface method, the skeleton marching method approximately represent the data points of a vascular segment as a short capsule-like localised implicit object and directly blends them into a vascular tree. No extra operations are required and the modelling performance is therefore improved.

Thirdly, this is a parallel-friendly technique. The skeleton marching method is based on the implicit modelling technique such that different blood vessel branches and different vascular sections can be reconstructed independently from the reconstruction of other vessel branches and sections.

Another main contribution made in this research is the introduction of the Thin Implicit Patch (TIP), a novel vascular tissue structure modelling technique. To the best knowledges of the author, this is the first vascular modelling technique to augment the surface-based vascular wall to be thin solid with interior structures. The proposed method is simple and easy to be implemented, and can be applied to model any required tissue structures. There are two originalities in the TIP technique:

Most existing vascular modelling techniques are surface-based. Despite the fact that a surface is easy to be visualised and is convenient for subtractive manufacturing, it is in general difficult to model real-world volumetric complex tissue structures. In addition, the surface-based geometric representation is not additive manufacturing friendly. It has to be converted into a volumetric form for the purpose of 3D printing. This is not a trivial task when internal geometric structures of an object need to be considered. The TIP technique proposed in this research provides a method for converting any given surface into an implicit function representing a thin solid object. This technique can produce a thin implicit surface with a uniform thickness. Both artificial and real-world data have been used to show the effectiveness and the efficiency of the TIP method.

A vascular wall is not only a thin surface with a thickness but also consists of high complex multi-layered tissue structures. Although the real fine internal structure of the vascular wall is hard to capture by normal medical imaging techniques, it is possible to model its structure with high faithfulness. In this research, Implicit Interior Structures (IIS) are designed by the implicit porous structures with real field functions such that complex internal structures can be easily embedded inside the thin implicit patch. The integration of implicit offset surfaces and IIS gives out multi-layered thin surfaces. This is a novel method for fine reconstruction of the geometric vascular tissue structures.

This research has achieved the goal of developing a high-performance computation and high-accuracy geometric vascular reconstruction technique, though there are still many technical issues which remain to be solved in the future work.

First, further improvement of the performance on the proposed method is still needed. Although the modelling performance has been significantly improved by the skeleton marching approach, there are still many areas which need to be optimised. For one thing, the surface fitting of the localised implicit objects has multiple choices. Though the direct RBF fitting with ellipsoid constraint is designed for small dataset and it works fine in this research, it does not mean no better fitting method can be chosen. The solution of the eigensystem in the direct RBF fitting is still cumbersome even with parallel computing. A better surface fitting will improve the modelling performance at the algorithmic level. For another, the skeleton marching method can be redesigned to make it more parallel computing efficient. Although parallel computing has been used in the implementation of the proposed method, it is only running on the remote HPC which has multiple GPUs. With improved algorithm and improved GPU technology, the skeleton marching technique can be running on a local computer with a GPU of massive processing cores.

Secondly, it is with the fine vascular reconstruction based on the true anatomical structures of the blood vessel wall or the captured vascular tissues structures using a certain tissue imaging technique. While it is an interesting and useful improvement from the surface-based vascular modelling to the thin solid vascular modelling with interior structures. But what can be achieved with the proposed technique are still very limited. On the one hand, the vascular image in this research does not contain useful information of the internal structure of vascular wall due to the limitation of ordinary imaging techniques. Although porous structures are used to simulate the inside of the blood vessel wall, it is far from sufficient to represent the true interior structures of the real-world blood vessels. The vascular tissue modelling proposed in this research only provides a possible solution to integrate interior structures inside the vascular wall, but there still is a long way to go for the faithful reconstruction of the actual tissue structures. On the other hand, what has been achieved for the interior structures of the vascular wall is only a coarse representation of blood vessels without noticing the more detailed structures on the cell or deeper level. However, the cardiovascular diseases may occur inside a cell and behave as the deformation or injury of cells. The fine reconstruction of the vascular tissue requires more detailed geometric description on these fine and delicate structures.

Thirdly, in addition to the two relatively more immediate tasks, some investigations on the hemodynamic analysis based on the vascular geometries reconstructed from patient-specific dataset will be carried out in future. The geometric reconstruction of blood vessels will not only supply the geometric structures of the blood vessels but it is also a premise on the blood flow simulation inside the vascular lumen. This is because the cardiovascular diseases may lead to the deformation of the blood vessels and then influence the blood transformation and biological functions of related tissues. The analysis of the hemodynamic plays an essential role on the diagnosis and treatment of the cardiovascular diseases (Antiga et al. 2008; Mittal et al. 2016). In addition, the research of endovascular devices is closely related with the hemodynamic analysis. The research and development of these high-precision instruments rely on accurate modelling of the vascular geometry and computational blood fluid simulation.

Last but not least, it is the research on virtual surgery by interactively modifying the vascular geometric shapes or geometric structures. The virtual surgery allows the surgeons to modify the shape of the blood vessels and observe the surgical results without real surgery. Interactive editing can deform and change the shape or size of the blood vessels to enable flexible analysis of cardiovascular diseases and related researches.

References

Adams, R. and Bischof, L. (1994). “Seeded region growing”. In: *IEEE transactions on pattern analysis and machine intelligence* 16.6, pp. 641–647 (cit. on p. 19).

Agin, G. J. (1972). “Representation and description of curved objects”. In: *Stanford Artificial Intelligence Report* (cit. on p. 18).

Alesic, Z. K. and Wyvill, B. (1991). “Controlled blending of procedural implicit surfaces”. In: *Proceedings - Graphics Interface.* University of Calgary, Calgary, Canada, pp. 236–245 (cit. on p. 24).

Alexe, A., Gaildrat, V., and Barthe, L. (2004). “Interactive modelling from sketches using spherical implicit functions”. In: *Proceedings of the 3rd international conference on Computer graphics, virtual reality, visualisation and interaction in Africa*, p. 25 (cit. on p. 15).

Allègre, R. et al. (2006). “The hybridtree: Mixing skeletal implicit surfaces, triangle meshes, and point sets in a free-form modeling system”. In: *Graphical models* 68.1, pp. 42–64 (cit. on p. 15).

Almasi, G. S. and Gottlieb, A. (1989). *Highly Parallel Computing.* Redwood City, CA, USA: Benjamin-Cummings Publishing Co., Inc. (cit. on p. 58).

Alwan, A. (2011). *Global status report on noncommunicable diseases 2010.* (Cit. on p. 1).

Angelidis, A. and Cani, M. P. (2002). “Adaptive implicit modeling using subdivision curves and surfaces as skeletons”. In: *Eurographics 2014 - State of the Art Reports* (cit. on p. 15).

Angles, B. et al. (2017). “Sketch-based implicit blending”. In: *ACM Transactions on Graphics* 36.6, pp. 1–13 (cit. on p. 40).

Antiga, L. (2002). “Patient-specific modeling of geometry and blood flow in large arteries”. PhD thesis. Mario Negri Institute: Politecnico di Milano (cit. on pp. 7, 19).

Antiga, L., Ene-Iordache, B., and Remuzzi, A. (2003). “Centerline Computation and Geometric Analysis of Branching Tubular Surfaces with Application to Blood Vessel Modeling.” In: *WSCG 2003* (cit. on pp. 12, 13, 18).

Antiga, L. et al. (2008). “An image-based modeling framework for patient-specific computational hemodynamics”. In: *Medical & Biological Engineering & Computing* 46.11, pp. 1097–1112 (cit. on pp. 20, 49, 50, 56, 106).

Araújo, B. R. de et al. (2015). “A Survey on Implicit Surface Polygonization”. In: *ACM Computing Surveys* 47.4, pp. 1–39 (cit. on p. 28).

Bajaj, C. (1997). “Implicit surface patches”. In: *Introduction to Implicit Surfaces* (cit. on p. 24).

Barbier, A. and Galin, E. (2004). “Fast Distance Computation Between a Point and Cylinders, Cones, Line-Swept Spheres and Cone-Spheres”. In: *Journal of Graphics Tools* 9.2, pp. 11–19 (cit. on p. 33).

Barthe, L., Gaildrat, V., and Caubet, R. (1998). *Combining implicit surfaces with soft blending in a CSG tree.* Tech. rep. (cit. on pp. 24, 40).

Barthe, L., Gaildrat, V., and Caubet, R. (2001). “Extrusion of 1D Implicit Profiles: Theory and First Application.” In: *International Journal of Shape Modeling* 7.2, pp. 179–198 (cit. on p. 25).

Barthe, L., Wyvill, B., and Groot, E. D. (2004). “Controllable Binary CSG Operators for "Soft Objects"”. In: *International Journal of Shape Modeling* 10.02, pp. 135–154 (cit. on p. 25).

Barthe, L. et al. (2003). “Two-dimensional Potential Fields for Advanced Implicit Modeling Operators.” In: *Computer Graphics Forum* 22.1, pp. 23–34 (cit. on pp. 25, 40).

Bates, R. et al. (2017). “Extracting 3D Vascular Structures from Microscopy Images using Convolutional Recurrent Networks”. In: *arXiv.org.* arXiv: `1705.09597v1 [cs.CV]` (cit. on p. 14).

Berger, M. et al. (2013). “A benchmark for surface reconstruction”. In: *ACM Transactions on Graphics* 32.2, pp. 1–17 (cit. on p. 27).

Berger, M. et al. (2016). “A Survey of Surface Reconstruction from Point Clouds”. In: *Computer Graphics Forum* 36.1, pp. 301–329 (cit. on p. 35).

Berger, M. et al. (2014). “State of the art in surface reconstruction from point clouds”. In: *Eurographics 2014 - State of the Art Reports* (cit. on p. 35).

Bernhardt, A. et al. (2010). “Implicit Blending Revisited.” In: *Computer Graphics Forum* 29.2, pp. 367–375 (cit. on pp. 22, 26, 40).

Betts, J. G. (2013). *Anatomy and physiology.* Houston, Texas: OpenStax College, Rice University (cit. on p. 89).

Bittar, E., Tsingos, N., and Gascuel, M.-P. (1995). “Automatic Reconstruction of Unstructured 3D Data: Combining a Medial Axis and Implicit Surfaces”. In: *Computer Graphics Forum* 14.3, pp. 457–468 (cit. on p. 14).

Blanc, C. and Schlick, C. (1995). “Extended field functions for soft objects”. In: *Proc of Implicit Surfaces* (cit. on p. 23).

Blinn, J. F. (1982). "A Generalization of Algebraic Surface Drawing." In: *ACM transactions on graphics (TOG)* 1.3, pp. 235–256 (cit. on p. 23).

Bloomenthal, J. (1988). "Polygonization of implicit surfaces". In: *Computer Aided Geometric Design* 5.4, pp. 341–355 (cit. on p. 42).

Bloomenthal, J. (1990). "Techniques for Implicit Modeling". In: *SIGGRAPH Course Notes on Modeling and Animating.* Xerox PARC Technical Report, P89-00106, also in SIGGRAPH'90 Course Notes on Modeling and Animating (cit. on pp. 27, 28, 79).

Bloomenthal, J. (1995a). "Bulge Elimination in Implicit Surface Blends". In: *Implicit surfaces* 95, pp. 7–20 (cit. on p. 24).

Bloomenthal, J. (1995b). "Skeletal design of natural forms". PhD thesis. The University of Calgary (cit. on pp. 2, 6, 14, 56).

Bloomenthal, J. (1997). "Bulge Elimination in Convolution Surfaces". In: *Computer Graphics Forum* 16.1, pp. 31–41 (cit. on pp. 24, 40).

Bloomenthal, J. and Bajaj, C. (1997). *Introduction to Implicit Surfaces.* Morgan Kaufmann (cit. on pp. 6, 24).

Bloomenthal, J. and Shoemake, K. (1991). "Convolution surfaces". In: *ACM SIGGRAPH Computer Graphics* 25.4, pp. 251–256 (cit. on pp. 23, 40).

Bloomenthal, J. and Wyvill, B. (1990a). "Interactive techniques for implicit modeling". In: *ACM SIGGRAPH Computer Graphics.* Palo Alto Research Center Incorporated, Palo Alto, United States, pp. 109–116 (cit. on p. 23).

Bloomenthal, J. and Wyvill, B. (1990b). "Interactive techniques for implicit modeling." In: *I3D* 24.2, pp. 109–116 (cit. on pp. 2, 28).

Boas, D. A. et al. (2001). "Imaging the body with diffuse optical tomography". In: *IEEE Signal Processing Magazine* 18.6, pp. 57–75 (cit. on p. 4).

Boskamp, T., Hahn, H. K., and Hindennach, M. (2005). "Geometrical and Structural Analysis of Vessel Systems in 3D Medical Image Datasets". In: *Medical Imaging Systems Technology: Volume 5: Methods in Cardiovascular and Brain Systems* 5, pp. 1–60 (cit. on p. 20).

Britannica, E. (1911). *Encyclopœdia Britannica Eleventh Edition* (cit. on p. 69).

British Heart Foundation (2018). *Cardiovascular disease.* Tech. rep. (cit. on p. 1).

Bühler, K., Felkel, P., and La Cruz, A. (2004). "Geometric Methods for Vessel Visualization and Quantification — A Survey". In: *Geometric Modeling for Scientific Visualization.* Berlin, Heidelberg: Springer Berlin Heidelberg, pp. 399–419 (cit. on p. 13).

Buhmann, M. D. (2000). "Radial Basis Functions". In: *Acta numerica* 9, pp. 1–38 (cit. on p. 30).

Canezin, F. (2016). "Study of the composition models of field functions in computer graphics". PhD thesis. Université de Toulouse (cit. on p. 51).

Cani, M. P. and Hornus, S. (2001). “Subdivision-curve primitives: a new solution for interactive implicit modeling”. In: *Shape Modeling and Applications*, pp. 82–88 (cit. on p. 14).

Cani-Gascuel, M. P. and Desbrun, M. (1997). “Animation of deformable models using implicit surfaces”. In: *IEEE Transactions on Visualization and Computer Graphics* 3 (cit. on pp. 14, 24).

Carr, J. C. et al. (2001). “Reconstruction and representation of 3D objects with radial basis functions”. In: *Proceedings of the 28th annual conference on Computer graphics and interactive techniques*. New York: ACM Press, pp. 67–76 (cit. on pp. 30, 31).

Chen, J., Jin, X., and Deng, Z. (2014). “GPU-based polygonization and optimization for implicit surfaces”. In: *The Visual Computer* 31.2, pp. 119–130 (cit. on p. 28).

Chow, H. N., Tan, S., and Sze, W. S. (2007). “Layered Modeling of Porous Structures with Voronoi Diagrams”. In: *Computer-Aided Design and Applications* 4.1-4, pp. 321–330 (cit. on p. 86).

Christie, A. and Roditi, G. (2014). “Vascular Imaging: The Evolving Role of the Multidisciplinary Team Meeting in Peripheral Vascular Disease”. In: *Seminars in Interventional Radiology* 31.04, pp. 320–329 (cit. on p. 5).

Coombe, G. (2006). *An Introduction to Scattered Data Approximation* (cit. on p. 51).

Coutelieris, F. A. and Delgado, J. M. P. Q. (2012). “Fundamentals of Porous Structures”. In: *Transport Processes in Porous Media*. Berlin, Heidelberg: Springer Berlin Heidelberg, pp. 5–21 (cit. on p. 86).

Cox, J. and Kirkpatrick, R. C. (1896). “The New Photography: with Report of a Case in which a Bullet was Photographed in the Leg”. In: *Montreal Medical Journal* (cit. on p. 3).

Crivellaro, A., Perotto, S., and Zonca, S. (2017). “Reconstruction of 3D scattered data via radial basis functions by efficient and robust techniques”. In: *Applied Numerical Mathematics* 113, pp. 93–108 (cit. on p. 32).

Cuomo, S. et al. (2017). “Reconstruction of implicit curves and surfaces via RBF interpolation”. In: *Applied Numerical Mathematics* 116, pp. 157–171 (cit. on p. 32).

Das, B. K. (2014). *Positron Emission Tomography*. A Guide for Clinicians. Springer (cit. on p. 4).

De Rossi, A. and Perracchione, E. (2017). “Positive constrained approximation via RBF-based partition of unity method”. In: *Journal of Computational and Applied Mathematics* 319, pp. 338–351 (cit. on p. 32).

Desbrun, M. and Gascuel, M.-P. (1995). “Animating soft substances with implicit surfaces”. In: *Proceedings of the 22nd annual conference on Computer graphics and interactive techniques - SIGGRAPH ’95*. New York, New York, USA: ACM Press, pp. 287–290 (cit. on p. 24).

Drever, L. a. et al. (2007). “Comparison of three image segmentation techniques for target volume delineation in positron emission tomography.” In: *Journal of applied clinical medical physics / American College of Medical Physics* 8.2, pp. 93–109 (cit. on p. 19).

Dwight, T. and Piersol, G. A. (1923). *Human anatomy: including structure and development and practical considerations*. Philadelphia: Lippincott (cit. on p. 89).

Foley, J. D. (1996). *Computer Graphics: Principles and Practice (Second Edition)*. Addison-Wesley systems programming series. Addison-Wesley (cit. on p. 42).

Foley, J. D. and Van Dam, A. (1982). *Fundamentals of Interactive Computer Graphics*. Boston, MA, USA: Addison-Wesley Longman Publishing Co., Inc. (cit. on p. 23).

Frangi, A. F., Niessen, W. J., and Viergever, M. A. (2001). “Three-dimensional modeling for functional analysis of cardiac images: a review.” In: *IEEE Transactions on Medical Imaging* 20.1, pp. 2–25 (cit. on p. 18).

Freytag, M., Shapiro, V., and Tsukanov, I. (2006). “Field modeling with sampled distances”. In: *Computer-Aided Design* 38.2, pp. 87–100 (cit. on p. 33).

Frisken, S. F. et al. (2000). “Adaptively Sampled Distance Fields”. In: *Proceedings of the 27th annual conference on Computer graphics and interactive techniques*. New York: ACM Press, pp. 249–254 (cit. on p. 36).

Gallier, J. (2018). *Curves and surfaces in geometric modeling: theory and algorithms*. University of Pennsylvania (cit. on p. 6).

Gamito, M. N. and Maddock, S. C. (2007). “A Progressive Refinement Approach for the Visualisation of Implicit Surfaces”. In: *Communications in Computer and Information Science*. University of Sheffield, Sheffield, United Kingdom. Berlin, Heidelberg: Springer Berlin Heidelberg, pp. 93–108 (cit. on p. 26).

Gibson, L. J. and Ashby, M. F. (2014). *Cellular solids*. 2nd ed. Structure and Properties. Cambridge: Cambridge University Press (cit. on p. 86).

Gomes, A. et al. (2009). *Implicit Curves and Surfaces: Mathematics, Data Structures and Algorithms*. Springer Science & Business Media (cit. on p. 22).

Gourmel, O. et al. (2013). “A gradient-based implicit blend”. In: *ACM Transactions on Graphics (TOG)* 32.2, 12:1–12:12 (cit. on pp. 16, 26, 40).

Groot, E. de, Wyvill, B., and Wetering, H. van de (2009). “Locally restricted blending of Blobtrees”. In: *Computers & Graphics* 33.6, pp. 690–697 (cit. on pp. 24, 40).

Guennebaud, G. and Gross, M. (2007). “Algebraic point set surfaces”. In: *ACM Transactions on Graphics* 26.3, p. 23 (cit. on pp. 26, 36).

Hahn, H. K., Preim, B., and Selle, D. (2001). “Visualization and interaction techniques for the exploration of vascular structures”. In: *Visualization*, pp. 395–578 (cit. on pp. 7, 18).

Hansen, C. D. and Johnson, C. R. (2005). *The Visualization Handbook.* Academic Press (cit. on p. 7).

Haralick, R. M., Sternberg, S. R., and Zhuang, X. (1987). "Image Analysis Using Mathematical Morphology". In: *IEEE transactions on pattern analysis and machine intelligence* PAMI-9.4, pp. 532–550 (cit. on p. 83).

Hartung, M. P., Grist, T. M., and François, C. J. (2011). "Magnetic resonance angiography: Current status and future directions". In: *Journal of Cardiovascular Magnetic Resonance* 13.1, p. 19 (cit. on p. 5).

Herrick, A. L. and Hutchinson, C. (2004). "Vascular imaging". In: *Best Practice & Research Clinical Rheumatology* 18.6, pp. 957–979 (cit. on p. 5).

Hoffmann, C. (1993). "Implicit curves and surfaces in CAGD". In: *IEEE Computer Graphics and Applications* 13.1, pp. 79–88 (cit. on p. 23).

Hoffmann, C. (2004). "Solid modeling". In: *Handbook of Discrete and Computational Geometry.* Chapman and Hall/CRC (cit. on pp. 6, 22).

Hoffmann, C. and Hopcroft, J. E. (1985). "The potential method for blending surfaces and corners". In: (cit. on pp. 23, 40).

Hoffmann, C. and Vanecek, G. (1991). "Fundamental techniques for geometric and solid modeling". In: *Control and dynamic systems* 48, pp. 101–165 (cit. on p. 22).

Hollister, S. J. and Kikuchi, N. (1992). "A comparison of homogenization and standard mechanics analyses for periodic porous composites". In: *Computational Mechanics* 10.2, pp. 73–95 (cit. on p. 86).

Hollister, S. J., Maddox, R. D., and Taboas, J. M. (2002). "Optimal design and fabrication of scaffolds to mimic tissue properties and satisfy biological constraints". In: *Biomaterials* 23.20, pp. 4095–4103 (cit. on p. 86).

Hong, Q. (2012). "Accurate geometry reconstruction of vascular structures using implicit splines". PhD thesis. University of Hull (cit. on pp. 19, 21).

Hong, Q. (2013). "A skeleton-based technique for modelling implicit surfaces". In: *2013 6th International Congress on Image and Signal Processing (CISP)* 2, pp. 686–691 (cit. on pp. 12, 21).

Hong, Q., Li, Q., and Tian, J. (2012). "Implicit Reconstruction of Vasculatures Using Bivariate Piecewise Algebraic Splines." In: *IEEE transactions on medical imaging* 31.3, pp. 543–553 (cit. on pp. 7, 16, 21, 26, 44, 45).

Hong, Q. et al. (2015). "An implicit skeleton-based method for the geometry reconstruction of vasculatures". In: *The Visual Computer*, pp. 1–12 (cit. on p. 21).

Hoppe, H. (1994). "Surface reconstruction from unorganized points". PhD thesis. University of Washington (cit. on p. 35).

Hossain, S. S. et al. (2011). "Mathematical modeling of coupled drug and drug-encapsulated nanoparticle transport in patient-specific coronary artery walls". In: *Computational Mechanics* 49.2, pp. 213–242 (cit. on p. 12).

Hsu, P.-C. (2013). “A Framework for Developing Boolean Set Implicit Blends from an Existing Union or Intersection Blend in Soft Object Modeling”. In: *Journal of Industrial and Intelligent Information Vol* 1.4, pp. 191–195 (cit. on p. 25).

Hsu, P.-C. et al. (2015). “Generalized Erosion and Dilation Operations of Distance Functions for Deforming Soft Objects”. In: *Journal of Image and Graphics* 3.2 (cit. on p. 33).

Ijiri, T. et al. (2013). “Bilateral Hermite Radial Basis Functions for Contour-based Volume Segmentation”. In: *EUROGRAPHICS ’94*. Wiley Online Library, pp. 123–132 (cit. on p. 31).

Ijiri, T. et al. (2014). “Flower modeling via X-ray computed tomography”. In: *ACM Transactions on Graphics*. Riken, Wako, Japan, pp. 1–10 (cit. on p. 32).

Kaladji, A. et al. (2012). “Computer-aided surgery: Concepts and applications in vascular surgery”. In: *Perspectives in Vascular Surgery and Endovascular Therapy* 24.1, pp. 23–27 (cit. on p. 2).

Kaufman, A. and Mueller, K. (2005). “Overview of volume rendering”. In: *The visualization handbook* (cit. on pp. 22, 41).

Kazhdan, M., Bolitho, M., and Hoppe, H. (2006). “Poisson Surface Reconstruction”. In: *Eurographics Symposium on Geometry Processing*. Ed. by K. Polthier and A. Sheffer. The Eurographics Association. Symposium on Geometry Processing (cit. on p. 26).

Kazhdan, M. and Hoppe, H. (2013). “Screened poisson surface reconstruction”. In: *ACM Transactions on Graphics* 32.3, pp. 1–13 (cit. on p. 26).

Kerrien, E. et al. (2017). “Blood vessel modeling for interactive simulation of interventional neuroradiology procedures”. In: *Medical image analysis* 35, pp. 685–698 (cit. on p. 21).

Kim, Y. and Horii, S. C. (2000). *Handbook of Medical Imaging, Volume 3. Display and PACS*. SPIE Press (cit. on p. 4).

Kirbas, C. and Quek, F. (2004). “A review of vessel extraction techniques and algorithms”. In: *ACM Computing Surveys (CSUR)* 36.2, pp. 81–121 (cit. on p. 20).

Kishore, L. T. and Gupta, P. C. (2013). “Vascular imaging:Past, present & future”. In: *Journal International Medical Sciences Academy* 26.1, pp. 65–68 (cit. on pp. 3, 5).

Kleck, J. E. (1989). *Modeling Using Implicit Surfaces*. Technical report (University of California, Santa Cruz. Computer Research Laboratory). University of California, Santa Cruz (cit. on p. 40).

Klein, J. and Zachmann, G. (2004). “Point cloud surfaces using geometric proximity graphs”. In: *Computers & Graphics* 28.6, pp. 839–850 (cit. on p. 36).

Kou, X. and Tan, S. (2010). “A simple and effective geometric representation for irregular porous structure modeling”. In: *Computer-Aided Design* 42.10, pp. 930–941 (cit. on p. 86).

Kretschmer, J. et al. (2013). “Interactive Patient-Specific Vascular Modeling with Sweep Surfaces”. In: *IEEE Transactions on Visualization and Computer Graphics* 19.12, pp. 28–37 (cit. on pp. 7, 16, 19, 22, 44, 45).

Kumar, R. P. et al. (2015). “Three-Dimensional Blood Vessel Segmentation and Centerline Extraction based on Two-Dimensional Cross-Section Analysis”. In: *Annals of Biomedical Engineering*, pp. 1–12 (cit. on pp. 2, 13, 22).

Larobina, M. and Murino, L. (2013). “Medical Image File Formats”. In: *Journal of Digital Imaging* 27.2, pp. 200–206 (cit. on pp. 3, 4).

Lefdal, M. B. (2016). “Segmentation and Centerline Extraction of the Coronary Arteries with GPU Processing”. MA thesis. Norwegian University (cit. on pp. 2, 13).

Lepore, M. R. et al. (2000). “Minimally invasive vascular techniques.” In: *The Ochsner journal* 2.3, pp. 145–152 (cit. on pp. 1, 2).

Lesage, D. et al. (2009). “A review of 3D vessel lumen segmentation techniques: Models, features and extraction schemes”. In: *Medical image analysis* 13.6, pp. 819–845 (cit. on pp. 1, 7, 20).

Levoy, M. (1988). “Display of surfaces from volume data”. In: *IEEE Computer Graphics and Applications* 8.3, pp. 29–37 (cit. on p. 42).

Li, Q. (2004). “Blending Implicit Shapes Using Smooth Unit Step Functions ”. In: *SHORT Communication Papers proceedings*, pp. 297–304 (cit. on p. 25).

Li, Q. (2007). “Smooth Piecewise Polynomial Blending Operations for Implicit Shapes.” In: *Computer Graphics Forum* 26.2, pp. 157–171 (cit. on pp. 6, 25, 38, 62).

Li, Q. and Griffiths, J. G. (2004a). “Least Squares Ellipsoid Specific Fitting.” In: *GMP*, pp. 335–340 (cit. on p. 51).

Li, Q. and Tian, J. (2008). “Blending implicit shapes using fuzzy set operations”. In: *WSEAS Transactions on Information Science and . . .* (Cit. on p. 25).

Li, Q. and Tian, J. (2009). “2D piecewise algebraic splines for implicit modeling”. In: *ACM Transactions on Graphics (TOG)* 28.2, p. 13 (cit. on pp. 16, 26, 28).

Li, Q. and Tian, J. (2011). “Partial shape-preserving splines”. In: *Computer-Aided Design* 43.4, pp. 394–409 (cit. on p. 26).

Li, Q. et al. (2004b). “Implicit Fitting Using Radial Basis Functions with Ellipsoid Constraint.” In: *Computer Graphics Forum* 23.1, pp. 55–70 (cit. on pp. 31, 36, 50, 51, 53, 96).

Li, Q. et al. (2018). “Towards additive manufacturing oriented geometric modeling using implicit functions”. In: *Visual Computing for Industry, Biomedicine, and Art* 1.1, p. 165 (cit. on p. 87).

Liang, J., Park, F., and Zhao, H. (2013). “Robust and efficient implicit surface reconstruction for point clouds based on convexified image segmentation”. In: *Journal of Scientific Computing* 54.2-3, pp. 577–602 (cit. on pp. 12, 17, 44).

Lien, J. M. (2010). “A simple method for computing Minkowski sum boundary in 3D using collision detection”. In: *Springer Tracts in Advanced Robotics*. George Mason University, Fairfax, United States. Berlin, Heidelberg: Springer Berlin Heidelberg, pp. 401–415 (cit. on p. 83).

Lim, C. T., Turkiyyah, G. M., and Ganter, M. A. (1995). “Implicit reconstruction of solids from cloud point sets”. In: *Proceedings of the third ACM symposium on Solid modeling and applications*. New York, New York, USA: ACM Press, pp. 393–402 (cit. on p. 22).

Lin, Y. et al. (2009). “Dual-RBF based surface reconstruction”. In: *The Visual Computer* 25.5-7, pp. 599–607 (cit. on p. 31).

Liu, P. S. and Chen, G. (2014). *Porous Materials: Processing and Applications*. Elsevier Inc. (cit. on p. 86).

Liu, S. et al. (2016). “A closed-form formulation of HRBF-based surface reconstruction by approximate solution”. In: *Computer-Aided Design* 78, pp. 147–157 (cit. on p. 32).

Liu, Y. et al. (2017). “Implicit surface reconstruction with total variation regularization”. In: *Computer Aided Geometric Design* 52-53, pp. 135–153 (cit. on p. 27).

Lorensen, W. E. and Cline, H. E. (1987). “Marching cubes: A high resolution 3D surface construction algorithm”. In: *ACM SIGGRAPH Computer Graphics* 21.4, pp. 163–169 (cit. on pp. 7, 17, 45).

Macêdo, I., Gois, J. P., and Velho, L. (2009). “Hermite interpolation of implicit surfaces with radial basis functions”. In: *Computer Graphics and Image Processing (SIBGRAPI), 2009 XXII Brazilian Symposium on.* IEEE, pp. 1–8 (cit. on p. 31).

Macêdo, I., Gois, J. P., and Velho, L. (2010). “Hermite Radial Basis Functions Implicits”. In: *Computer Graphics Forum* 30.1, pp. 27–42 (cit. on pp. 31, 36).

Maekawa, T. (1999). “An overview of offset curves and surfaces”. In: *Computer-Aided Design* 31.3, pp. 165–173 (cit. on pp. 69, 73).

Masutani, Y., Masamune, K., and Dohi, T. (1996). “Region-growing based feature extraction algorithm for tree-like objects”. In: *Visualization in Biomedical Computing*. Berlin, Heidelberg: Springer, Berlin, Heidelberg, pp. 159–171 (cit. on p. 19).

Menon, J. et al. (1996). “Implicit surfaces for geometric modeling and computer graphics”. In: *ACM SIGGRAPH 1996* (cit. on pp. 22, 24).

Middleditch, A. E. and Sears, K. H. (1985). “Blend surfaces for set theoretic volume modelling systems”. In: *ACM SIGGRAPH Computer Graphics* 19.3, pp. 161–170 (cit. on pp. 2, 23).

Mistretta, C. A., Crummy, A. B., and Strother, C. M. (1981). “Digital angiography: a perspective.” In: *Radiology* 139.2, pp. 273–276 (cit. on p. 5).

Mittal, R. et al. (2016). “Computational modeling of cardiac hemodynamics: Current status and future outlook”. In: *Journal of Computational Physics* 305.C, pp. 1065–1082 (cit. on p. 106).

Mortenson, M. E. (1997). “Geometric modeling”. In: (cit. on p. 6).

Muraki, S. (1991). “Volumetric shape description of range data using “Blobby Model””. In: *ACM SIGGRAPH computer graphics* 25.4, pp. 227–235 (cit. on p. 23).

Museth, K. et al. (2002). “Level set surface editing operators”. In: *ACM Transactions on Graphics (TOG)* (cit. on pp. 22, 25).

Musialski, P. et al. (2015). “Reduced-order shape optimization using offset surfaces”. In: *ACM Transactions on Graphics (TOG)* 34.4, 102–102:9 (cit. on p. 69).

Newman, T. S. and Yi, H. (2006). “A survey of the marching cubes algorithm”. In: *Computers & Graphics* 30.5, pp. 854–879 (cit. on p. 17).

Nishimura, H. (1985). “Object modeling by distribution function and a method of image generation”. In: *Trans Inst Electron Commun Eng Japan* 68, p. 718 (cit. on p. 23).

Oeltze, S. and Preim, B. (2005). “Visualization of vasculature with convolution surfaces: method, validation and evaluation”. In: *IEEE Transactions on Medical Imaging* 24.4, pp. 540–548 (cit. on pp. 7, 20).

Oentoro, A. (2009). “A system for computer-assisted surgery with intraoperative CT imaging”. MA thesis. Queen’s University (cit. on p. 3).

Ohtake, Y., Belyaev, A., and Seidel, H. P. (2003a). “A multi-scale approach to 3D scattered data interpolation with compactly supported basis functions”. In: *2003 Shape Modeling International.* IEEE, pp. 153–161 (cit. on p. 30).

Ohtake, Y., Belyaev, A., and Seidel, H. P. (2004). “3D scattered data approximation with adaptive compactly supported radial basis functions”. In: *Shape Modeling Applications, 2004. Proceedings*, pp. 31–39 (cit. on p. 30).

Ohtake, Y., Belyaev, A., and Seidel, H. P. (2005). “3D scattered data interpolation and approximation with multilevel compactly supported RBFs”. In: *Graphical models* 67.3, pp. 150–165 (cit. on p. 30).

Ohtake, Y., Belyaev, A., and Seidel, H. P. (2006). “Sparse surface reconstruction with adaptive partition of unity and radial basis functions”. In: *Graphical models* 68.1, pp. 15–24 (cit. on p. 30).

Ohtake, Y. et al. (2003b). “Multi-level partition of unity implicits”. In: *ACM Transactions on Graphics.* New York: ACM Press, pp. 463–470 (cit. on pp. 25, 45).

Opalach, A. (1996). “Implicit Surfaces for Modelling and Character Animation”. PhD thesis. The University of Sheffield (cit. on p. 24).

Opalach, A. and Maddock, S. (1995). “An overview of implicit surfaces”. In: *Introduction to modelling and animation using implicit surfaces* (cit. on p. 24).

Osher, S. and Fedkiw, R. (2006). *Level Set Methods and Dynamic Implicit Surfaces.* Vol. 153. Applied Mathematical Sciences. New York, NY: Springer Science & Business Media (cit. on pp. 22, 25, 77, 78).

Owens, J. D. et al. (2007). “A Survey of General-Purpose Computation on Graphics Hardware”. In: *Computer Graphics Forum* 26.1, pp. 80–113 (cit. on pp. 28, 59).

Pan, M., Tong, W., and Chen, F. (2016). “Compact implicit surface reconstruction via low-rank tensor approximation”. In: *Computer-Aided Design* 78, pp. 158–167 (cit. on p. 36).

Pan, M., Tong, W., and Chen, F. (2017). “Phase-field guided surface reconstruction based on implicit hierarchical B-splines”. In: *Computer Aided Geometric Design* 52-53, pp. 154–169 (cit. on p. 36).

Pan, R. and Skala, V. (2010). “A two-level approach to implicit surface modeling with compactly supported radial basis functions”. In: *Engineering with Computers* 27.3, pp. 299–307 (cit. on p. 30).

Papademetris, X. et al. (2009). “From medical image computing to computer-aided intervention: development of a research interface for image-guided navigation”. In: *The International Journal of Medical Robotics and Computer Assisted Surgery* 5.2, pp. 147–157 (cit. on p. 2).

Pasko, A. A. and Savchenko, V. V. (1994). “Blending operations for the functionally based constructive geometry”. In: *Citeseer* (cit. on pp. 24, 40).

Pasko, A. and Adzhiev, V. (2002a). “Function-Based Shape Modeling: Mathematical Framework and Specialized Language”. In: *Automated Deduction in Geometry.* Berlin, Heidelberg: Springer, Berlin, Heidelberg, pp. 132–160 (cit. on p. 6).

Pasko, A. et al. (1995). “Function representation in geometric modeling: concepts, implementation and applications”. In: *The Visual Computer* 11.8, pp. 429–446 (cit. on pp. 6, 22, 24, 37, 38, 40).

Pasko, G. et al. (2002b). “Bounded blending operations”. In: *Proceedings SMI. Shape Modeling International 2002.* IEEE Comput. Soc, pp. 95–103 (cit. on p. 24).

Peters, T. M. (2001). “Image-guided surgery: from X-rays to virtual reality”. In: *Computer Methods in Biomechanics and Biomedical Engineering* 4.1, pp. 27–57 (cit. on p. 2).

Pommert, A., Bomans, M., and Höhne, K. H. (1992). “Volume visualization in magnetic resonance angiography”. In: *IEEE Comput. Graphics Appl* (cit. on pp. 7, 41).

Prautzsch, H., Boehm, W., and Paluszny, M. (2002). *Bezier and B-spline techniques.* Berlin, Heidelberg: Springer Berlin Heidelberg (cit. on p. 74).

Preim, B. and Botha, C. P. (2014). *Visual Computing for Medicine: Theory, Algorithms, and Applications: Second Edition.* University of Bremen, Bremen, Germany: Elsevier (cit. on pp. 6, 7, 12).

Preim, B. and Oeltze, S. (2008). "3D visualization of vasculature: an overview". In: *Visualization in medicine and life sciences*, pp. 39–59 (cit. on pp. 7, 17, 18, 41, 45).

Pressley, A. N. (2010). *Elementary differential geometry* (cit. on p. 48).

Ricci, A. (1974). "A constructive geometry for computer graphics". In: *Computer-Aided Design* 6.1, p. 53 (cit. on pp. 23, 37, 38).

Rockwood, A. P. (1989). "The displacement method for implicit blending surfaces in solid models". In: *ACM Transactions on Graphics (TOG)* 8.4, pp. 279–297 (cit. on p. 40).

Rouhani, M. and Sappa, A. D. (2012). "Implicit Polynomial Representation Through a Fast Fitting Error Estimation". In: *IEEE Transactions on Image Processing* 21.4, pp. 2089–2098 (cit. on p. 33).

Rouhani, M., Sappa, A. D., and Boyer, E. (2015). "Implicit B-spline surface reconstruction". In: *IEEE Transactions on Image Processing* 24.1, pp. 22–32 (cit. on p. 27).

Ruikar, D. D., Hegadi, R. S., and Santosh, K. C. (2018). "A Systematic Review on Orthopedic Simulators for Psycho-Motor Skill and Surgical Procedure Training". In: *Journal of Medical Systems* 42.9, p. 168 (cit. on p. 41).

Rvachev, V. (1963). "An analytic description of certain geometric objects". In: *Soviet Mathematics. Doklady* 153.4, pp. 765–767 (cit. on p. 37).

Sabin, M. A. (1968). *The Use of Potential Surfaces for Numerical Geometry.* Tech. rep. VTO/MS/153. Weybridge, UK: British Aircraft Corporation (cit. on pp. 23, 40).

Scheffler, M. and Colombo, P. (2006). *Cellular Ceramics: Structure, Manufacturing, Properties and Applications.* Structure, Manufacturing, Properties and Applications. Weinheim, FRG: Wiley-VCH Verlag GmbH & Co. KGaA (cit. on p. 86).

Schneider, R. (1993). *Convex Bodies: The Brunn-Minkowski Theory.* Encyclopedia of Mathematics and its Applications. Cambridge University Press (cit. on p. 83).

Schroeder, C. et al. (2005a). "Computer-aided design of porous artifacts". In: *Computer-Aided Design* 37.3, pp. 339–353 (cit. on p. 86).

Schroeder, W. J., Lorensen, W. E., and Linthicum, S. (1994). "Implicit modeling of swept surfaces and volumes". In: *Proceedings of the conference on Visualization'94.* IEEE Comput. Soc. Press, pp. 40–45 (cit. on p. 15).

Schroeder, W. J., Martin, K., and Lorensen, B. (2005b). *The Visualization Toolkit.* Elsevier (cit. on p. 4).

Schumann, C. et al. (2007). “Model-free Surface Visualization of Vascular Trees”. In: *Eurographics/ IEEE-VGTC Symposium on Visualization (2007)*. Citeseer, pp. 283–290 (cit. on pp. 7, 17).

Schumann, C. et al. (2008). “Implicit vessel surface reconstruction for visualization and CFD simulation.” In: *International Journal of Computer Assisted Radiology and Surgery* 2.5, pp. 275–286 (cit. on p. 20).

Sederberg, T. W. (1985). “Piecewise algebraic surface patches”. In: *Computer Aided Geometric Design* 2.1-3, pp. 53–59 (cit. on p. 23).

Sederberg, T. W. (1987). *Algebraic geometry for surface and solid modeling.* Geometric Modeling: Algorithms and New Trends (cit. on p. 23).

Selle, D. et al. (2002). “Analysis of vasculature for liver surgical planning”. In: *IEEE Transactions on Medical Imaging* 21.11, pp. 1344–1357 (cit. on pp. 14, 19).

Shang, Y. et al. (2011). “Vascular active contour for vessel tree segmentation”. In: *Biomedical Engineering, IEEE Transactions on* 58.4, pp. 1023–1032 (cit. on pp. 21, 22).

Shapiro, V. (1991). *Theory of R-functions and Applications: A Primer.* Tech. rep. (cit. on p. 37).

Shapiro, V. (1994). “Real functions for representation of rigid solids”. In: *Computer Aided Geometric Design* 11.2, pp. 153–175 (cit. on p. 37).

Shapiro, V. and Tsukanov, I. (1999). “Implicit functions with guaranteed differential properties”. In: *Proceedings of the fifth ACM symposium on Solid modeling and applications.* University of Wisconsin Madison. New York, New York, USA: ACM, pp. 258–269 (cit. on p. 22).

Sherstyuk, A. (1999). “Kernel functions in convolution surfaces: a comparative analysis”. In: *The Visual Computer* 15.4, pp. 171–182 (cit. on p. 40).

Sigg, C. (2006). “Representation and rendering of implicit surfaces”. PhD thesis. ETH Zurich (cit. on p. 26).

Smistad, E., Elster, A. C., and Lindseth, F. (2012). “GPU-based airway segmentation and centerline extraction for image guided bronchoscopy”. In: *Norsk informatikkonferanse* (cit. on pp. 2, 13).

Sofka, M. and Stewart, C. V. (2006). “Retinal Vessel Centerline Extraction Using Multiscale Matched Filters, Confidence and Edge Measures”. In: *IEEE Transactions on Medical Imaging* 25.12, pp. 1531–1546 (cit. on p. 13).

Song, X. and Jüttler, B. (2009). “Modeling and 3D object reconstruction by implicitly defined surfaces with sharp features”. In: *Computers & Graphics* 33.3, pp. 321–330 (cit. on p. 25).

Stam, J. and Schmidt, R. (2011). “On the velocity of an implicit surface”. In: *ACM Transactions on Graphics* 30.3, pp. 1–7 (cit. on p. 27).

Subhlok, J. et al. (1993). “Exploiting task and data parallelism on a multicomputer”. In: *ACM SIGPLAN Notices* 28.7, pp. 13–22 (cit. on p. 60).

Tankelevich, R. and Rockwood, A. P. (2004). “Potential fields and implicit modeling”. In: *ACM SIGGRAPH 2004 Posters*. New York, New York, USA: ACM Press, p. 3 (cit. on p. 33).

Tao, J. and Wang, C. (2016). “Peeling the flow: a sketch-based interface to generate stream surfaces”. In: *SIGGRAPH ASIA 2016 Symposium on Visualization*, pp. 14–8 (cit. on p. 27).

Taubin, G. (1988). “Nonplanar curve and surface estimation in 3-space”. In: *Proc. IEEE Conf. Robotics and Automation*. Philadelphia: IEEE Comput. Soc. Press, pp. 644–645 (cit. on pp. 32, 80).

Taubin, G. (1991). “Estimation of planar curves, surfaces, and nonplanar space curves defined by implicit equations with applications to edge and range image segmentation”. In: *IEEE transactions on pattern analysis and machine intelligence* 13.11, pp. 1115–1138 (cit. on pp. 32, 80).

Taubin, G. (1993). “An improved algorithm for algebraic curve and surface fitting”. In: *Computer Vision*, pp. 658–665 (cit. on p. 33).

Taylor, C. A. and Figueroa, C. A. (2009). “Patient-specific modeling of cardiovascular mechanics.” In: *Annual Review of Biomedical Engineering* 11, pp. 109–134 (cit. on p. 21).

Taylor, R. H. and Joskowicz, L. (2002). “Computer-integrated surgery and medical robotics”. In: *Standard Handbook of Biomedical Engineering and Design (2002)* 19.5, pp. 765–781 (cit. on p. 3).

Telea, A. and Wijk, J. J. (2002). “An augmented fast marching method for computing skeletons and centerlines”. In: *Proceedings of VisSym* (cit. on p. 13).

Tetteh, G. et al. (2017). “Deep-FExt: Deep Feature Extraction for Vessel Segmentation and Centerline Prediction”. In: *Medical Image Computing and Computer-Assisted Intervention – MICCAI 2012*. Cham: Springer International Publishing, pp. 344–352 (cit. on p. 14).

Tobor, I., Reuter, P., and Schlick, C. (2006). “Reconstructing multi-scale variational partition of unity implicit surfaces with attributes”. In: *Graphical models* 68.1, pp. 25–41 (cit. on p. 30).

Torres, C. E. and Barba, L. A. (2009). “Fast radial basis function interpolation with Gaussians by localization and iteration”. In: *Journal of Computational Physics* 228.14, pp. 4976–4999 (cit. on p. 31).

Turk, G. and O’Brien, J. F. (1999). *Variational Implicit Surfaces*. Tech. rep. Georgia Institute of Technology (cit. on pp. 24, 36).

Turk, G. and O'Brien, J. F. (2002). "Modelling with implicit surfaces that interpolate". In: *ACM Transactions on Graphics (TOG)* 21.4, pp. 855–873 (cit. on p. 24).

Twigg, C. (2003). "Catmull-rom splines". In: *Computer* 41.6, pp. 4–6 (cit. on p. 16).

Tyrrell, J. A. et al. (2007). "Robust 3-D modeling of vasculature imagery using superellipsoids". In: *Medical Imaging, IEEE Transactions on* 26.2, pp. 223–237 (cit. on p. 2).

Urick, B. et al. (2017). "Review of Patient-Specific Vascular Modeling: Template-Based Isogeometric Framework and the Case for CAD". In: *Archives of Computational Methods in Engineering* 11.Supplement 1, pp. 1–24 (cit. on p. 18).

Varadhan, G. and Manocha, D. (2006). "Accurate Minkowski sum approximation of polyhedral models". In: *Graphical models* 68.4, pp. 343–355 (cit. on p. 83).

Velho, L., Gomes, J., and Figueiredo, L. H. de (2007). *Implicit Objects in Computer Graphics*. Springer Science & Business Media (cit. on p. 34).

Wald, I. and Slusallek, P. (2001). "State of the art in interactive ray tracing". In: *State of the Art Reports, EUROGRAPHICS*, pp. 21–42 (cit. on p. 42).

Wang, C. C. L. and Chen, Y. (2013). "Thickening freeform surfaces for solid fabrication". In: *Rapid Prototyping Journal* 19.6, pp. 395–406 (cit. on p. 68).

Wang, W. p. and Wang, K. k. (1986). "Geometric Modeling for Swept Volume of Moving Solids". In: *IEEE Computer Graphics and Applications* 6.12, pp. 8–17 (cit. on p. 15).

Wang, X. et al. (2016). "Repairing the cerebral vascular through blending Ball B-Spline curves with G 2 continuity". In: *Neurocomputing* 173, pp. 768–777 (cit. on p. 18).

Warren, J. (1989). "Blending algebraic surfaces". In: *ACM Transactions on Graphics* 8.4, pp. 263–278 (cit. on p. 23).

Weiler, K. J. (1986). "Topological Structures for Geometric Modeling". PhD thesis. Rensselaer Polytechnic Institue (cit. on pp. 4, 6).

Wood, A. (1870). *The American botanist and florist; including lessons in the structure, life, and growth of plants; together with a simple analytical flora, descriptive of the native and cultivated plants growing in the Atlantic division of the America*. Chicago: A.S. Barnes & company (cit. on p. 89).

World Health Organization (2010). *Global atlas on cardiovascular disease prevention and control. 2011*. Genebra: World Health Organization (cit. on p. 1).

World Health Organization (2017). *Cardiovascular Diseases (CVDs)*. Tech. rep. World Health Organization (cit. on p. 1).

World Health Organization (2018). *World Health Statistics 2018*. Monitoring Health for the SDGs, Sustainable Development Goals. Geneva (cit. on p. 1).

Wu, G. and Zhang, Y. (2015). “A Novel Fractional Implicit Polynomial Approach for Stable Representation of Complex Shapes”. In: *Journal of Mathematical Imaging and Vision* 55.1, pp. 89–104 (cit. on p. 36).

Wu, X. et al. (2011). “Segmentation and reconstruction of vascular structures for 3D real-time simulation”. In: *Medical image analysis* 15.1, pp. 22–34 (cit. on pp. 2, 21, 45).

Wu, Z. (1992). “Hermite-Birkhoff interpolation of scattered data by radial basis functions”. In: *Approximation Theory and its Applications* (cit. on p. 36).

Wyvill, B. and Guy, A. (1998). “The BlobTree”. In: *Journal of Implicit Surfaces* 3 (cit. on pp. 6, 24, 40).

Wyvill, G., McPheeters, C., and Wyvill, B. (1986). “Data structure for soft objects”. In: *The Visual Computer* 2.4, pp. 227–234 (cit. on p. 23).

Wyvill, G. and Trotman, A. (1990). “Ray-Tracing Soft Objects”. In: *CG International ’90*. Ed. by T.-S. Chua and T. L. Kunii. Tokyo: Springer Japan, pp. 469–476 (cit. on p. 23).

Xu, C. and Prince, J. L. (1997). “Gradient vector flow: a new external force for snakes”. In: *Proceedings of IEEE Computer Society Conference on Computer Vision and Pattern Recognition*. IEEE, pp. 66–71 (cit. on p. 19).

Yokota, R., Barba, L. A., and Knepley, M. G. (2010). “PetRBF–A parallel O(N) algorithm for radial basis function interpolation”. In: *Computer Methods in Applied Mechanics and Engineering* 199.25-28, pp. 1793–1804 (cit. on p. 31).

Yoo, T. S. et al. (2003). “Beyond Blobs: Recent Advances in Implicit Surfaces ”. In: *ACM Transactions on Graphics*, p. 721 (cit. on p. 25).

Yureidini, A. (2014). “Robust blood vessel surface reconstruction for interactive simulations from patient data”. PhD thesis. Université des Sciences et Technologie de Lille-Lille I (cit. on pp. 15, 19, 22).

Yureidini, A. et al. (2012). “Local Implicit Modeling of Blood Vessels for Interactive Simulation”. In: *Medical Image Computing and Computer-Assisted Intervention – MICCAI 2012*. Berlin, Heidelberg: Springer Berlin Heidelberg, pp. 553–560 (cit. on pp. 6, 15, 22).

Zanni, C., Gleicher, M., and Cani, M. P. (2015). “N-ary implicit blends with topology control”. In: *Computers & Graphics* 46.C (cit. on pp. 25, 40).

Zanni, C. et al. (2012). “Geometric details on skeleton-based implicit surfaces”. In: *Eurographics 2012-33rd Annual Conference of the European Association for Computer Graphics*. Eurographics, pp. 49–52 (cit. on pp. 15, 27, 28).

Zeng, H., Liu, Z., and Lin, Z. (2005). “PDE-Driven Implicit Reconstruction of 3D Object”. In: *International Conference on Computer Graphics, Imaging and Visualization (CGIV’05)*. IEEE, pp. 251–256 (cit. on p. 33).

Zhang, Y., Chen, K., and Wong, S. (2008). "3D interactive centerline extraction". In: The Insight Journal (cit. on p. 13).

Zhang, Y. et al. (2007). "Patient-specific vascular NURBS modeling for isogeometric analysis of blood flow". In: *Computer methods in applied mechanics and engineering* 196.29, pp. 2943–2959 (cit. on pp. 2, 7, 16, 18, 19).

Zhao, H., Osher, S., and Fedkiw, R. (2001). "Fast surface reconstruction using the level set method". In: *Proceedings IEEE Workshop on Variational and Level Set Methods in Computer Vision*. IEEE, pp. 194–201 (cit. on pp. 22, 25, 36).

Zhou, Y. and Toga, A. W. (1999). "Efficient skeletonization of volumetric objects". In: *IEEE Transactions on Visualization and Computer Graphics* 5.3, pp. 196–209 (cit. on p. 13).